

## ELECTROCHEMISTRY

Electric field–confined synthesis of single atomic  $\text{TiO}_x\text{C}_y$  electrocatalytic membranesYifan Gao<sup>1,2</sup>, Shuai Liang<sup>3\*</sup>, Chengxu Jiang<sup>1</sup>, Mengyao Gu<sup>3</sup>, Quanbiao Zhang<sup>1</sup>, Ali Abdelhafiz<sup>2</sup>, Zhen Zhang<sup>4</sup>, Ying Han<sup>5</sup>, Yang Yang<sup>5</sup>, Xiaoyuan Zhang<sup>1</sup>, Peng Liang<sup>1</sup>, Ju Li<sup>2,4\*</sup>, Xia Huang<sup>1\*</sup>

Electrocatalysis exhibits certain benefits for water purification, but the low performance of electrodes severely hampers its utility. Here, we report a general strategy for fabricating high-performance three-dimensional (3D) porous electrodes with ultrahigh electrochemical active surface area and single-atom catalysts from earth-abundant elements. We demonstrate a binder-free dual electrospinning-electrospraying (DESP) strategy to densely distribute single atomic Ti and titanium oxycarbide ( $\text{TiO}_x\text{C}_y$ ) sub-3-nm clusters throughout interconnected carbon nanofibers (CNs). The composite offers ultrahigh conductivity and mechanical robustness (ultrasonication resistant). The resulting  $\text{TiO}_x\text{C}_y$  filtration membrane exhibits record-high water purification capability with excellent permeability ( $\sim 8370 \text{ liter m}^{-2} \text{ hour}^{-1} \text{ bar}^{-1}$ ), energy efficiency (e.g., >99% removal of toxins within 1.25 s at  $0.022 \text{ kWh}\cdot\text{m}^{-3}$  per order), and erosion resistance. The hierarchical design of the  $\text{TiO}_x\text{C}_y$  membrane facilitates rapid and energy-efficient electrocatalysis through both direct electron transfer and indirect reactive oxygen species ( $^1\text{O}_2$ ,  $\cdot\text{OH}$ , and  $\text{O}_2^{\cdot-}$ , etc.) oxidations. The electric field–confined DESP strategy provides a general platform for making high-performance 3D electrodes.

## INTRODUCTION

Electrocatalysis is key to fuel cells (1), electrolyzers (2), and  $\text{CO}_2$  utilization (3) and to enable innovative water purification solutions (4–6). For example, electrocatalytic membranes can enhance pollutant removal in water by combining electrocatalytic oxidative degradation and physical retention, thereby outperforming conventional adsorption or biological processes (4, 6, 7). However, the efficiency and sustainability of such an approach remain unclear due to the inadequate performance of current-generation electroactive membranes. It is also unclear whether it is the local catalytic activity, adhesive strength/local contact quality (8, 9) of the catalyst with the current collector, longer-range electronic or chemicals transport, or a combination of these issues that limit the performance of the filtration membrane. For organic toxin removal from water, the important figures of merits are the water flow rate (thus demanding greater porosity), energy efficiency ( $\text{kWh}\cdot\text{m}^{-3}$  per order), durability, and low unintended toxicity—that is, the electrocatalysts need to adhere strongly to the substrate to prevent erosion by the flowing water and, even if eroded and entrained in the drinking water, does not cause harm.

Preparing high-activity catalysts is a major prerequisite. A consensus for increasing catalytic activity is to increase the specific surface area of the catalyst, which is inversely proportional to its size. Correspondingly, reducing the size of catalysts to nano or even single atomic level is crucial. However, the preparation of electrocatalysts with an ultrahigh-specific surface area that remains robust under

flowing conditions is challenging. Current methods such as vacuum filtration (10), metal-support interactions (11), electrodeposition (12–14), anodization (15), and hydrothermal synthesis (16, 17), mainly produce powdered catalysts (16, 18) or thin-layer catalysts on conventional bulk electrodes (10–12, 15, 19). There is a big problem of how to disperse and bind sub-few nanometer or single-atom catalysts (SACs) strongly and densely onto electronically conductive substrates in three dimension, which also need to be erosion resistant. Intimate direct physical contact between electrocatalysts and electronically conductive substrate has been achieved by the exsolution process, where zero-valent electrocatalysts are anchored or “socketed” into the substrate (20) without any third-phase binder. This increases the true contact area (8, 9) and enhances both the erosion resistance and electronic contact. After all, without facile electronic percolation all the way to the current collector, electrocatalysts are inactive by definition. Fabricating robust three dimensionally connected integral electrodes without compromising the specific surface area of raw electrocatalysts can be challenging. Existing strategy that uses binders (21) to prepare bulk catalytic electrodes with electrocatalyst particles is doubtful because the insulating binders markedly reduce the electronic conductance and effective specific surface area, especially the electrochemical active surface area (ECSA). Binders can also obscure SAC and prevent them from reaction. The strategies that produce thin-layer catalysts on bulk electrodes also have limitations because they are not conducive to building three-dimensional (3D) structures that maintain a high specific surface area in the thickness direction.

Yet, another important issue for water purification applications is the manufacturing cost. Although several recent studies have successfully prepared sub-3-nm-scale (13, 22) electrocatalysts with improved specific surface area, the methods and adopted raw materials are costly and less amenable to scaled-up manufacture. Compared to precious metals, light transition-metal oxides (TMOs) have the advantages of lower material cost, higher stability, and lower toxicity. Transition-metal oxycarbides (TMOCs), such as titanium oxycarbide ( $\text{TiO}_x\text{C}_y$ ), overcome the poor electrical conductivity of

<sup>1</sup>State Key Laboratory of Regional Environment and Sustainability, School of Environment, Tsinghua University, Beijing 100084, China. <sup>2</sup>Department of Nuclear Science and Engineering, Massachusetts Institute of Technology, 77 Massachusetts Avenue, Cambridge, MA 02139, USA. <sup>3</sup>Beijing Key Lab for Source Control Technology of Water Pollution, College of Environmental Science and Engineering, Beijing Forestry University, Beijing 100083, China. <sup>4</sup>Department of Materials Science and Engineering, Massachusetts Institute of Technology, 77 Massachusetts Avenue, Cambridge, MA 02139, USA. <sup>5</sup>Department of Engineering Science and Mechanics, The Pennsylvania State University, University Park, PA 16802, USA.

\*Corresponding author. Email: shuai\_liang@bjfu.edu.cn (S.L.); liju@mit.edu (J.L.); xhuang@tsinghua.edu.cn (X.H.)

TMO (e.g.,  $\text{TiO}_2$ ) and have been proven to be an effective electrocatalyst (23). However, the preparation of TMO with high specific surface area is also more challenging. Overall, there is still a lack of effective strategies that allow efficient and low-cost fabrication of integral SAC electrodes with high specific ECSA.

In this study, we developed an electric-filed-confined strategy to fabricate high-performance electrocatalytic membranes with ultrahigh ECSA. The proposed dual electrospinning-electrospraying (DESP) synthetic strategy and subsequent thermal treatment allows in situ generation and assembly of single atomic Ti and sub-3-nm electrocatalyst clusters in 3D pores. Highly scattered single atomic Ti and  $\text{TiO}_x\text{C}_y$  clusters are in situ fused with carbon and highly dispersed in a 3D carbon nanofiber (CN) network, resulting in a porous composite matrix membrane (designated as  $\text{TiO}_x\text{C}_y$  membrane). This envelopment achieved by in situ generation of interleaved  $\text{TiO}_x\text{C}_y$  lattices and anchored single atoms on porous carbon ensures a robust bonding and excellent contact with conductive substrates without using environmentally unfriendly binders. The resultant hierarchical  $\text{TiO}_x\text{C}_y$  membrane achieved record-high electrocatalytic performance with excellent energy efficiencies. Through systematic experimental analyses and simulation, we revealed that such a hierarchical 3D arrangement of single atomic  $\text{TiO}_x\text{C}_y$  enables the establishment of a multidimensional barrier against waterborne toxins. Considering the easy-to-scale-up nature of the fabrication method and the environmentally friendly as well as low-cost merit of the materials used, we envision that this strategy will provide a foundation for the development of high-performance and multifunctional porous electrodes in diverse applications.

## RESULTS AND DISCUSSION

### Fabrication of single atomic $\text{TiO}_x\text{C}_y$ membrane that achieves ultraefficient electrocatalysis

Efficient electrocatalysis requires massive exposure of highly reactive sites and a robust electron transport network (for both long-range fiber-to-fiber electronic transport and fiber-to-catalyst conductance). For water purification (targeting pollutant degradation) or catalytic reactions in other applications (targeting conversion of chemicals), a porous flow-through and macroscopically thick structure that enhances mass transfer and provides sufficient electrode-solution reaction area (24) is an ideal structure for electrodes. Electrospinning is excellent for the preparation of 3D thick nanofiber electrodes (25). However, doping catalysts into the nanofibers is limited by the single electrospinning method [e.g., precursor solution is difficult to homogenize, sub-nano-sized catalysts (or seeds) are easily agglomerated in precursor solutions, and spinning with particle becomes more difficult]. Therefore, we developed a DESP synthetic strategy (Fig. 1A) to first prepare an integral SAC-CN network and then to in situ create robust catalyst-to-carbon fiber-fused connections by thermal post-treatment (fig. S1A). With this strategy, the electrospinning portion is used to construct a highly connected nanofiber matrix using polyacrylonitrile (PAN) as the primary raw material, while the electrospaying portion is used to distribute electrocatalysts [in situ synthesized from titanium butoxide (TBT)] among the CN network. Under the strong electrostatic field, the TBT is vigorously beaten and highly dispersed as clusters and even individual molecules into the PAN network (Fig. 1B), hence the term “electric filed-confined strategy.” Strong chemical bonds may be formed between TBT and PAN due to cross-linking reactions (26). The continuous and layer-by-layer preparation process ensures uniform

distribution, 3D connectivity, and mechanical strength (Fig. 1B). The subsequent thermal treatment in terms of preoxidation and carbonization converts the TBT clusters into  $\text{TiO}_x\text{C}_y$  particles (figs. S2 to S4). An obvious and well-defined carbon shell can be found on the outside of the  $\text{TiO}_x\text{C}_y$  cluster (Fig. 1C and fig. S5). This means that the  $\text{TiO}_x\text{C}_y$  cluster is tightly fused with carbon. The multiscale microscopy observation (Fig. 1, D to G) demonstrates that abundant single atomic Ti and sub-3-nm  $\text{TiO}_x\text{C}_y$  clusters are highly dispersed in the interconnected nanofiber matrix, thus forming the desired 3D arrangement structure. These single atomic Ti and  $\text{TiO}_x\text{C}_y$  clusters stemmed from the TBT molecule seeds that were highly dispersed in/on CNs at the atomic level confined by the electric field during the DESP process (see figs. S6 and S7 for further aberration-corrected high-angle annular dark-field imaging (HAADF)-scanning transmission electron microscopy (STEM) characterization of the cross sections of as-spun and pre-oxidized samples). These single-atom Ti seeds were then converted to single atomic Ti and  $\text{TiO}_x\text{C}_y$  clusters by subsequent heat treatment. Thereby, a self-supported  $\text{TiO}_x\text{C}_y$  membrane (fig. S8) containing highly reactive single atomic  $\text{TiO}_x\text{C}_y$  was successfully prepared without using any binder.

Clearly, the interior of the nonsolid  $\text{TiO}_x\text{C}_y$  cluster particles comprise numerous single atomic Ti (Fig. 1F) and sub-3-nm  $\text{TiO}_x\text{C}_y$  clusters (fig. S9). Moreover, the CNs were found to be hollow based on the focused ion beam-scanning electron microscope (FIB-SEM) views (Fig. 1D and fig. S10) and transmission electron microscopy (TEM) observation (Fig. 1E). The three black holes in Fig. 1E correspond to the hollow CNs. The hollow structure of the CNs gives rise to a larger specific surface area and more active catalytic sites. A lot of Ti single atoms and  $\text{TiO}_x\text{C}_y$  lattices were found in the hollow CNs (fig. S9). Even inside the CNs far away from the  $\text{TiO}_x\text{C}_y$  clusters are spread with single atomic Ti (Fig. 1G and fig. S11). This further supports that the seeds of single atomic Ti were highly dispersed in the CNs by the strong electrostatic field force during DESP, rather than transferred from the  $\text{TiO}_x\text{C}_y$  clusters. The  $\text{TiO}_x\text{C}_y$  lattice was confirmed by x-ray diffraction (XRD; Fig. 1H) and can also be observed on the wall of the hollow CNs (fig. S11). Furthermore, x-ray absorption spectroscopy characterization was performed. The x-ray absorption near-edge structure (Fig. 1I) and extended x-ray absorption fine structure (Fig. 1J) spectra at the Ti K edge further support the presence of single atomic Ti and the valence state of Ti less than +4 in the  $\text{TiO}_x\text{C}_y$  membrane (see more details in section S1 and table S1) (27, 28). Such a hierarchical 3D porous network, with ubiquitously and abundantly distributed Ti single atoms and sub-3-nm  $\text{TiO}_x\text{C}_y$  lattices/clusters, results in ultrahigh-specific surface area and ultrahigh catalytic activity.

Furthermore, at the junctions of the hollow CNs and clusters as well as on the inner walls of hollow CN (fig. S9),  $\text{TiO}_x\text{C}_y$  and TiC lattice were observed. Even in the outermost layers of the carbon-based shell  $\text{TiO}_x\text{C}_y$  can be observed (fig. S12). Moreover, the TEM view (Fig. 1E) and energy dispersive spectrometer (EDS) mapping results (Fig. 1C) revealed that the hollow CN has been completely fused with the carbon shell of the  $\text{TiO}_x\text{C}_y$  cluster. This is further demonstrated by the magnified aberration-corrected HAADF-TEM (fig. S13), where the interface between the  $\text{TiO}_x\text{C}_y$  main core and the carbon shell within the cluster particle is continuous. These all mean that with the deep embedment of Ti single atoms and  $\text{TiO}_x\text{C}_y$  lattices into the CNs and carbon shell, a complete and strong fusion of “ $\text{TiO}_x\text{C}_y$ @CN” was achieved, ensuring a robust covalent bonding. This covalent bonding can

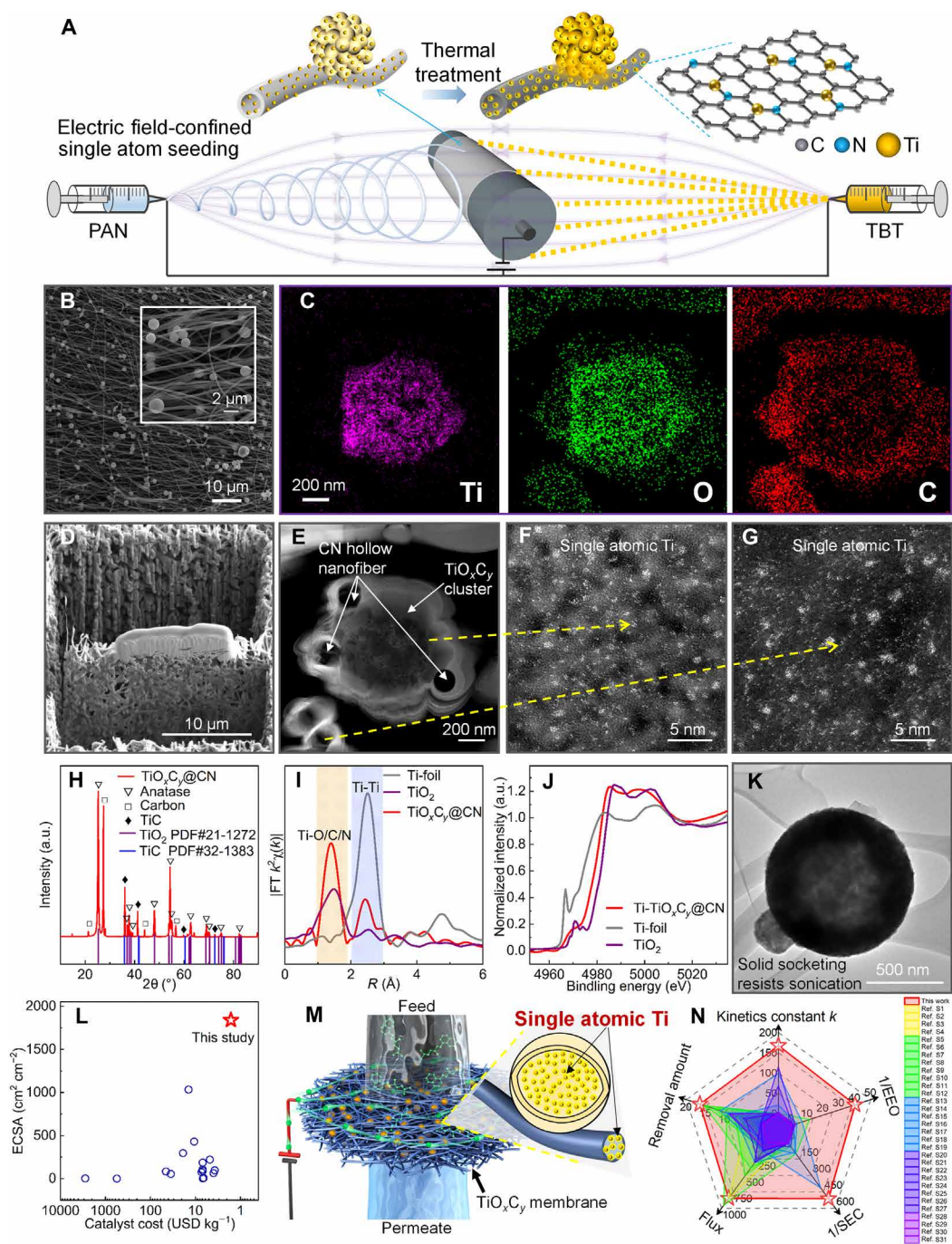


**Fig. 1. Efficient preparation of single atomic  $\text{TiO}_x\text{C}_y$  membrane that enables highly efficient electrocatalysis.** (A) Illustration of the dual electrospinning-electrospraying (DESP) synthetic fabrication strategy via electric field-confined single-atom seeding. (B) Scanning electron microscope (SEM) view of the 3D  $\text{TiO}_x\text{C}_y$  clusters highly distributed in a CN alveoli-like network (designated as  $\text{TiO}_x\text{C}_y$  membrane). (C) Energy dispersive spectrometer (EDS) elemental mapping showing the fused structure of the  $\text{TiO}_x\text{C}_y$  cluster. (D) Focused ion beam (FIB)-SEM view showing the 3D structure of the  $\text{TiO}_x\text{C}_y$  membrane: 3D highly dispersed  $\text{TiO}_x\text{C}_y$  clusters in a 3D CN network. (E) Further zoomed-in STEM image showing that the CN is hollow and fused to the cluster. (F) Single atomic Ti and  $\text{TiO}_x\text{C}_y$  were observed inside the clusters by aberration-corrected HAADF-STEM. (G) Further microscopic imaging by aberration-corrected HAADF-STEM of the CNs showing the presence of single atomic Ti in the hollow CN, even the CNs away from the  $\text{TiO}_x\text{C}_y$  clusters are spread all over with single atomic Ti. (H) XRD showing the presence of  $\text{TiO}_x\text{C}_y$ ,  $\text{TiO}_{2-x}$ , and TiC. (I) X-ray absorption near-edge structure (XANES) and (J) extended X-ray absorption fine structure (EXAFS) spectra at the Ti K edge for Ti- $\text{TiO}_x\text{C}_y$  membrane, Ti foil, and  $\text{TiO}_2$ . (K) TEM image after an ultrasonication treatment of  $\text{TiO}_x\text{C}_y$  membrane demonstrating the robust bond between the  $\text{TiO}_x\text{C}_y$  and CN, while the CN has been broken. (L) Comparison in terms of ECSA and cost between the prepared  $\text{TiO}_x\text{C}_y$  membrane with different electrocatalysts reported in literature (table S2). (M) Schematic illustrating the ultraefficient electrocatalytic water purification process. The enlarged schematic shows the highly distributed single atomic Ti. (N) Radar chart comparing the electrocatalytic efficiency between this work and other published studies (listed in table S3). EEO, electrical energy per order; a.u., arbitrary unit.

endow the membrane with a higher overall strength than simple physical contact. The strong binding between the  $\text{TiO}_x\text{C}_y$  and CN was further verified through the ultrasonication treatment (a commonly used way to disperse and separate materials) of  $\text{TiO}_x\text{C}_y$  membrane before the TEM observation (Fig. 1K). Even an intense sonication that breaks the nanofibers cannot break off the strong bonding between the  $\text{TiO}_x\text{C}_y$  and CN. It is noteworthy that the TiC and  $\text{TiO}_x\text{C}_y$  are electrically conductive phases (29), which ensures the localized ultrahigh-speed electron transfer between the  $\text{TiO}_x\text{C}_y$  catalytic sites and CNs. Electron transfer capability was directly assessed by measuring the conductivity of membranes (fig. S14). The  $\text{TiO}_x\text{C}_y$  membrane maintained a high conductivity comparable with that of the CN membrane.

By comparing with other published electrocatalytic electrodes in terms of ECSA and materials cost, it can be found that the  $\text{TiO}_x\text{C}_y$  membrane achieved a record-high ECSA at a very low cost (Fig. 1L and table S2). The high ECSA should be mainly attributed to the single atomic Ti, which cannot be achieved by the CN membrane alone. Waterborne toxins (e.g., perfluorinated compounds, disinfection byproducts, pharmaceuticals, personal care, and cosmetic products) severely affect human health and ecosystems (30). However, the current prevailing water treatment processes (e.g., aerobic activated sludge processes) cannot guarantee the adequate removal of emerging pollutants (7). Here, we used the prepared  $\text{TiO}_x\text{C}_y$  membrane as an anode in the electrocatalytic membrane filtration (EMF) water purification process (Fig. 1M; see detailed system configuration in fig. S15) to test its electrocatalytic degradation performance. Propranolol (PRO) was used as a representative emerging pollutant for the tests.

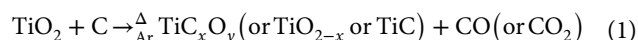
As expected, the  $\text{TiO}_x\text{C}_y$  membrane exhibited an ultraefficient electrocatalytic degradation capability during the high-permeability [ $\sim 8370 \text{ liter m}^{-2} \text{ hour}^{-1} \text{ bar}^{-1}$ , 1.25 s of hydraulic retention time (HRT)] one-time contact filtration tests (Fig. 1N and fig. S16A). The efficiency of water purification refers to the ratio of the beneficial output (e.g., pure water production, pollutant degradation, etc.) to the consumptive input (e.g., energy, materials, time, etc.). We systematically compared the EMF efficiency of the  $\text{TiO}_x\text{C}_y$  membrane with other previously published studies (listed in table S3) on the basis of five metrics, including the amount of pollutants removed [ $\text{g m}^{-2} \text{ hour}^{-1}$ , used as a more comparable index than the removal rate (%) among different studies], kinetic rate ( $k$ ,  $\text{min}^{-1}$ ), 1/electrical energy per order (1/EEO,  $\text{m}^3 \cdot \text{order kWh}^{-1}$ ), 1/specific energy consumption (1/SEC,  $\text{g pollutant kWh}^{-1}$ ), and water flux ( $\text{liter m}^{-2} \text{ hour}^{-1}$ ). For each index, a larger value indicates a higher efficiency. As demonstrated in Fig. 1N, the  $\text{TiO}_x\text{C}_y$  membrane achieved superior efficiency, with all five indices (especially for the energy consumption-related indices, i.e., 1/EEO and 1/SEC) reaching the top level. The low-energy consumption (EEO and SEC) is enabled by the high electrocatalytic efficiency and high water flux of the  $\text{TiO}_x\text{C}_y$  membrane. Unlike the other previously reported membranes that had at least one shortcoming, the  $\text{TiO}_x\text{C}_y$  membrane exhibited comprehensively superior electrocatalytic performance. This performance could be mainly attributed to the single atomic Ti prepared by the electric-filed-confined DESP process, which cannot be achieved by the CN membrane alone. The used  $\text{TiO}_x\text{C}_y$  membrane after an electrocatalytic treatment was also characterized by FIB-SEM and aberration-corrected HAADF-STEM. The hierarchical single atomic structure of the membrane remained unchanged (fig. S17).

### Ultraefficient electrocatalysis owes to ultrahigh ECSA, electrocatalytic defects, and fused bond

ECSA is one of the most important metrics for evaluating electrode performance, representing the electrochemically active surface area normalized by the geometric area of the electrode. The assessment of ECSA plays a pivotal role in the realm of electrocatalysis (31). As shown in Fig. 2A, The  $\text{TiO}_x\text{C}_y$  membrane exhibited an exceptional ECSA of  $1840 \text{ cm}^2 \text{ cm}^{-2}$ . This value is indicative of a markedly increased availability of active sites, which is a key determinant in boosting the electrocatalytic efficacy of materials. For comparison, the ECSA of the control  $\text{TiO}_2$ -dip-coating@CP [i.e., prepared by loading commercial  $\text{TiO}_2$  nanoparticles (P25) onto commercial carbon paper (CP)] was measured to be  $17.5 \text{ cm}^2 \text{ cm}^{-2}$ , which is two orders of magnitude lower. Compared with other reported electrocatalysts, including both metal oxides [e.g.,  $\text{TiO}_2$  (32), CuO (17), and  $\text{Co}_{3-x}\text{O}_4$  (22)] and more expensive noble metals [e.g., Pd/Au (13), and Pt (33)], the  $\text{TiO}_x\text{C}_y$  membrane demonstrated the highest ECSA (Fig. 1L). The  $\text{TiO}_x\text{C}_y$  membrane also has a high Brunauer-Emmett-Teller (BET)-specific surface area of  $109.5 \text{ m}^2 \text{ g}^{-1}$  (equivalent to  $7600 \text{ m}^2 \text{ m}^{-2}$ ; Fig. 2B) and sub-3-nm-sized pores [ $\sim 0.54 \text{ nm}$ , possible nanoconfinement effect (Fig. 2C) (34)].

In addition to the ultrahigh ECSA, the high reactivity of the electrocatalytic sites is also critical. Compared with  $\text{TiO}_2$ ,  $\text{TiO}_x\text{C}_y$  normally has a greater conductivity and exhibits higher catalytic activity (35). With the optimized fabrication conditions, we successfully created highly reactive oxygen defect structures in the sub-3-nm particles. As demonstrated in Fig. 2D, the presence of oxygen lattice defects was successfully verified by the strong electron paramagnetic resonance (EPR) signal around  $g = 2.0023$  (35, 36), which was not detected in the control CN and P25/CN (fig. S1C; blended electrocatalysts) membranes. Moreover, a positive shift of the Ti-O binding energy was identified by comparing the x-ray photoelectron spectroscopy (XPS) spectra (fig. S18) between the  $\text{TiO}_x\text{C}_y$  membrane and commercial  $\text{TiO}_2$  (nominated as P25) particles, implying the existence of oxygen defects that could lead to reduced electron cloud density and increased binding energy (35). While XPS was based on the whole  $\text{TiO}_x\text{C}_y$  membrane sample, the high-resolution EDS analyses only focused on the  $\text{TiO}_x\text{C}_y$  nanoparticles. An atomic Ti:O ratio of 1:1.5 (higher than the 1:2 ratio measured on P25) by high-resolution EDS (fig. S3) indicated the existence of oxygen defects and reduced valence Ti-cations ( $\text{Ti}^{3+}$  instead of  $\text{Ti}^{4+}$ ). The Raman spectra (fig. S19) also suggested the presence of  $\text{TiO}_x\text{C}_y$  and CN in the membranes (37).

The  $\text{TiO}_x\text{C}_y$  and its fused structure were created by the DESP and subsequent preoxidation and carbonization processes (fig. S1A). The formation of these structures can be ascribed to the carbonization stage (fig. S20), where the carbothermal reduction of  $\text{TiO}_2$  could produce  $\text{TiO}_x\text{C}_y$ ,  $\text{TiO}_{2-x}$ , and TiC (38)



The generation of  $\text{TiO}_x\text{C}_y$ ,  $\text{TiO}_{2-x}$ , or TiC may depend on the localized ratio of  $\text{TiO}_2$ /carbon (38). In general, high temperature ( $>900^\circ\text{C}$ ) is required for the occurrence of the reactions above (38). However, in our preparation ( $900^\circ\text{C}$ ), carbothermal reduction in Ar cover gas occurred more easily as the liquid organic titanium (TBT) was used as a precursor. Besides, DESP resulted in dense single atomic Ti seeds in the carbon fiber substrate, thus increasing the surface area (see more discussion in section S2). In particular, the fused structure

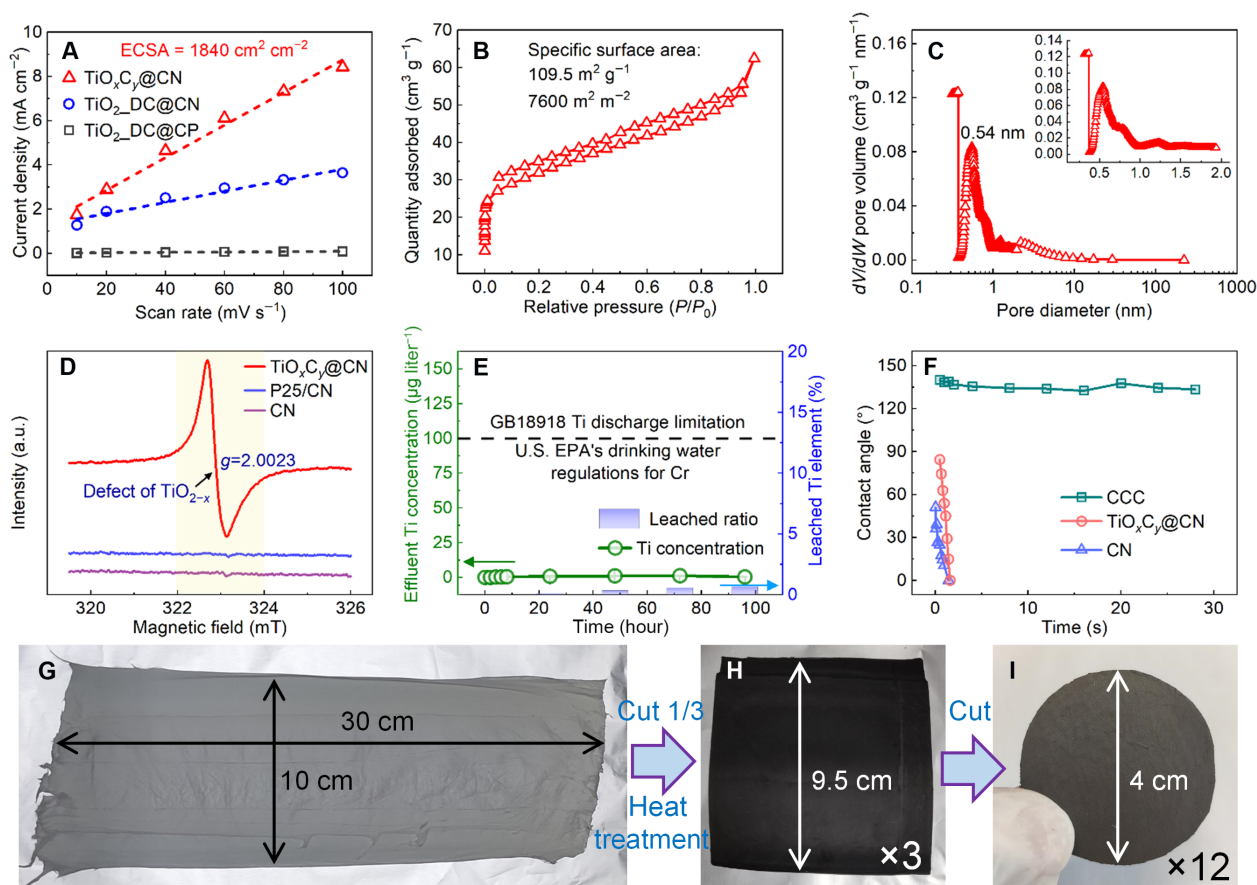


**Fig. 2. Ultrahigh ECSA, electrocatalytic defects, and fused bond of the TiO<sub>x</sub>C<sub>y</sub> membrane.** (A) Measured ultrahigh ECSA, (B) specific surface area, and (C) hierarchical pore size distribution of the TiO<sub>x</sub>C<sub>y</sub> membrane. The compared TiO<sub>2</sub>\_DC@CN and TiO<sub>2</sub>\_DC@CP were prepared by loading commercial TiO<sub>2</sub> nanoparticles (P25) onto CN or commercial CP using the dip coating (DC). (D) Measured EPR spectra that indicate the existence of TiO<sub>2-x</sub> defects in TiO<sub>x</sub>C<sub>y</sub> membrane (see more chemistry analyses in figs. S3 and S18, and section S2). (E) Effluent Ti concentration (μg liter<sup>-1</sup>) and Ti leaching mass ratio (%) over the total titanium of the TiO<sub>x</sub>C<sub>y</sub> membrane during the electrocatalytic degradation process. Two standards are referenced here: (i) Ti discharge concentration of 100 μg liter<sup>-1</sup> required by GB18918 (39) and (ii) Cr concentration of 100 μg liter<sup>-1</sup> required by the U.S. Environmental Protection Agency (U.S. EPA) drinking water standard (the latter is far more toxic than Ti) (40). (F) Comparison of wetting behavior among the TiO<sub>x</sub>C<sub>y</sub>, CN, and commercial carbon cloth (CCC) membranes. Representative photographs of (G) the as-spun and (H) carbonized samples, and (I) the self-supported TiO<sub>x</sub>C<sub>y</sub> membrane (~0.35 mm in thickness) used in the EMF experiments. At the laboratory stage, 12 membranes as shown in (I) can be fabricated by a single DESP process.

was formed as a result of TBT liquid mist beating against carbon polymer (PAN) nanofibers under a strong electrostatic force. The mechanism of generation of these fused structures between single atomic TiO<sub>x</sub>C<sub>y</sub>, and carbon substrates highlights a new approach to simultaneously enhance the effective active sites, local electronic conductivity, and mechanical robustness of electrocatalytic electrodes.

The robust fused bonding structure of TiO<sub>x</sub>C<sub>y</sub> membrane resulted in high erosion and corrosion resistance. The sub-3-nm TiO<sub>x</sub>C<sub>y</sub> particles in the electrodes were hardly detached during use, which ensures a stable electrocatalytic process and safe purified water. As shown in Fig. 2E, trace Ti element of up to 1.18 μg liter<sup>-1</sup> was detected in the effluent during the EMF tests. This is a very safe concentration, much lower than the Ti discharge concentration required by GB18918 (39) of 100 μg liter<sup>-1</sup>, or the US Environmental Protection Agency drinking water standard concentration of 100 μg liter<sup>-1</sup> for chromium (40) (the latter is far more toxic than Ti). After the 96-hour test, the Ti element loss was evaluated to be less than ~0.66% over the total titanium of the TiO<sub>x</sub>C<sub>y</sub> membrane.

Moreover, the TiO<sub>x</sub>C<sub>y</sub> membrane turns out to be highly hydrophilic (Fig. 2F and fig. S21), which is beneficial to the electrocatalytic reactions during the filtration process (41) in the aqueous system. The high hydrophilicity of the TiO<sub>x</sub>C<sub>y</sub> membrane should be attributed to both of its higher surface energy (contributed by C=O, C-OH, and Ti-O components) and hierarchical porous structure (enables Wenzel contacting thus enhanced hydrophilicity). The TiO<sub>x</sub>C<sub>y</sub> membrane contains abundant C=O and C-OH groups (C 1s; fig. S4B). The surface density of -OH was measured to be 2.48 × 10<sup>-7</sup> mol cm<sup>-2</sup> by a toluidine blue O (TBO) colorimetric method, which was more than twice that of the Magnéli phase Ti<sub>4</sub>O<sub>7</sub> (1.2 ± 0.23 × 10<sup>-7</sup> mol cm<sup>-2</sup>) (42). Besides, the membrane had an effective pore size of 350 nm (belonging to the microfiltration category), which was measured by a series of microparticle rejection tests (more details in section S3 and fig. S16). This porous structure would give rise to a minor filtration resistance and could also facilitate mass transfer. The TiO<sub>x</sub>C<sub>y</sub> membrane has a hierarchical structure that includes 350-nm pores formed by CNs interlacing and

0.5- to 2-nm gap pores between the ~2-nm  $\text{TiO}_x\text{C}_y$  particles. This hierarchical structure could stimulate the capillary effect during water transport, allowing water and the contaminants entrained in it to achieve rapid mass transfer and reaction through the membrane.

After conducting a preliminary assessment of fabrication cost and prospect for practical scalability, we determined that the DESP strategy is conducive to scaling up for large-area membrane production at low cost (section S4). At the laboratory stage, we have already been able to prepare  $\text{TiO}_x\text{C}_y$  samples as large as 30 cm by 10 cm (Fig. 2G) in a single DESP process, which ultimately results in three carbonized samples of 9.5 cm by 9.5 cm as Fig. 2H and 12 membranes with a diameter of 4 cm as Fig. 2I. Combined with a larger electrostatic spinning equipment and a large-scale heat treatment line, it is expected that more and larger membranes can be easily produced at the scale-up stage. Although the DESP strategy has achieved the successful preparation of high-performance single atomic electrocatalytic membrane based on TBT and PAN, it also shows potential in the preparation of other types of single atomic catalysts. However, the dependent molecular raw materials still need to be further screened and optimized, which needs to be investigated by subsequent studies.

### Integrated direct and indirect oxidation accounts for the ultraefficient electrocatalysis

As demonstrated in Fig. 3A, the PRO (20 mg liter<sup>-1</sup>) removal rates by the  $\text{TiO}_x\text{C}_y$  membrane at 0 V varied within a low range of 2 to 3%.

This minor removal could be ascribed to the physical adsorption. In contrast, as a 3-V cell voltage was applied, the  $\text{TiO}_x\text{C}_y$  membrane instantly achieved a high removal rate of ~96% (1.4 log removal, much higher than those for the control P25/CN, vacuum filtration–P25@CN, and CN membranes; see additional comparison with more control membranes in section 5) and maintained above 96% during the purification period. Similar continuous ~100% degradation performance was also observed at PRO (2 mg liter<sup>-1</sup>) (fig. S22), indicating a prominent electrocatalytic performance. Further analysis for degradation products via high-performance liquid chromatography (HPLC)–mass spectrometry (MS)/MS (fig. S23, A to E) revealed that most PRO were degraded with few intermediate products. After the applied 3-V voltage was cut off at 35 min, no extra increase in the effluent PRO concentration beyond the influent value was observed, and the removal rate soon decreased to the same level as the 0-V test (fig. S23C). The effluent conductivity and pH conditions also remained considerably stable during filtration (fig. S23D). These results implied that the contribution by electrosorption to the rapid PRO removal was negligible (43).

Accordingly, the primary cause of pollutant removal is electrocatalytic degradation rather than adsorption or electrosorption. Direct in situ electron transfer oxidation by the oxidative centers (e.g., oxidative holes  $h^+$  excited by electron transfer) (44–46) and indirect oxidation by generated reactive oxygen species (ROS) (e.g.,  $\cdot\text{OH}$ ,  $\text{SO}_4^{2-\cdot}$ ,  $^1\text{O}_2$ , etc.) are usually recognized as two predominant paths of electrocatalytic pollutant degradation (47). We conducted three series of

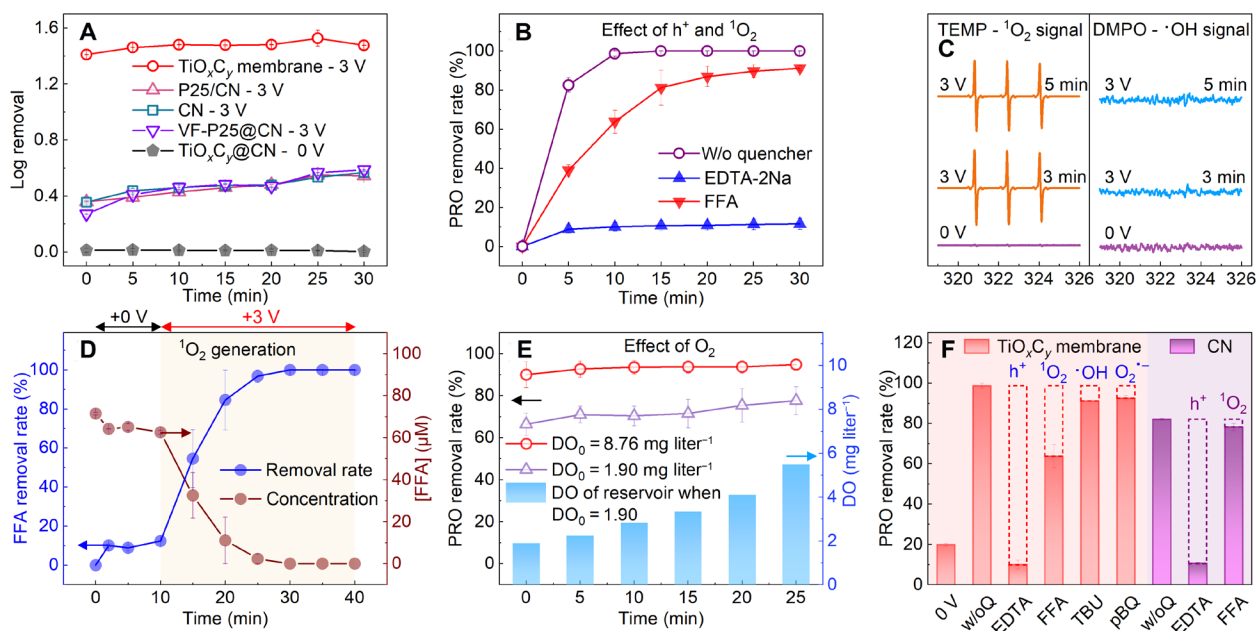


**Fig. 3. Revealing the mechanism of the ultraefficient electrocatalytic performance of the  $\text{TiO}_x\text{C}_y$  membrane.** (A) Comparison of electrocatalytic performance in terms of PRO removal rate among different electrodes [i.e.,  $\text{TiO}_x\text{C}_y$ , commercial  $\text{TiO}_2$  nanoparticles (P25)/CN, vacuum filtration (VF)–P25@CN, and CN; see details in section S5). (B) Quenching tests revealing the effect of oxidative holes [ $h^+$ , quenched by 100 mM disodium EDTA-2Na (EDTA-2Na)] and singlet oxygen [ $^1\text{O}_2$ , quenched with 100 mM furfuryl alcohol (FFA)] on the degradation of PRO (20 mg liter<sup>-1</sup>) during a cyclic EMF process (3-V cell voltage). (C) EPR spectra exploring the existence of  $^1\text{O}_2$  and  $\cdot\text{OH}$  using 100 mM 2,2,6,6-tetramethyl-4-piperidone (TEMP) and 100 mM 5,5-dimethyl-1-pyrroline *N*-oxide (DMPO) as the trapping agents, respectively. (D) Further probe test demonstrating the generation of  $^1\text{O}_2$  through the degradation of 67.6  $\mu\text{M}$  FFA by the  $\text{TiO}_x\text{C}_y$  membrane. (E) Effect of dissolved oxygen concentration on the continuous PRO degradation by the  $\text{TiO}_x\text{C}_y$  membrane. (F) Comparison of the PRO removal rates among different EMF tests without the quencher (denoted as w/oQ) or with different quenchers, including EDTA-2Na, FFA, tert-butanol (TBU), and *p*-benzoquinone (pBQ), which screened out oxidation by  $h^+$ ,  $^1\text{O}_2$ ,  $\cdot\text{OH}$ , and  $\text{O}_2^{\cdot-}$ , respectively. The reduced portions marked with the dotted boxes indicate the amounts degraded by the quenched oxidants, thus revealing the contribution ratios of different oxidants to pollutant degradation.

tests, including quenching, EPR, and probe tests, to systematically reveal the mechanism behind the electrocatalytic degradation.

As shown in Fig. 3B, the addition of ethylenediaminetetraacetic acid disodium salt (EDTA-2Na, able to quench  $h^+$ ) (48) led to a notable reduction in the PRO removal rate. Similar reductions were also observed in two confirmatory tests that used ammonium oxalate (AO) as the quencher (fig. S24) and cimetidine (CMT) as the pollutant (fig. S25). These results all verified the predominant contribution of direct electron transfer oxidation to the degradation of the pollutants (49). In addition, the addition of furfuryl alcohol (FFA, able to quench singlet oxygen  $^1O_2$ ) (50) resulted in delayed PRO degradation and a decreased removal rate (Fig. 3B), demonstrating that PRO degradation could be ascribed to indirect oxidation by  $^1O_2$ . Moreover, EPR detection revealed the typical signals of 2,2,6,6-tetramethyl-4-piperidone (TEMP)-captured  $^1O_2$  (Fig. 3C) (51), which persisted throughout the EMF process, thus directly verifying the presence of  $^1O_2$ . Furthermore, the direct probe test with trace FFA (67.6  $\mu\text{M}$ , far less than the 100 mM used in the quenching test) that could selectively react with  $^1O_2$  at  $1.2 \times 10^8 \text{ M}^{-1} \text{ s}^{-1}$  also confirmed the efficient production of  $^1O_2$  (Fig. 3D). In addition, we found that the reduction of influent dissolved oxygen (DO) concentration led to a decrease of PRO removal rate by 24% (Fig. 3E). This rate is similar to the contribution ratio of  $^1O_2$  oxidation to the PRO removal. Thus, the generation of  $^1O_2$  was closely related to the concentration of DO (Fig. 3E and more details in section S6). Further quenching and EPR tests (Fig. 3C, see more details in sections S7 and S8, and fig. S26) demonstrated that the generation of  $\cdot\text{OH}$ ,  $\text{O}_2^{\cdot-}$ , and  $\text{SO}_4^{2\cdot-}$  was minor.

The contribution ratio of each direct and indirect oxidation mechanisms ( $h^+$ ,  $^1O_2$ ,  $\cdot\text{OH}$ , and  $\text{O}_2^{\cdot-}$ ) to PRO degradation was calculated on the basis of the data at 10 min of the quenching tests. As demonstrated

in Fig. 3F, the PRO degradation by the  $\text{TiO}_x\text{C}_y$  membrane can be mainly attributed to the direct electron transfer oxidation and indirect oxidation by  $^1O_2$ . The contribution ratios of  $\cdot\text{OH}$  and  $\text{O}_2^{\cdot-}$  were both less than 8%. In marked contrast, the degradation by the CN membrane was almost exclusively ascribed to direct electron transfer oxidation. Apparently, the  $\text{TiO}_x\text{C}_y$  membrane performed much better than CN membrane alone in producing  $^1O_2$ , which was most likely due to the presence of single atomic Ti and  $\text{TiO}_x\text{C}_y$  clusters as active sites. The generation of  $^1O_2$  might be related to the electrocatalytic conversion of dissolved  $\text{O}_2$  by single atomic  $\text{TiO}_x\text{C}_y$  (52, 53).

### Sub-3-nm cluster structure evokes superior electrocatalytic degradation

To help explore the mechanisms behind the superior electrocatalytic performance, a series of simulations were performed. Three typical microscopic models were established, representing the sub-3-nm cluster scenario (Fig. 4A), micron-sized particle scenario (Fig. 4B), and nanocluster-free scenario (Fig. 4C), respectively. As a result, it was observed that the sub-3-nm cluster structure enabled the fastest electrocatalytic degradation at the nanocluster-foulant interface ( $k_c$ ; Fig. 4, A to C;  $N_c$ , fig. S27, A to C), thus resulting in a substantially enhanced pollutant removal rate (Fig. 4, D to F). In addition, the incorporation of  $\text{TiO}_x\text{C}_y$  sub-3-nm cluster promoted the transfer of the reactive center from the surface of the nanofiber to the surface of the nanoparticle (Fig. 4, A to C, and fig. S27), where more electrocatalytic sites were conspicuously present. This gave rise to a further increase in the pollutant removal rate (Fig. 4, D to F, and fig. S27, A to C). Furthermore, the unique hierarchical structure of the “nanofiber-nanocluster” of the  $\text{TiO}_x\text{C}_y$  membrane also enhanced the hydraulic mass transfer (fig. S28 and more details in section S9).

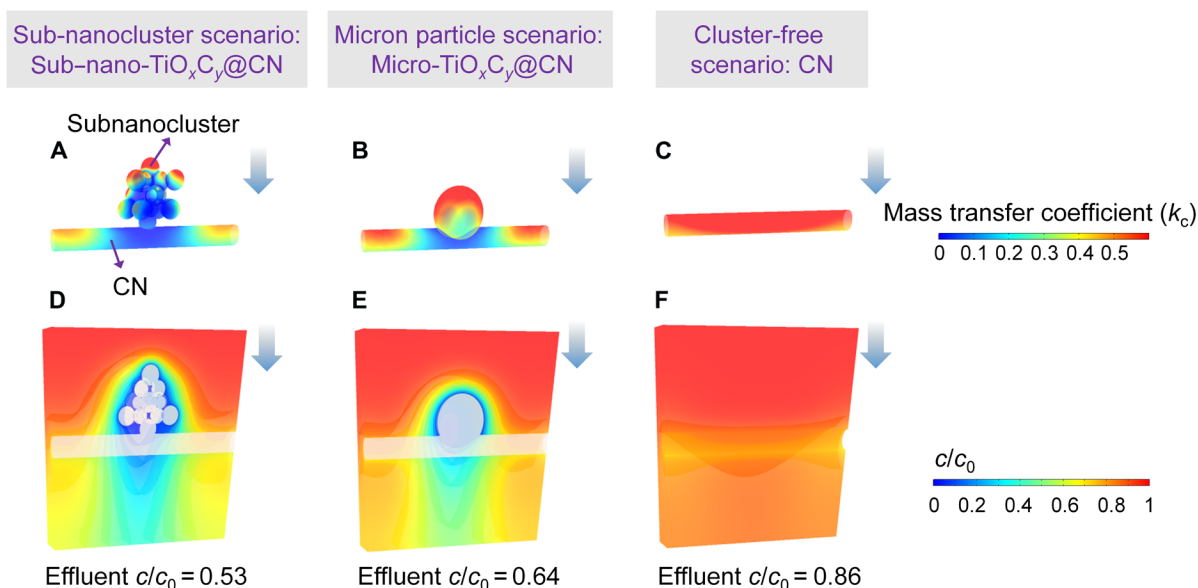


**Fig. 4. Simulation analyses revealing the advantage of the nanocluster structure of the  $\text{TiO}_x\text{C}_y$  membrane for electrocatalytic degradation.** (A to C) Comparison of the computed distribution of the pollutant mass transfer coefficient ( $\text{mm s}^{-1}$ ) adjacent to the membrane surface among three representative models: (A) sub-nano- $\text{TiO}_x\text{C}_y$  membrane segment, (B) micro- $\text{TiO}_x\text{C}_y$  segment, and (C) CN segment. (D to F) Comparison of the computed distribution of pollutant concentration ( $c/c_0$ ) in the outer area among the (D) sub-3-nm  $\text{TiO}_x\text{C}_y$ , (E) micro- $\text{TiO}_x\text{C}_y$ , and (F) CN segments. The total mass of the sub-3-nm  $\text{TiO}_x\text{C}_y$  cluster in (A) and (D) is equal to the mass of a single  $\text{TiO}_x\text{C}_y$  particle in the model corresponding to (B) and (E).

## Hierarchical structure ensures multidimensional degradation of pollutants

As discussed above, the 3D  $\text{TiO}_x\text{C}_y$  membrane imparts an ultraefficient electrocatalytic water purification, owing to the ultrahigh-specific surface area, sufficient and highly dispersed single atomic Ti, excellent contact by enveloping, and enhanced mass transfer. Such a hierarchical structure enables the multidimensional degradation of pollutants.

Specifically, as illustrated in Fig. 5A, the unobstructed electron migration along the nanofiber and the  $\text{TiO}_x\text{C}_y$  incessantly produces a large number of highly oxidative holes ( $\text{h}^+$ ). They act similarly to landmines (Fig. 5B), ensuring that the pollutants in contact with them are directly and efficiently degraded. Correspondingly, by virtue of its large-specific surface area and abundant defect structures, the  $\text{TiO}_x\text{C}_y$  membrane constructs a dense and regenerative barrier for the removal of pollutants. In addition, its fibrous structure stirs up the flow (fig. S28G; thereby enhancing convection mass transfer) and also increases the chance of pollutants coming into contact with  $\text{h}^+$ . Furthermore, owing to the fast migration of electrons, the widely distributed single atomic  $\text{TiO}_x\text{C}_y$  ensures the efficient production of  $^1\text{O}_2$  by electrocatalytic conversion of dissolved  $\text{O}_2$  (52, 53). They act similarly to longer-range assassins [with a longer lifetime than  $\cdot\text{OH}$  and many other active species (54)], thereby covering a wider area to further degrade the pollutants that could bypass the adsorptive capture and direct oxidation by  $\text{h}^+$ . In contrast, the conventional strategies for the P25/CN and

CN membranes suffer from impeded electron transfer (fig. S29A) and unidimensional degradation capability (fig. S29B).

The durability and treatment capacity of the  $\text{TiO}_x\text{C}_y$  membrane were evaluated. As shown in Fig. 5C, the membrane successfully retained a removal rate of  $\geq 95\%$  after a 600-min unceasing treatment with very low-energy consumption of approximately  $0.018 \text{ kWh}\cdot\text{m}^{-3}\cdot\text{order}^{-1}$ , without any conspicuous sign of performance deterioration. As presented in fig. S30, after the degradation experiments, the changes of the  $\text{TiO}_x\text{C}_y$  membrane in morphology, Raman spectra, and Fourier transform infrared spectra were minimal. The electrocatalytic capability of this membrane is versatile for a variety of pharmaceutical and personal care product pollutants. We selected four more representatives of pharmaceuticals and personal care products, including sulfamethoxazole (SMX), CMT, ciprofloxacin (CIP), and ranitidine (RTD), for the EMF tests. The obtained ultraefficient results (Fig. 5, D and E) were quite comparable with those for the PRO scenario, while the removal performance of P25/CN membrane, used as a control, was much lower (fig. S31). This shows that  $\text{TiO}_x\text{C}_y$  membrane can achieve high removal rates for various pollutants including hydrophilic and hydrophobic pollutants. When tested with mixed contaminants in complex practical wastewaters, the  $\text{TiO}_x\text{C}_y$  membrane still maintained a comparable performance (fig. S32).

Overall, the short-range, heterogeneous, energy-efficient, and instantaneous direct electron transfer oxidation and the long-range, homogeneous, unrestricted  $^1\text{O}_2$  oxidation by single atomic  $\text{TiO}_x\text{C}_y$  jointly build a multidimensional barrier against the coming pollutants. In

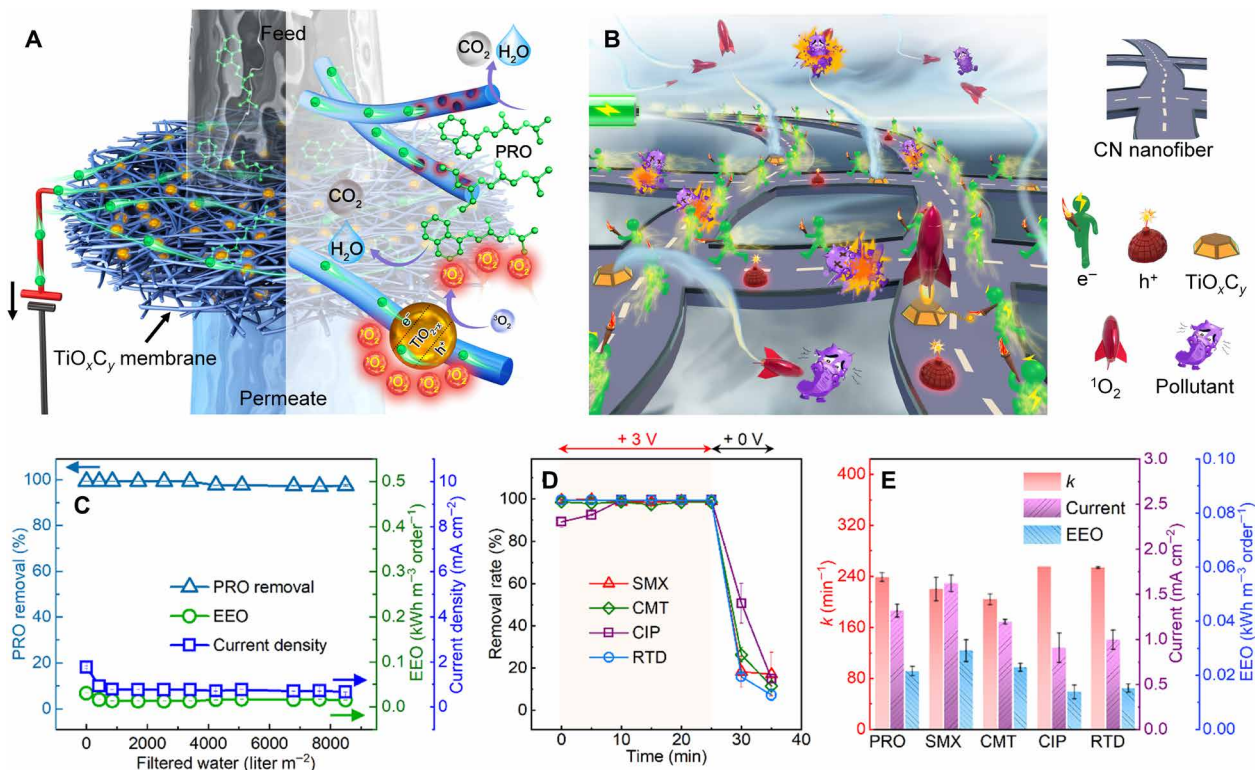


**Fig. 5. Highly scattered single atomic  $\text{TiO}_x\text{C}_y$  ensure multidimensional degradation of pollutants.** (A) Schematic demonstrating the efficient generation of  $\text{h}^+$  and  $^1\text{O}_2$  on the  $\text{TiO}_x\text{C}_y$  membrane during the EMF process. (B) Cartoon illustration of the multidimensional pollutant degradation by  $\text{TiO}_x\text{C}_y$  membrane. (C) Stability tests of the PRO degradation performance by the  $\text{TiO}_x\text{C}_y$  membrane at  $0.5 \text{ mg liter}^{-1}$ . (D) Versatility tests of the electrocatalytic degradation performance for different pollutants: sulfamethoxazole (SMX), CMT, ciprofloxacin (CIP), and ranitidine (RTD); all at  $2 \text{ mg liter}^{-1}$ . (E) Comparison of the degradation efficiency in terms of  $k$ , current density, and EEO among the different pollutants (i.e., PRO, SMX, CMT, CIP, and RTD).

general, the electrocatalysts of a single material or simple structure normally function using only one primary mechanism: either direct oxidation or indirect reactions by ROS. Considering that different types of pollutants have different sensitivities to direct oxidation and indirect oxidation (55), this multidimensional degradation promisingly offers a versatile capacity in degrading diverse types of pollutants (Fig. 5D). For  $\text{TiO}_x\text{C}_y$  membrane, we believe its unique hierarchical structure led to the intensification of both the direct and indirect oxidation processes, thereby inducing a coupling effect that leads to multidimensional electrolysis.

In summary, this study has developed a DESP strategy for the efficient fabrication of high-performance 3D SAC porous electrodes with ultrahigh ECSA. A  $\text{TiO}_x\text{C}_y$  filtration membrane composed of 3D highly scattered single atomic Ti and  $\text{TiO}_x\text{C}_y$  sub-3-nm clusters fused in highly interconnected CN network was successfully prepared. The strong fused bond can be owing to the generation of  $\text{TiO}_x\text{C}_y$  during the DESP and subsequent thermal treatment. These ultra-highly dispersed single atomic  $\text{TiO}_x\text{C}_y$  structures simultaneously enhance effective active sites, local electronic conductivity, and mechanical robustness. The obtained  $\text{TiO}_x\text{C}_y$  membrane achieves superior electrocatalytic performance with excellent energy efficiencies and erosion resistance. It was also revealed through systematic analyses that the 3D single atomic  $\text{TiO}_x\text{C}_y$  enabled the establishment of a multidimensional barrier against waterborne toxins, comprising short-range heterogeneous direct electron transfer oxidation and long-range homogeneous oxidation by  $^1\text{O}_2$  and other ROS ( $-\text{OH}$ ,  $\text{O}_2^{\cdot-}$ , etc.). The hierarchical structures simultaneously enhance the local catalytic activity, catalyst-to-collector bonding, and long-range electronic/chemicals transport. Overall, this strategy provides a general platform for designing high-performance electrocatalytic membranes via the construction of single atomic  $\text{TiO}_x\text{C}_y$ , that highly dispersed and tightly fused in a CN network in a low-cost and easy-to-scale-up manner. We envision that this fabrication strategy will lay a foundation for the future sustainable development of high-performance and multifunctional electrocatalytic 3D electrodes in diverse applications.

## MATERIALS AND METHODS

### Chemicals and materials

TBT ( $\geq 97\%$ ), PAN (weight-average molecular weight  $\sim 150,000$ ), PRO (hydrochloride), SMX, CIP, CMT, RTD, and P25 ( $\text{TiO}_2$ ) nanoparticles were purchased from Sigma-Aldrich (USA). *N,N*-dimethylformamide (DMF;  $> 99.9\%$ ), acetic acid ( $\geq 99.8\%$ ), acetonitrile ( $\geq 99.9\%$ ), TBU, *p*-benzoquinone (pBQ), buffered phosphate, FFA, terephthalic acid (TA), 2-hydroxyterephthalic acid (hTA), and AO were obtained from Shanghai Macklin Biochemical Co. Ltd. (Shanghai, China). TEMP and 5,5-dimethyl-1-pyrroline *N*-oxide (DMPO) were purchased from Meryer Co. Ltd. (Shanghai, China).  $\text{Na}_2\text{SO}_4$  and EDTA-2Na were purchased from Sinopharm Chemical Reagent Co. Ltd. (Shanghai, China). Titanium mesh was purchased from Zhuosheng Wire Mesh Co. Ltd. (Hangzhou, China) and was successively rinsed with deionized water and acetone before use. All the other chemicals and materials were used as received.

### Fabrication of the $\text{TiO}_x\text{C}_y$ membrane

The  $\text{TiO}_x\text{C}_y$  membrane was fabricated with the DESP synthetic strategy (Fig. 1A and fig. S1A). Specifically, the PAN solution [10% in DMF (w/v)] and TBT solution [8:3 in acetic acid (v/v)] were first

prepared as precursor solutions. Then, the PAN and TBT solutions were simultaneously drawn to a cylinder collector (rotating at a set speed of 2500 rpm) by an applied electric field in a laboratory electrospinning system (ET-3556H, Ucalery Co. Ltd., China). Because of different solution viscosities and properties (56), the PAN solution was spun as nanofibers (i.e., electrospinning), and the TBT solution was sprayed out in a mist (i.e., electro spraying). For both the electrospinning and electro spraying processes, the inner needle diameter, tip-to-collector distance, tip voltage, and collector voltage were set to 0.5 mm, 15 cm, 15 kV, and  $-7.5$  kV, respectively. The injection speeds of the electrospinning and electro spraying processes were set to  $1.5$  ml hour $^{-1}$  and  $1.34$  ml hour $^{-1}$ , respectively. After 10 hours of fabrication at  $40 \pm 10\%$  humidity and  $25^\circ \pm 5^\circ\text{C}$ , the obtained membrane precursor was detached and preoxidized in air at  $280^\circ\text{C}$  for 2 hours and then carbonized in Ar at  $900^\circ\text{C}$  for 1 hour. After cooling to room temperature, the preparation process of the  $\text{TiO}_x\text{C}_y$  membrane was completed. In addition, the control CN and P25/CN membranes were prepared following the same procedure but using different precursor solutions. The CN membrane was prepared only by electrospinning with the PAN solution (fig. S1B). For the P25/CN membrane, an additional 12 weight % P25 nanoparticles were added to the PAN solution before the electrospinning process (fig. S1C).

### Membrane characterizations

The microtopography and elemental distribution of the membranes were investigated by SEM (Zeiss Merlin Compact, Germany) and TEM (JEM-2100F, Japan). The membrane was cut by FIB-SEM (ZEISS Crossbeam 540, Germany) for internal cross-sectional observation with both the STEM and HAADF-STEM based on a double-corrected microscope (JEM-ARM300F, JEOL, Japan). The ECSA was derived from the double-layer capacitance (57), which was obtained by performing CV sweeps in a three-electrode electrochemical workstation at different scanning rates (section S10). The effective membrane pore size was evaluated with a series of microparticle rejection tests. The specific surface area and size distribution of nanopores were measured by a specific surface area and porosity analyzer (Autosorb-iQ2, Quantachrome Co. Ltd., USA). The BET specific surface area was also measured on the basis of  $\text{N}_2$  adsorption isotherm. The elemental compositions were characterized by XPS (ESCALAB 250Xi, Thermo Fisher Scientific, England). The crystal structures were investigated by XRD (D8/Aduance, Bruker, Germany). The Raman spectra were obtained using a Raman spectrometer (LabRAM HR Evolution, Horiba Co. Ltd., France) with a 532-nm laser. The EPR spectra were collected by an X-band EPR spectrometer (JES-FA200, JEOL, Japan) to detect oxygen vacancies of  $\text{TiO}_{2-x}$  membranes. Membrane conductivity was measured with a four-probe tester (280SJ, Four Dimensions, USA). The mechanical tensile strength was assessed by an electronic universal testing machine (Acumen 3, MTS Co. Ltd., USA). Membrane surface hydrophilicity was evaluated through water contact angle measurement using an optical instrument (OCA 20, DataPhysics, Germany). The density of the surface  $-\text{OH}$  groups was measured using the TBO colorimetric method (40).

### Electrocatalytic degradation tests

The electrocatalytic degradation experiments were performed with the EMF system (fig. S15), which comprised an EMF reactor with an effective filtration area of  $7$  cm $^2$ , a reservoir beaker, a peristaltic

pump, and an external power (SS-L303SPD, ABF, China). The electrocatalytic membrane and titanium mesh were installed ~1.5 mm apart in parallel in the filtration reactor and were used as the anode and cathode, respectively. The influent sequentially flowed through the membrane and titanium mesh for purification. A 3-V cell voltage (dc) was applied to initiate the electrocatalytic reactions during the EMF experiments. A series of individual pollutant solutions comprising 10 mM Na<sub>2</sub>SO<sub>4</sub> (as electrolyte) and one type of pollutant (i.e., PRO, SMX, CIP, CMT, or RTD; 2 mg liter<sup>-1</sup> unless specified) were prepared for the EMF tests.

For the investigations of the degradation performance, the EMF system was operated in a continuous flow mode where the effluent was not recycled back to the reservoir. The continuous mode only allows one-time contact between the foulants and membrane, which resembles practical treatment conditions. For most mechanism investigations, the system was operated in batch mode (unless specified) where the effluent was recycled back to the reservoir. In the batch mode, the samples were taken from the reservoir for measurements and analyses. The batch mode allows cycled collection of trace and short-lived ROS, thereby disclosing subtle differences among different tests.

### Quantifications of pollutant removal

The concentrations of PRO, SMX, CIP, RTD, CMT, FFA, TA, and hTA were determined using an HPLC instrument (Agilent 1200 LC) equipped with a C-18 column (Agilent Eclipse XDB-C18). The adopted eluent compositions (v/v, 0.1% phosphoric acid solution:acetonitrile) and the corresponding detection wavelengths were as follows: 70:30 and 218 nm for PRO, 60:40 and 270 nm for SMX, 82:18 and 278 nm for CIP, 90:10 and 312 nm for RTD, 90:10 and 218 nm for CMT, 80:20 and 220 nm for FFA, and 65:35 and 218 nm for TA. In particular, an additional fluorescent detector was used for the hTA measurement at  $\lambda_{\text{ex}} = 315$  nm and  $\lambda_{\text{em}} = 435$ . The flow rate and column temperature were set to 1.0 ml min<sup>-1</sup> and 30°C, respectively. The injection volume was adjusted from 5 to 50  $\mu\text{l}$  with the initial concentration of the pollutant. The chemical composition of the effluent was further analyzed with HPLC-MS/MS (Agilent, US) instrument (24) and inductively coupled plasma-MS (Agilent, US) instrument.

### Quantification of membrane filtration performance and electrocatalytic efficiency

The HRT(s) for electrocatalytic degradation was calculated as

$$\text{HRT} \frac{d}{J} \times 36,000 \quad (2)$$

where  $d$  (cm) is the thickness of the membrane and  $J$  (liter m<sup>-2</sup> hour<sup>-1</sup>) is the flux of membrane filtration. The apparent removal kinetic constant  $k$  was calculated by fitting the data to pseudo-first-order kinetics

$$\ln \frac{C}{C_0} = -kt_1 \quad (3)$$

where  $C$  (mg liter<sup>-1</sup>) and  $C_0$  (mg liter<sup>-1</sup>) indicate the effluent and influent pollutant concentrations, respectively, and  $t_1$  (min) refers to the HRT of the EMF process. The EEO (kWh·m<sup>-3</sup>·order<sup>-1</sup>) and SEC (kWh·g<sup>-1</sup> pollutant) were separately calculated as

$$\text{EEO} = \frac{UI \frac{t_2}{60} \times 10^{-3}}{V \log_{10} \left( \frac{C_0}{C} \right)} \quad (4)$$

$$\text{SEC} = \frac{UI \frac{t_2}{60} \times 10^{-3}}{V(C_0 - C)} \quad (5)$$

where  $U$  (V) is the applied cell voltage,  $I$  (A) is the measured current,  $t_2$  (min) is the reaction time, and  $V$  (m<sup>3</sup>) is the total influent volume involved in the reactions. The removal amount ( $R$ , g m<sup>-2</sup> hour<sup>-1</sup>) of pollutants was calculated as

$$R = \frac{V(C_0 - C)}{A \frac{t_2}{60}} \quad (6)$$

### Identification of ROS

Quenching, EPR, and probe tests were separately performed to identify the existence and effects of different oxidation mechanisms (i.e., h<sup>+</sup>, <sup>1</sup>O<sub>2</sub>, O<sub>2</sub><sup>·-</sup>, ·OH, etc.) in the electrocatalytic degradation process. All three tests were carried out in the batch mode (unless specified) at 3-V cell voltage.

Quenching tests were conducted to investigate the generation and effect of h<sup>+</sup>, <sup>1</sup>O<sub>2</sub>, O<sub>2</sub><sup>·-</sup>, ·OH, and ·OH<sub>ads</sub>. Different quenchers were separately added to the influent PRO solution [PRO (20 mg liter<sup>-1</sup>) and 10 mM Na<sub>2</sub>SO<sub>4</sub>] for electrocatalytic degradation experiments. EDTA-2Na and AO were separately used to quench h<sup>+</sup>. FFA, pBQ, TBU, and buffered phosphate were used to quench <sup>1</sup>O<sub>2</sub>, O<sub>2</sub><sup>·-</sup>, ·OH, and ·OH<sub>ads</sub>, respectively.

EPR tests were conducted to detect <sup>1</sup>O<sub>2</sub>, O<sub>2</sub><sup>·-</sup>, and ·OH by an X-band EPR spectrometer (JES-FA200, JEOL, Japan). A portion of TEMP was added to a 10 mM Na<sub>2</sub>SO<sub>4</sub> solution as the trapping agent of <sup>1</sup>O<sub>2</sub> (51). A portion of DMPO was added to a 10 mM Na<sub>2</sub>SO<sub>4</sub> solution as the trapping agent of ·OH (58). Specifically, for the detection of O<sub>2</sub><sup>·-</sup>, a 0.1-ml portion of the EMF effluent (containing 10 mM Na<sub>2</sub>SO<sub>4</sub>) was immediately transferred to a DMPO (in 10 ml of methanol) solution (59). The ERP spectra were recorded with a modulation frequency of 100 kHz, a modulation amplitude of 0.1 mT, a microwave power of 1 mW, a sweep width of 15 mT, and a sweep time of 120 s.

Probe tests were conducted to quantify <sup>1</sup>O<sub>2</sub> and ·OH (50). A trace amount of FFA (67.6  $\mu\text{M}$ ) was added to a 10 mM Na<sub>2</sub>SO<sub>4</sub> solution to capture the <sup>1</sup>O<sub>2</sub> via reaction during the EMF process. A trace amount of TA (100  $\mu\text{M}$ ) was added to a 10 mM Na<sub>2</sub>SO<sub>4</sub> solution to capture ·OH, which was then changed to hTA.

### Modeling and simulation

Three types of microscopic models were established using COMSOL Multiphysics 5.6, separately simulating the sub-3-nm-TiO<sub>x</sub>C<sub>y</sub> membrane segment, micro-TiO<sub>x</sub>C<sub>y</sub> segment, and CN segment (Fig. 4). The total mass of the TiO<sub>x</sub>C<sub>y</sub> particles in the sub-3-nm-TiO<sub>x</sub>C<sub>y</sub> model was set equal to that of the single TiO<sub>x</sub>C<sub>y</sub> particle in the micro-TiO<sub>x</sub>C<sub>y</sub> model. The distribution of the pollutant mass transfer coefficient ( $k_c$ , m s<sup>-1</sup>), pollutant concentration ( $c/c_0$ ), normal electric field intensity ( $E$ , V m<sup>-1</sup>), normal current density ( $I$ , A m<sup>-2</sup>), and mass flux of pollutants ( $N_c$ , mol m<sup>-2</sup> s<sup>-1</sup>) was calculated. Poisson's equation was used to solve the electric current density distribution on the surface and other electric parameters around the surface. The Navier-Stokes equations and Nernst-Planck equations were combined to describe the advection and diffusion of pollutants. The inlet was on the upper surface of the 3D simulation domain, and the reference electrode was placed on the lower surface. The interlayer spacing of the multilayer model was set to 600 nm. The pore size in

the classical pore structure model (fig. S28C) was set as 500 nm. The mass flux ( $N_c$ ) and the mass transfer coefficient ( $k_c$ ) were calculated as

$$N_c = -D \left( \frac{\partial C}{\partial \vec{n}} \right)_{\text{surface}} + C \times \vec{v} \cdot \vec{n} \quad (7)$$

$$k_c = \frac{N_c}{C_{\text{bulk}} - C_{\text{surface}}} \quad (8)$$

where  $C$  ( $\text{mol} \cdot \text{m}^{-3}$ ) is the pollutant concentration,  $\vec{n}$  is the normal vector of the electrode surface,  $\vec{v}$  is the flow rate on the electrode surface ( $\text{m} \cdot \text{s}^{-1}$ ),  $D$  ( $\text{m}^2 \cdot \text{s}^{-1}$ ) is the diffusion coefficient of the pollutant, and  $C_{\text{bulk}}$  and  $C_{\text{surface}}$  indicate the pollutant concentration of the bulk solution and at the electrode surface, respectively.

## Supplementary Materials

This PDF file includes:

Supplementary Sections S1 to S10

Figs. S1 to S32

Tables S1 to S3

References

## REFERENCE AND NOTES

- R. Zeng, Y. Yang, X. Feng, H. Li, L. M. Gibbs, F. J. DiSalvo, H. D. Abruña, Nonprecious transition metal nitrides as efficient oxygen reduction electrocatalysts for alkaline fuel cells. *Sci. Adv.* **8**, eabj1584 (2022).
- A. Abdelhafiz, A. N. M. Tanvir, M. Zeng, B. Wang, Z. Ren, A. R. Harutyunyan, Y. Zhang, J. Li, Pulsed light synthesis of high entropy nanocatalysts with enhanced catalytic activity and prolonged stability for oxygen evolution reaction. *Adv. Sci.* **10**, 2300426 (2023).
- Z. Liang, L. Song, M. Sun, B. Huang, Y. Du, Tunable CO/H<sub>2</sub> ratios of electrochemical reduction of CO<sub>2</sub> through the Zn-Ln dual atomic catalysts. *Sci. Adv.* **7**, eabl4915 (2021).
- Y. Gao, S. Liang, B. Liu, C. Jiang, C. Xu, X. Zhang, P. Liang, M. Elimelech, X. Huang, Subtle tuning of nanodefects actuates highly efficient electrocatalytic oxidation. *Nat. Commun.* **14**, 2059 (2023).
- L. Chen, A. N. Alshwabkeh, S. Hojabri, M. Sun, G. Xu, J. Li, A robust flow-through platform for organic contaminant removal. *Cell Rep. Phys. Sci.* **2**, 100296 (2021).
- L. Liu, H. Lan, Y. Cui, Q. Tang, J. Bai, X. An, M. Sun, H. Liu, J. Qu, A Janus membrane with electro-induced multi-affinity interfaces for high-efficiency water purification. *Sci. Adv.* **10**, eadn8696 (2024).
- L. Ren, J. Ma, M. Chen, Y. Qiao, R. Dai, X. Li, Z. Wang, Recent advances in electrocatalytic membrane for the removal of micropollutants from water and wastewater. *iScience* **25**, 104342 (2022).
- W. Bian, W. Wu, B. Wang, W. Tang, M. Zhou, C. Jin, H. Ding, W. Fan, Y. Dong, J. Li, D. Ding, Revitalizing interface in protonic ceramic cells by acid etch. *Nature* **604**, 479–485 (2022).
- S. Li, Q. Li, R. W. Carpick, P. Gumbsch, X. Z. Liu, X. Ding, J. Sun, J. Li, The evolving quality of frictional contact with graphene. *Nature* **539**, 541–545 (2016).
- L. Jin, X. Duan, M. Sun, C. D. Vecitis, H. Yu, Y. Liu, A General strategy to synthesize fluidic single atom electrodes for selective reactive oxygen species production. *ACS Nano* **17**, 12875–12883 (2023).
- Y. Yao, L. Zhao, J. Dai, J. Wang, C. Fang, G. Zhan, Q. Zheng, W. Hou, L. Zhang, Single atom Ru monolithic electrode for efficient chlorine evolution and nitrate reduction. *Angew. Chem. Int. Ed. Engl.* **61**, e202208215 (2022).
- J. Ding, J. Huang, Q. Zhang, Z. Wei, Q. He, Z. Chen, Y. Liu, X. Su, Y. Zhai, A hierarchical monolithic cobalt-single-atom electrode for efficient hydrogen peroxide production in acid. *Cat. Sci. Technol.* **12**, 2416–2419 (2022).
- E. Plaza-Mayoral, I. J. Pereira, K. Nicole Dalby, K. D. Jensen, I. Chorkendorff, H. Falsig, P. Sebastián-Pascual, M. Escudero-Escribano, Pd–Au nanostructured electrocatalysts with tunable compositions for formic acid oxidation. *ACS Appl. Energy Mater.* **5**, 10632–10644 (2022).
- H. Xie, H. Zhang, X. Wang, G. Wei, S. Chen, X. Quan, Conductive and stable polyphenylene/CNT composite membrane for electrically enhanced membrane fouling mitigation. *Front. Environ. Sci. Eng.* **18**, 3 (2023).
- C. C. Raj, R. Sundheep, R. Prasanth, Enhancement of electrochemical capacitance by tailoring the geometry of TiO<sub>2</sub> nanotube electrodes. *Electrochim. Acta* **176**, 1214–1220 (2015).
- H. L. Hellstern, M. Bremholm, A. Mamakhel, J. Becker, B. B. Iversen, Hydrothermal synthesis of TiO<sub>2</sub>@SnO<sub>2</sub> hybrid nanoparticles in a continuous-flow dual-stage reactor. *ChemSusChem* **9**, 532–539 (2016).
- Y. Lu, H. Cao, S. Xu, C. Jia, G. Zheng, A comparative study of the effects of different TiO<sub>2</sub> supports toward CO<sub>2</sub> electrochemical reduction on CuO/TiO<sub>2</sub> electrode. *RSC Adv.* **11**, 21805–21812 (2021).
- P. Li, X. Qi, L. Zhao, J. Wang, M. Wang, M. Shao, J. S. Chen, R. Wu, Z. Wei, Hierarchical 3D porous carbon with facily accessible Fe–N<sub>4</sub> single-atom sites for Zn–air batteries. *J. Mater. Chem. A* **10**, 5925–5929 (2022).
- M. Wang, B.-j. Kim, D. Suk Han, H. Park, Electrocatalytic activity of nanoparticulate TiO<sub>2</sub> coated onto Ta-doped IrO<sub>2</sub>/Ti substrates: Effects of the TiO<sub>2</sub> overlayer thickness. *Chem. Eng. J.* **425**, 131435 (2021).
- W. Fan, B. Wang, R. Gao, G. Dimitrakopoulos, J. Wang, X. Xiao, L. Ma, K. Wu, B. Yildiz, J. Li, Anodic shock-triggered exsolution of metal nanoparticles from perovskite oxide. *J. Am. Chem. Soc.* **144**, 7657–7666 (2022).
- J. Li, M. Li, N. An, S. Zhang, Q. Song, Y. Yang, J. Li, X. Liu, Boosted ammonium production by single cobalt atom catalysts with high Faradic efficiencies. *Proc. Natl. Acad. Sci. U.S.A.* **119**, e2123450119 (2022).
- Y.-C. Zhang, C. Han, J. Gao, J. Wu, X.-D. Zhu, J.-J. Zou, Co<sub>3-x</sub>O<sub>4</sub>/NiO with abundant Ni<sup>3+</sup> active sites for boosting oxygen evolution reaction. *Chem. Eng. J.* **446**, 137036 (2022).
- N. Shakibi Nia, C. Griesser, T. Mairegger, E.-M. Wernig, J. Bernardi, E. Portenkirchner, S. Penner, J. Kunze-Liebhäuser, Titanium oxycarbide as platinum-free electrocatalyst for ethanol oxidation. *ACS Catal.* **14**, 324–329 (2024).
- Y. Gao, N. Yan, C. Jiang, C. Xu, S. Yu, P. Liang, X. Zhang, S. Liang, X. Huang, Filtration-enhanced highly efficient photocatalytic degradation with a novel electrospun rGO@TiO<sub>2</sub> nanofibrous membrane: Implication for improving photocatalytic efficiency. *Appl. Catal. B* **268**, 118737 (2020).
- X. Li, W. Chen, Q. Qian, H. Huang, Y. Chen, Z. Wang, Q. Chen, J. Yang, J. Li, Y.-W. Mai, Electrospinning-based strategies for battery materials. *Adv. Energy Mater.* **11**, 2000845 (2021).
- J. Wen, G. L. Wilkes, Organic/inorganic hybrid network materials by the Sol–Gel approach. *Chem. Mater.* **8**, 1667–1681 (1996).
- J. Cheng, H. Ma, Y. Shi, L. Liu, W. Shang, W. Liu, S. Li, W. Li, Y. Wang, Y. Shi, Single-atom Ti decorated carbon black and carbon nanotubes: Modular dual-carbon electrode for optimizing the charge transport kinetics of perovskite solar cells. *Adv. Funct. Mater.* **34**, 2409533 (2024).
- L. Kuai, Z. Chen, S. Liu, E. Kan, N. Yu, Y. Ren, C. Fang, X. Li, Y. Li, B. Geng, Titania supported synergistic palladium single atoms and nanoparticles for room temperature ketone and aldehydes hydrogenation. *Nat. Commun.* **11**, 48 (2020).
- D. N. Miller, A. K. Azad, H. Delpouve, L. Quazuguel, J. Zhou, A. Sinha, P. Wormald, J. T. S. Irvine, Studies on the crystal structure, magnetic and conductivity properties of titanium oxycarbide solid solution (TiO<sub>1-x</sub>C<sub>x</sub>). *J. Mater. Chem. A* **4**, 5730–5736 (2016).
- R. Tröger, H. Ren, D. Yin, C. Postigo, P. D. Nguyen, C. Baduel, O. Golovko, F. Been, H. Joerss, M. R. Bolea, S. Polesello, M. Roncoroni, S. Taniyasu, F. Menger, L. Ahrens, F. Yin Lai, K. Wilberg, What's in the water?—Target and suspect screening of contaminants of emerging concern in raw water and drinking water from Europe and Asia. *Water Res.* **198**, 117099 (2021).
- S. S. Jeon, P. W. Kang, M. Klingenhof, H. Lee, F. Dionigi, P. Strasser, Active surface area and intrinsic catalytic oxygen evolution reactivity of NiFe LDH at reactive electrode potentials using capacitances. *ACS Catal.* **13**, 1186–1196 (2023).
- S. Franz, H. Arab, G. L. Chiarello, M. Bestetti, E. Selli, Single-step preparation of large area TiO<sub>2</sub> photoelectrodes for water splitting. *Adv. Energy Mater.* **10**, 2000652 (2020).
- K. Shi, Z. S. Parsons, X. Feng, Sensitivity of gas-evolving electrocatalysis to the catalyst microenvironment. *ACS Energy Lett.* **8**, 2919–2926 (2023).
- J. Shen, G. Liu, Y. Han, W. Jin, Artificial channels for confined mass transport at the sub-nanometre scale. *Nat. Rev. Mater.* **6**, 294–312 (2021).
- C. Liu, A.-Y. Zhang, Y. Si, D.-N. Pei, H.-Q. Yu, Photochemical protection of reactive sites on defective TiO<sub>2-x</sub> surface for electrochemical water treatment. *Environ. Sci. Technol.* **53**, 7641–7652 (2019).
- A.-Y. Zhang, T. Lin, Y.-Y. He, Y.-X. Mou, Heterogeneous activation of H<sub>2</sub>O<sub>2</sub> by defect-engineered TiO<sub>2-x</sub> single crystals for refractory pollutants degradation: A Fenton-like mechanism. *J. Hazard. Mater.* **311**, 81–90 (2016).
- M. Bai, B. Hong, K. Zhang, K. Yuan, K. Xie, W. Wei, Y. Lai, Defect-rich carbon nitride as electrolyte additive for in-situ electrode interface modification in lithium metal battery. *Chem. Eng. J.* **407**, 127123 (2021).
- J. P. Flach, P. H. Figueiredo de Lima, J. C. Sparks, M. Islam, R. Martinez-Duarte, Synthesis of titanium oxycarbide through carbothermal reduction of titanium dioxide nanoparticles and renewable biopolymers. *ECS Trans.* **72**, 17–23 (2016).
- Ministry of Ecology and Environment of the People's Republic of China. *Discharge standard of pollutants for urban wastewater treatment plant* (Ministry of Ecology and Environment of the People's Republic of China, 2022).
- U. S. E. P. Agency, in *National Primary Drinking Water Regulations* (2024).
- G. Chen, Z. Ma, K. Xiao, X. Wang, S. Liang, X. Huang, Hierarchically textured superhydrophilic polyvinylidene fluoride membrane via nanocasting and post-

- fabrication grafting of surface-tailored silica nanoparticles. *Environ. Sci. Nano* **6**, 3579–3589 (2019).
42. H. Shi, Y. Wang, C. Li, R. Pierce, S. Gao, Q. Huang, Degradation of perfluorooctanesulfonate by reactive electrochemical membrane composed of magnéli phase titanium suboxide. *Environ. Sci. Technol.* **53**, 14528–14537 (2019).
  43. M. Li, K. Zuo, S. Liang, K. Xiao, P. Liang, X. Wang, X. Huang, Electrically tuning ultrafiltration behavior for efficient water purification. *Environ. Sci. Technol.* **54**, 11536–11545 (2020).
  44. Y. Wang, X. Liu, X. Han, R. Godin, J. Chen, W. Zhou, C. Jiang, J. F. Thompson, K. B. Mustafa, S. A. Shevlin, J. R. Durrant, Z. Guo, J. Tang, Unique hole-accepting carbon-dots promoting selective carbon dioxide reduction nearly 100% to methanol by pure water. *Nat. Commun.* **11**, 2531 (2020).
  45. C. Liu, Y. Min, A.-Y. Zhang, Y. Si, J.-J. Chen, H.-Q. Yu, Electrochemical treatment of phenol-containing wastewater by facet-tailored TiO<sub>2</sub>: Efficiency, characteristics and mechanisms. *Water Res.* **165**, 114980 (2019).
  46. X. Wang, D. Guo, J. Zhang, Y. Yao, Y. Liu, Insights into the electron transfer mechanisms of permanganate activation by carbon nanotube membrane for enhanced micropollutants degradation. *Front. Environ. Sci. Eng.* **17**, 106 (2023).
  47. Z. Pan, C. Song, L. Li, H. Wang, Y. Pan, C. Wang, J. Li, T. Wang, X. Feng, Membrane technology coupled with electrochemical advanced oxidation processes for organic wastewater treatment: Recent advances and future prospects. *Chem. Eng. J.* **376**, 120909 (2019).
  48. S. Lan, J. Feng, Y. Xiong, S. Tian, S. Liu, L. Kong, Performance and mechanism of piezo-catalytic degradation of 4-chlorophenol: Finding of effective piezo-dechlorination. *Environ. Sci. Technol.* **51**, 6560–6569 (2017).
  49. L. Peng, H. Liu, W.-L. Wang, Z.-B. Xu, X.-Y. Ni, Y.-H. Wu, Q.-Y. Wu, H.-Y. Hu, Degradation of methylisothiazolinone biocide using a carbon fiber felt-based flow-through electrode system (FES) via anodic oxidation. *Chem. Eng. J.* **384**, 123239 (2020).
  50. Y. Zhao, M. Sun, X. Wang, C. Wang, D. Lu, W. Ma, S. A. Kube, J. Ma, M. Elimelech, Janus electrocatalytic flow-through membrane enables highly selective singlet oxygen production. *Nat. Commun.* **11**, 6228 (2020).
  51. J. Wandt, P. Jakes, J. Granwehr, H. A. Gasteiger, R.-A. Eichel, Singlet oxygen formation during the charging process of an aprotic lithium–oxygen battery. *Angew. Chem. Int. Ed. Engl.* **55**, 6892–6895 (2016).
  52. W. Huang, X. Wang, W. Zhang, S. Zhang, Y. Tian, Z. Chen, W. Fang, J. Ma, Intraligand charge transfer boosts visible-light-driven generation of singlet oxygen by metal-organic frameworks. *Appl. Catal. B* **273**, 119087 (2020).
  53. Y. Qian, D. Li, Y. Han, H.-L. Jiang, Photocatalytic molecular oxygen activation by regulating excitonic effects in covalent organic frameworks. *J. Am. Chem. Soc.* **142**, 20763–20771 (2020).
  54. C. Dong, Y. Bao, T. Sheng, Q. Yi, Q. Zhu, B. Shen, M. Xing, I. M. C. Lo, J. Zhang, Singlet oxygen triggered by robust bimetallic MoFe/TiO<sub>2</sub> nanospheres of highly efficacy in solar-light-driven peroxymonosulfate activation for organic pollutants removal. *Appl. Catal. B* **286**, 119930 (2021).
  55. C. Trellu, M. Rivallin, S. Cerneau, C. Coetsier, C. Causserand, M. A. Oturan, M. Cretin, Integration of sub-stoichiometric titanium oxide reactive electrochemical membrane as anode in the electro-Fenton process. *Chem. Eng. J.* **400**, 125936 (2020).
  56. H. Tu, M. Huang, Y. Yi, Z. Li, Y. Zhan, J. Chen, Y. Wu, X. Shi, H. Deng, Y. Du, Chitosan-rectorite nanospheres immobilized on polystyrene fibrous mats via alternate electrospinning/ electrospraying techniques for copper ions adsorption. *Appl. Surf. Sci.* **426**, 545–553 (2017).
  57. A. Abdelhafiz, B. Wang, A. R. Harutyunyan, J. Li, Carbothermal shock synthesis of high entropy oxide catalysts: Dynamic structural and chemical reconstruction boosting the catalytic activity and stability toward oxygen evolution reaction. *Adv. Energy Mater.* **12**, 2200742 (2022).
  58. X. Li, S. Shao, Y. Yang, Y. Mei, W. Qing, H. Guo, L. E. Peng, P. Wang, C. Y. Tang, Engineering interface with a one-dimensional RuO<sub>2</sub>/TiO<sub>2</sub> heterostructure in an electrocatalytic membrane electrode: Toward highly efficient micropollutant decomposition. *ACS Appl. Mater. Interfaces* **12**, 21596–21604 (2020).
  59. S. Liang, W. Zheng, L. Zhu, W. Duan, C. Wei, C. Feng, One-step treatment of phosphite-laden wastewater: A single electrochemical reactor integrating superoxide radical-induced oxidation and electrocoagulation. *Environ. Sci. Technol.* **53**, 5328–5336 (2019).
  60. B. Ravel, M. Newville, ATHENA, ARTEMIS, HEPHAESTUS: Data analysis for x-ray absorption spectroscopy using IFEFFIT. *J. Synchrotron Radiat.* **12**, 537–541 (2005).
  61. C. Trellu, C. Coetsier, J.-C. Rouch, R. Esmilaire, M. Rivallin, M. Cretin, C. Causserand, Mineralization of organic pollutants by anodic oxidation using reactive electrochemical membrane synthesized from carbothermal reduction of TiO<sub>2</sub>. *Water Res.* **131**, 310–319 (2018).
  62. V. Maneeratana, D. Portehault, J. Chaste, D. Maily, M. Antonietti, C. Sanchez, Original electrospun core–shell nanostructured magnéli titanium oxide fibers and their electrical properties. *Adv. Mater.* **26**, 2654–2658 (2014).
  63. A. Wang, X. Liu, Y. Wen, Y. Qiu, S. Lv, M. Xu, C. Meng, K. Wang, F. Lin, S. Xie, Q. Zhuo, Single-atom Zr embedded Ti<sub>4</sub>O<sub>7</sub> anode coupling with hierarchical CuFe<sub>2</sub>O<sub>4</sub> particle electrodes toward efficient electrooxidation of actual pharmaceutical wastewater. *Water Res.* **245**, 120596 (2023).
  64. D. Huang, D. J. Kim, K. Rigby, X. Zhou, X. Wu, A. Meese, J. Niu, E. Stavitski, J.-H. Kim, Elucidating the Role of single-atom Pd for electrocatalytic hydrodechlorination. *Environ. Sci. Technol.* **55**, 13306–13316 (2021).
  65. T. Li, S. Ren, C. Zhang, L. Qiao, J. Wu, P. He, J. Lin, Y. Liu, Z. Fu, Q. Zhu, W. Pan, B. Wang, Z. Chen, Cobalt single atom anchored on N-doped carbon nanoboxes as typical single-atom catalysts (SACs) for boosting the overall water splitting. *Chem. Eng. J.* **458**, 141435 (2023).
  66. Y. Liao, C.-H. Loh, M. Tian, R. Wang, A. G. Fane, Progress in electrospun polymeric nanofibrous membranes for water treatment: Fabrication, modification and applications. *Prog. Polym. Sci.* **77**, 69–94 (2018).
  67. C. J. Luo, S. D. Stoyanov, E. Stride, E. Pelan, M. Edirisinghe, Electrospinning versus fibre production methods: From specifics to technological convergence. *Chem. Soc. Rev.* **41**, 4708–4735 (2012).
  68. L. Persano, A. Camposo, C. Tekmen, D. Pisignano, Industrial upscaling of electrospinning and applications of polymer nanofibers: A review. *Macromol. Mater. Eng.* **298**, 504–520 (2013).
  69. M. Yu, R.-H. Dong, X. Yan, G.-F. Yu, M.-H. You, X. Ning, Y.-Z. Long, Recent advances in needleless electrospinning of ultrathin fibers: From academia to industrial production. *Macromol. Mater. Eng.* **302**, 1700002 (2017).
  70. H. B. Madalosso, R. Machado, D. Hotza, C. Marangoni, Membrane surface modification by electrospinning, coating, and plasma for membrane distillation applications: A state-of-the-art review. *Adv. Eng. Mater.* **23**, 2001456 (2021).
  71. J. Xue, T. Wu, Y. Dai, Y. Xia, Electrospinning and electrospun nanofibers: Methods, materials, and applications. *Chem. Rev.* **119**, 5298–5415 (2019).
  72. H. Lin, H. Peng, X. Feng, X. Li, J. Zhao, K. Yang, J. Liao, D. Cheng, X. Liu, S. Lv, J. Xu, Q. Huang, Energy-efficient for advanced oxidation of bio-treated landfill leachate effluent by reactive electrochemical membranes (REMs): Laboratory and pilot scale studies. *Water Res.* **190**, 116790 (2021).
  73. T. X. Huong Le, L. F. Dumée, S. Lacour, M. Rivallin, Z. Yi, L. Kong, M. Bechelany, M. Cretin, Hybrid graphene-decorated metal hollow fibre membrane reactors for efficient electro-Fenton - Filtration co-processes. *J. Membr. Sci.* **587**, 117182 (2019).
  74. N. Mamedia, H. J. Park, K. H. Choo, Membrane electro-oxidizer: A new hybrid membrane system with electrochemical oxidation for enhanced organics and fouling control. *Water Res.* **126**, 40–49 (2017).
  75. H. Hui, H. Wang, Y. Mo, Z. Yin, J. Li, Optimal design and evaluation of electrocatalytic reactors with nano-MnOx/Ti membrane electrode for wastewater treatment. *Chem. Eng. J.* **376**, 120190 (2019).
  76. K. V. Plakas, S. D. Sklari, D. A. Yiankakis, G. T. Sideropoulos, V. T. Zaspalis, A. J. Karabelas, Removal of organic micropollutants from drinking water by a novel electro-Fenton filter: Pilot-scale studies. *Water Res.* **91**, 183–194 (2016).
  77. D. Yu, M. Wu, Q. Hu, L. Wang, C. Lv, L. Zhang, Iron-based metal-organic frameworks as novel platforms for catalytic ozonation of organic pollutant: Efficiency and mechanism. *J. Hazard. Mater.* **367**, 456–464 (2019).
  78. J. Lim, Y. Yang, M. R. Hoffmann, Activation of peroxymonosulfate by oxygen vacancies-enriched cobalt-doped black TiO<sub>2</sub> nanotubes for the removal of organic pollutants. *Environ. Sci. Technol.* **53**, 6972–6980 (2019).
  79. C. C. L. McCrory, S. Jung, I. M. Ferrer, S. M. Chatman, J. C. Peters, T. F. Jaramillo, Benchmarking hydrogen evolving reaction and oxygen evolving reaction electrocatalysts for solar water splitting devices. *J. Am. Chem. Soc.* **137**, 4347–4357 (2015).
  80. M. Szkoda, A. Ilnicka, M. Skorupska, M. Wysokowski, J. P. Lukaszewicz, Modification of TiO<sub>2</sub> nanotubes by graphene–strontium and cobalt molybdate perovskite for efficient hydrogen evolution reaction in acidic medium. *Sci. Rep.* **12**, 22577 (2022).
  81. A. M. Diez, I. Núñez, M. Pazos, M. Á. Sanromán, Y. V. Kolen'ko, Fluoride-doped TiO<sub>2</sub> photocatalyst with enhanced activity for stable pollutant degradation. *Catalysts* **12**, 1190 (2022).
  82. J. Li, Y. Kuang, X. Zhang, W.-H. Hung, C.-Y. Chiang, G. Zhu, G. Chen, F. Wang, P. Liang, H. Dai, Electrochemical acetate production from high-pressure gaseous and liquid CO<sub>2</sub>. *Nat. Catal.* **6**, 1151–1163 (2023).
  83. Y. Zhao, Y. Wang, Y. Dong, C. Carlos, J. Li, Z. Zhang, T. Li, Y. Shao, S. Yan, L. Gu, J. Wang, X. Wang, Quasi-two-dimensional earth-abundant bimetallic electrocatalysts for oxygen evolution reactions. *ACS Energy Lett.* **6**, 3367–3375 (2021).
  84. Y. Yan, J. Lin, K. Huang, X. Zheng, L. Qiao, S. Liu, J. Cao, S. C. Jun, Y. Yamauchi, J. Qi, Tensile strain-mediated spinel ferrites enable superior oxygen evolution activity. *J. Am. Chem. Soc.* **145**, 24218–24229 (2023).
  85. Y. Wei, Y. Hu, P. Da, Z. Weng, P. Xi, C.-H. Yan, Triggered lattice-oxygen oxidation with active-site generation and self-termination of surface reconstruction during water oxidation. *Proc. Natl. Acad. Sci. U.S.A.* **120**, e2312224120 (2023).
  86. F. Ye, S. Zhang, Q. Cheng, Y. Long, D. Liu, R. Paul, Y. Fang, Y. Su, L. Qu, L. Dai, C. Hu, The role of oxygen-vacancy in bifunctional indium oxyhydroxide catalysts for electrochemical coupling of biomass valorization with CO<sub>2</sub> conversion. *Nat. Commun.* **14**, 2040 (2023).

87. F. Yao, M. Jia, Q. Yang, F. Chen, Y. Zhong, S. Chen, L. He, Z. Pi, K. Hou, D. Wang, X. Li, Highly selective electrochemical nitrate reduction using copper phosphide self-supported copper foam electrode: Performance, mechanism, and application. *Water Res.* **193**, 116881 (2021).
88. S. I. Perez Bakovic, P. Acharya, M. Watkins, H. Thornton, S. Hou, L. F. Greenlee, Electrochemically active surface area controls HER activity for Fe<sub>x</sub>Ni<sub>100-x</sub> films in alkaline electrolyte. *J. Catal.* **394**, 104–112 (2021).
89. J. D. García-Espinoza, M. Zolfaghari, P. Mijajlova Nacheva, Synergistic effect between ultraviolet irradiation and electrochemical oxidation for removal of humic acids and pharmaceuticals. *Water Environ. J.* **34**, 232–246 (2020).
90. H. Song, L. Yan, J. Ma, J. Jiang, G. Cai, W. Zhang, Z. Zhang, J. Zhang, T. Yang, Nonradical oxidation from electrochemical activation of peroxydisulfate at Ti/Pt anode: Efficiency, mechanism and influencing factors. *Water Res.* **116**, 182–193 (2017).
91. J. T. Jasper, O. S. Shafaat, M. R. Hoffmann, Electrochemical transformation of trace organic contaminants in latrine wastewater. *Environ. Sci. Technol.* **50**, 10198–10208 (2016).
92. E. Isarain-Chávez, R. M. Rodríguez, P. L. Cabot, F. Centellas, C. Arias, J. A. Garrido, E. Brillas, Degradation of pharmaceutical beta-blockers by electrochemical advanced oxidation processes using a flow plant with a solar compound parabolic collector. *Water Res.* **45**, 4119–4130 (2011).
93. J. Zheng, Z. Wang, J. Ma, S. Xu, Z. Wu, Development of an electrochemical ceramic membrane filtration system for efficient contaminant removal from waters. *Environ. Sci. Technol.* **52**, 4117–4126 (2018).
94. L. Xu, J. Niu, H. Xie, X. Ma, Y. Zhu, J. Crittenden, Effective degradation of aqueous carbamazepine on a novel blue-colored TiO<sub>2</sub> nanotube arrays membrane filter anode. *J. Hazard. Mater.* **402**, 123530 (2021).
95. F. Wei, D. Liao, Y. Lin, C. Hu, J. Ju, Y. Chen, D. Feng, Electrochemical degradation of reverse osmosis concentrate (ROC) using the electrodeposited Ti/TiO<sub>2</sub>-NTs/PbO<sub>2</sub> electrode. *Sep. Purif. Technol.* **258**, 118056 (2021).
96. K. Wang, Y. Li, J. Huang, L. Xu, L. Yin, Y. Ji, C. Wang, Z. Xu, J. Niu, Insights into electrochemical decomposition mechanism of lipopolysaccharide using TiO<sub>2</sub> nanotubes arrays electrode. *J. Hazard. Mater.* **391**, 122259 (2020).
97. L. Huang, D. Li, J. Liu, L. Yang, C. Dai, N. Ren, Y. Feng, Construction of TiO<sub>2</sub> nanotube clusters on Ti mesh for immobilizing Sb-SnO<sub>2</sub> to boost electrocatalytic phenol degradation. *J. Hazard. Mater.* **393**, 122329 (2020).
98. M. Chen, S. Pan, C. Zhang, C. Wang, W. Zhang, Z. Chen, X. Zhao, Y. Zhao, Electrochemical oxidation of reverse osmosis concentrates using enhanced TiO<sub>2</sub>-NTA/SnO<sub>2</sub>-Sb anodes with/without PbO<sub>2</sub> layer. *Chem. Eng. J.* **399**, 125756 (2020).
99. M. Chen, C. Wang, X. Zhao, Y. Wang, W. Zhang, Z. Chen, X. Meng, J. Luo, J. Crittenden, Development of a highly efficient electrochemical flow-through anode based on inner in-site enhanced TiO<sub>2</sub>-nanotubes array. *Environ. Int.* **140**, 105813 (2020).
100. X. Meng, Z. Chen, C. Wang, W. Zhang, K. Zhang, S. Zhou, J. Luo, N. Liu, D. Zhou, D. Li, J. Crittenden, Development of a three-dimensional electrochemical system using a blue TiO<sub>2</sub>/SnO<sub>2</sub>-Sb<sub>2</sub>O<sub>3</sub> anode for treating low-ionic-strength wastewater. *Environ. Sci. Technol.* **53**, 13784–13793 (2019).
101. J. Cai, M. Zhou, Y. Pan, X. Du, X. Lu, Extremely efficient electrochemical degradation of organic pollutants with co-generation of hydroxyl and sulfate radicals on Blue-TiO<sub>2</sub> nanotubes anode. *Appl Catal B* **257**, 117902 (2019).
102. Y. Yang, L. C. Kao, Y. Liu, K. Sun, H. Yu, J. Guo, S. Y. H. Liou, M. R. Hoffmann, Cobalt-doped black TiO<sub>2</sub> nanotube array as a stable anode for oxygen evolution and electrochemical wastewater treatment. *ACS Catal.* **8**, 4278–4287 (2018).
103. Y. Yang, M. R. Hoffmann, Synthesis and stabilization of blue-black TiO<sub>2</sub> nanotube arrays for electrochemical oxidant generation and wastewater treatment. *Environ. Sci. Technol.* **50**, 11888–11894 (2016).
104. M. T. Fukunaga, J. R. Guimarães, R. Bertazzoli, Kinetics of the oxidation of formaldehyde in a flow electrochemical reactor with TiO<sub>2</sub>/RuO<sub>2</sub> anode. *Chem. Eng. J.* **136**, 236–241 (2008).
105. S. N. Misal, M.-H. Lin, S. Mehraeen, B. P. Chaplin, Modeling electrochemical oxidation and reduction of sulfamethoxazole using electrocatalytic reactive electrochemical membranes. *J. Hazard. Mater.* **384**, 121420 (2020).
106. Y. Liu, H. Liu, Z. Zhou, T. Wang, C. N. Ong, C. D. Vecitis, Degradation of the common aqueous antibiotic tetracycline using a carbon nanotube electrochemical filter. *Environ. Sci. Technol.* **49**, 7974–7980 (2015).
107. T.-Y. Tan, Z.-T. Zeng, G.-M. Zeng, J.-L. Gong, R. Xiao, P. Zhang, B. Song, W.-W. Tang, X.-Y. Ren, Electrochemically enhanced simultaneous degradation of sulfamethoxazole, ciprofloxacin and amoxicillin from aqueous solution by multi-walled carbon nanotube filter. *Sep. Purif. Technol.* **235**, 116167 (2020).
108. J. F. Carneiro, J. M. Aquino, B. F. Silva, A. J. Silva, R. C. Rocha-Filho, Comparing the electrochemical degradation of the fluoroquinolone antibiotics norfloxacin and ciprofloxacin using distinct electrolytes and a BDD anode: Evolution of main oxidation byproducts and toxicity. *J. Environ. Chem. Eng.* **8**, 104433 (2020).
109. D. A. C. Coledam, J. M. Aquino, B. F. Silva, A. J. Silva, R. C. Rocha-Filho, Electrochemical mineralization of norfloxacin using distinct boron-doped diamond anodes in a filter-press reactor, with investigations of toxicity and oxidation by-products. *Electrochim. Acta* **213**, 856–864 (2016).
110. M.-L. Liu, L. Li, Y.-X. Sun, Z.-J. Fu, X.-L. Cao, S.-P. Sun, Scalable conductive polymer membranes for ultrafast organic pollutants removal. *J. Membr. Sci.* **617**, 118644 (2021).
111. P. Gayen, C. Chen, J. T. Abiade, B. P. Chaplin, Electrochemical oxidation of atrazine and clothianidin on Bi-doped SnO<sub>2</sub>-TiO<sub>2</sub>-n<sub>1</sub> electrocatalytic reactive electrochemical membranes. *Environ. Sci. Technol.* **52**, 12675–12684 (2018).
112. L. Xu, X. Ma, J. Niu, J. Chen, C. Zhou, Removal of trace naproxen from aqueous solution using a laboratory-scale reactive flow-through membrane electrode. *J. Hazard. Mater.* **379**, 120692 (2019).
113. C. Zhou, Y. Wang, J. Chen, J. Niu, Porous Ti/SnO<sub>2</sub>-Sb anode as reactive electrochemical membrane for removing trace antiretroviral drug stavudine from wastewater. *Environ. Int.* **133**, 105157 (2019).
114. S. Yu, Y. Gao, R. Khan, P. Liang, X. Zhang, X. Huang, Electrospun PAN-based graphene/SnO<sub>2</sub> carbon nanofibers as anodic electrocatalysis microfiltration membrane for sulfamethoxazole degradation. *J. Membr. Sci.* **614**, 118368 (2020).
115. C. Yang, Y. Fan, S. Shang, P. Li, X. Y. Li, Fabrication of a permeable SnO<sub>2</sub>-Sb reactive anodic filter for high-efficiency electrochemical oxidation of antibiotics in wastewater. *Environ. Int.* **157**, 106827 (2021).
116. I. Sánchez-Montes, J. R. Fuzer Neto, B. F. Silva, A. J. Silva, J. M. Aquino, R. C. Rocha-Filho, Evolution of the antibacterial activity and oxidation intermediates during the electrochemical degradation of norfloxacin in a flow cell with a PTFE-doped β-PbO<sub>2</sub> anode: Critical comparison to a BDD anode. *Electrochim. Acta* **284**, 260–270 (2018).
117. G. Wei, X. Quan, X. Fan, S. Chen, Y. Zhang, Carbon-nanotube-based sandwich-like hollow fiber membranes for expanded microcystin-LR removal applications. *Chem. Eng. J.* **319**, 212–218 (2017).
118. Y. Yang, S. Qiao, M. Zheng, J. Zhou, X. Quan, Enhanced permeability, contaminants removal and antifouling ability of CNTs-based hollow fiber membranes under electrochemical assistance. *J. Membr. Sci.* **582**, 335–341 (2019).
119. D. Huang, G. Wang, X. Zhao, W. Pang, M. Wang, D. Wang, Electrogenation of hydrogen peroxide in neutral medium using PVDF-based air cathode for removing ofloxacin in wastewater. *J. Solid State Electrochem.* **23**, 1455–1462 (2019).
120. J. Chen, S. Fan, Y. Chen, Y. Wang, K. Bai, Z. Mai, Z. Xiao, Electrocatalytic composite membrane with deep-permeation nano structure fabricated by flowing synthesis for enhanced catalysis. *J. Membr. Sci.* **636**, 119616 (2021).
121. H. Liu, G. Zhang, C. Zhao, J. Liu, F. Yang, Hydraulic power and electric field combined antifouling effect of a novel conductive poly(aminoanthraquinone)/reduced graphene oxide nanohybrid blended PVDF ultrafiltration membrane. *J. Mater. Chem. A* **3**, 20277–20287 (2015).
122. A. V. Dudchenko, J. Rolf, K. Russell, W. Duan, D. Jassby, Organic fouling inhibition on electrically conducting carbon nanotube–polyvinyl alcohol composite ultrafiltration membranes. *J. Membr. Sci.* **468**, 1–10 (2014).
123. F. Sun, J. Yang, Q. Shen, M. Li, H. Du, D. Y. Xing, Conductive polyethersulfone membrane facilely prepared by simultaneous phase inversion method for enhanced anti-fouling and separation under low driven-pressure. *J. Environ. Manage.* **297**, 113363 (2021).

#### Acknowledgments

**Funding:** We gratefully acknowledge the financial support from the Major Program of National Natural Science Foundation of China (no. 52091543) and the National Natural Science Foundation of China (No. 52170022). **Author Contributions:** Y.G., S.L., J.L., and X.H. conceived the idea. Y.G. and S.L. designed the experiments. Y.G. implemented the experimental setup. Y.G., Q.Z., M.G., and Z.Z. conducted the experiments. Y.G. and C.J. carried out the theoretical calculations. Y.G. and A.A. obtained ECSA data through experiments. Y.Y. and Y.H. performed part of the TEM characterization. Y.G., S.L., J.L., and X.H. wrote the manuscript. P.L. and X.Z. participated in the experiments design and manuscript review. All the authors discussed the results and commented on the manuscript. **Competing interests:** The authors declare that they have no competing interests. **Data and materials availability:** All data needed to evaluate the conclusions in the paper are present in the paper and/or the Supplementary Materials.

Submitted 27 August 2024

Accepted 14 March 2025

Published 18 April 2025

10.1126/sciadv.ads7154

Supplementary Materials for  
**Electric field–confined synthesis of single atomic TiO<sub>x</sub>C<sub>y</sub>  
electrocatalytic membranes**

Yifan Gao *et al.*

Corresponding author: Shuai Liang, shuai\_liang@bjfu.edu.cn; Ju Li, liju@mit.edu;  
Xia Huang, xhuang@tsinghua.edu.cn

*Sci. Adv.* **11**, eads7154 (2025)  
DOI: 10.1126/sciadv.ads7154

**This PDF file includes:**

Supplementary Sections S1 to S10  
Figs. S1 to S32  
Tables S1 to S3  
References

## Supplementary Section I

**The X-ray absorption near-edge structure characterization.** The EXAFS fitting parameters at the Ti K-edge for various samples were listed in **Table S1**. The obtained XAFS data was processed in Athena (version 0.9.26)(60) for background, pre-edge line and post-edge line calibrations. Then Fourier transformed fitting was carried out in Artemis (version 0.9.26) (60). The  $k^2$  weighting,  $k$ -range of 3–12  $\text{\AA}^{-1}$  and  $R$  range of 1–3  $\text{\AA}$  were used for the fitting of Ti-foil; The  $k^2$  weighting,  $k$ -range of 3–10.0  $\text{\AA}^{-1}$  and  $R$  range of 1–3  $\text{\AA}$  were used for the fitting of Samples.

## Supplementary Section II

**Formation of  $\text{TiO}_x\text{C}_y$ ,  $\text{TiO}_{2-x}$ , and TiC.** Normally, the formation of  $\text{TiO}_x\text{C}_y$ ,  $\text{TiO}_{2-x}$ , or TiC in anatase titanium oxide requires harsh conditions. Most of the previous studies used high-temperature hydrogen reduction(35, 36). However, this method is dangerous and expensive, thus limiting the practical application of the  $\text{TiO}_x\text{C}_y$ . The formation of oxygen defects can also be achieved by carbothermal reduction(61, 62):



but the required temperature is relatively high(61). Herein, the  $\text{TiO}_x\text{C}_y$ ,  $\text{TiO}_{2-x}$ , and TiC were detected in the  $\text{TiO}_x\text{C}_y$  membrane, suggesting that the submicron structure of the electrospun nanofibers and nanoparticles might help to reduce the energy barrier of the reduction reaction(62). Under the action of high-voltage electrostatic field (1.5  $\text{kV cm}^{-1}$ ) during the electrospinning process, a high-energy collision occurred between the Ti-contained nano-liquid mist and polymer nanofibers. A high-energy collision would promote the tight contact of  $\text{TiO}_2$  and CN. The tight contact (submicron structure of the electrospun nanofibers and nanoparticles) help to reduce the energy barrier of the carbothermal reduction reaction (S1). So the *in-situ* generated anatase nanoparticles in  $\text{TiO}_x\text{C}_y$  membrane bore an easier tendency of carbothermal reduction reaction (S1).

Overall, the above analyses supported the formation of  $\text{TiO}_x\text{C}_y$ ,  $\text{TiO}_{2-x}$ , and  $\text{TiC}$  in the  $\text{TiO}_x\text{C}_y$  membrane.

### Supplementary Section III

**Filtration performance of  $\text{TiO}_x\text{C}_y$  membrane.** Owing to its highly porous structure, the  $\text{TiO}_x\text{C}_y$  membrane achieved a considerably high water permeability of  $8370 \pm 190 \text{ L m}^{-2} \text{ h}^{-1} \text{ bar}^{-1}$  (**Fig. S16A**). The effective pore size of the  $\text{TiO}_x\text{C}_y$  membrane was also evaluated with a series of micro-particle rejection tests. The results (**Fig. S16B**) showed that its effective pore size fell roughly around 350 nm with a good selectivity (sharp increase of rejection rate). Detailed particle rejection performance for the different micro-particles of 806.9, 362.2, 194.5, and 57.7 nm were showed in **Fig. S16C–F**, respectively.

### Supplementary Section IV

**Assessment of fabrication cost and prospect for practical scalability.** Here, we conducted a preliminary techno-economic outlook to compare the cost of the DESP with other methods for the preparation of catalytic electrodes. We considered the energy consumption and other associated costs of the DESP, thermal treatment, and other preparation processes reported in the literature, normalizing these costs to the unit mass of the catalyst produced (USD/g). Our findings indicate that the cost of producing the  $\text{TiO}_x\text{C}_y$  membrane is about \$7/g, whereas the costs for  $\text{Zr/Ti}_4\text{O}_7$  electrode(63),  $\text{Pd}_1/\text{rGO}$  electrode(64),  $\text{Pd}_{\text{nano}}/\text{rGO}$  electrode(64), and  $\text{Co@CNB-N}_4$  electrode(65) from various literature sources are \$500/g, \$396/g, \$446/g, and \$227/g, respectively. Consequently, beyond the low material cost of the  $\text{TiO}_x\text{C}_y$  membrane, the DESP process also presents a cost advantage in its preparation. Furthermore, since the  $\text{TiO}_x\text{C}_y$  membrane is binder-free throughout its preparation, it avoids the environmental impact associated with binders, resulting in substantial environmental benefits.

The electrospinning technology has been widely recognized as a low cost and promising technology(66) for preparation of nano-fiber based products. In our laboratory, large-area membranes (at least 300 mm in length, 100 mm in width, and 0.35 mm in thickness) have been successfully prepared (**Fig. 2H–2I**). For practical industrial productions, the large-scale applications have made a great progress in the past decades(66-71). Electrospinning can be operated in the same production line as electrospinning. The only difference is the composition of precursor solutions. It can be feasibly incorporated to the production line of electrospinning. Another injector and high electrostatic voltage for electrospinning can easily be added to the electrospinning production line. Correspondingly, the simultaneous electrospinning–electrospinning process required in the proposed fabrication strategy can be feasibly established. Besides, thermal treatment is a very common and general method in industrial productions. Overall, the fabrication methods of the  $\text{TiO}_x\text{C}_y$  membranes (i.e., electrospinning, electrospinning, and thermal treatment) are promisingly low-cost and easy to scale up. Additionally, in view of the advantageous performance in several previously reported scaled-up studies based on various electrocatalytic-membrane-based processes(72-76), we envision that the superior performance (**Fig. 1Q**) of the prepared electrocatalytic membrane can also be expected in future scaled-up applications.

### **Supplementary Section V**

**Comparison of the electrocatalytic performance of  $\text{TiO}_x\text{C}_y$  membrane.** Different designs of control experiments had been conducted for different purposes. **i)** To reveal the unique performance of the single atomic Ti and  $\text{TiO}_x\text{C}_y$  cluster, we designed the comparison between the CN membrane alone and the  $\text{TiO}_x\text{C}_y$  membrane. **ii)** To reveal the effects of the preparation process on ECSA, we designed the comparison between the  $\text{TiO}_2$ \_dip\_coating@CP (commonly used conventional method) and  $\text{TiO}_x\text{C}_y$  membranes. **iii)** To reveal the advantages of the proposed DESP strategy over the

conventional and commonly used blending or coating strategies, we designed the comparison between the  $\text{TiO}_x\text{C}_y$  membrane and the P25/CN (blending strategy) and VF-P25@CN membranes.

As shown in **Fig. 3A**, the  $\text{TiO}_x\text{C}_y$  membrane achieved a higher removal rate than the commercial  $\text{TiO}_2$  nanoparticles (P25)/CN and vacuum filtration (VF)-P25@CN. By these strategies, the  $\text{TiO}_2$  catalysts were mainly loosely deposited on the surface of the membrane. As a result, the binding between the catalysts and CN matrix would be very weak thus decreased electrocatalysis efficiency. Besides, it would be difficult to achieve a uniform catalyst distribution throughout the membrane matrix by this coating strategy. That would also limit their degradation efficiency. In addition to the control membranes above, we tried directly blending the TBT in the electrospinning side, i.e., adding TBT to the precursor solution of the CNs, a DMF solution containing PAN. However, due to the fast reaction between TBT and PAN, this precursor solution quickly produced a large amount of lumpy solids, which were not suitable for electrospinning. This phenomenon further demonstrates the advances of our DESP strategy.

## Supplementary Section VI

**Effect of dissolved oxygen (DO).** The DO concentration of the influent in the EMF process with the  $\text{TiO}_x\text{C}_y$  membrane was reduced to  $<2 \text{ mg L}^{-1}$  by bubbling nitrogen. It was noted that the DO concentration of the normal (i.e., without particular control of the DO condition) EMF test was relatively steady at  $\sim 8\text{--}9 \text{ mg L}^{-1}$ . The reduction of influent DO concentration led to a decrease of the PRO removal rate by 24% (**Fig. 3E**). This rate is similar to the contribution ratio of  $^1\text{O}_2$  oxidation to the PRO removal during the  $\text{TiO}_x\text{C}_y$  membrane-based EMF test. Under continuous stirring in the reservoir, the DO concentration of the influent gradually increased to  $\sim 5.5 \text{ mg L}^{-1}$ . The difference of PRO removal rate between the nitrogen bubbling group and the normal group was also reduced to 17%. This indicates that the removal of PRO is positively correlated with

the DO concentration. Accordingly, we speculated that the generated  $^1\text{O}_2$  comes from the transformation of the DO in the solution.

## Supplementary Section VII

**The detection of  $\cdot\text{OH}$ .** In general, the quenching tests revealed that the generation of both the  $\cdot\text{OH}$  and  $\text{O}_2^{\cdot-}$  was minor (**Fig. S26A**). When TBU, a quencher of  $\cdot\text{OH}$ , was added, it resulted in only a 7.5% decrease in the removal of PRO. Terephthalic acid (TA) was further used as a probe molecule for  $\cdot\text{OH}$ . As a result, only a slight  $\sim 7\%$  removal was observed in the 30 min electrocatalytic degradation process (**Fig. S26B**), which was consistent with the minor generation of their reaction product 2-hydroxyterephthalic acid (hTA, **Fig. S26C**). The contribution of  $\cdot\text{OH}$  measured using both TBU quenching and TA probe methods were very low and close in value. This conclusion was also consistent with the DMPO-EPR test result (**Fig. 3C**), where such a small amount of  $\cdot\text{OH}$  cannot be captured by DMPO-EPR with a strong enough peak signal.

Besides, we further confirmed that the detected  $\cdot\text{OH}$  primarily existed as dissolved  $\cdot\text{OH}_{\text{dis}}$  rather than adsorbed  $\cdot\text{OH}_{\text{ads}}$  (**Fig. S26D**). Some studies have classified the  $\cdot\text{OH}$  into dissolved radical ( $\cdot\text{OH}_{\text{dis}}$ ) and adsorbed radical ( $\cdot\text{OH}_{\text{ads}}$ ), and the  $\cdot\text{OH}_{\text{ads}}$  will not be quenched by the TBU(42, 77). So the buffered phosphate, a strong quencher for  $\cdot\text{OH}_{\text{ads}}$ (42), was added to assess the contribution of  $\cdot\text{OH}_{\text{ads}}$  (**Fig. S26D**). Considering that the addition of buffered phosphate will slightly increase (by  $\sim 28\%$ ) the conductivity of the solution, an additional experiment was carried out under the same solution conductivity by increasing the concentration of  $\text{Na}_2\text{SO}_4$ . The obtained results eliminated the effect of the increased conductivity. Consequently, the addition of the phosphate did not inhibit the removal of PRO, indicating that the  $\cdot\text{OH}_{\text{ads}}$  was not the main contributor to the pollutant removal. The applied cell voltage (3 V) may not be sufficient to produce a large amount of effective  $\cdot\text{OH}$ . Generally,  $\text{O}_2^{\cdot-}$  is produced more

in the process of cathodic electrocatalysis. In this study, most of the anode generated  $\text{O}_2^{\cdot-}$  might be converted to  $^1\text{O}_2$ .

### Supplementary Section VIII

**The detection of adsorbed  $\text{SO}_4^{2-}$ .** The MeOH is able to simultaneously quench the  $\cdot\text{OH}$  and  $\text{SO}_4^{2-}$ , while the TBU can only quench the  $\cdot\text{OH}$ (78). Therefore, the difference of PRO removal rate between the MeOH and TBU quenching tests indicates the contribution of  $\text{SO}_4^{2-}$ . As shown in **Fig. S26A**, there was almost no difference of degradation performance of between the MeOH-quenched and TBU-quenched tests. This suggested that the  $\text{SO}_4^{2-}$  was not the main contributor to the pollutant removal. In principle,  $\text{SO}_4^{2-}$  is mainly produced in persulfate catalysis, not in the absence of persulfate process.

### Supplementary Section IX

**Sub-nanocluster structure enhances hydraulic mass transfer.** For the classical microfiltration membrane with finger-like pore structures (**Fig. S28C**), the concentration of pollutants in the center area of the pores (channels) was higher than that on the wall of the channel. The  $\text{TiO}_x\text{C}_y$  membrane and CN membrane with highly interconnected framework could remit this mass transfer limitation (**Fig. S28A and B**) due to the forced convection and the confinement effect by the network topology(50). The mass transfer could be further enhanced in the  $\text{TiO}_x\text{C}_y$  membrane due to its larger specific surface area and additional turbulence caused by the  $\text{TiO}_x\text{C}_y$  nanoparticles. The computed  $c/c_0$  results in the effluent area for the  $\text{TiO}_x\text{C}_y$ , CN, and classical membranes are 0.23, 0.36. and 0.43, respectively. The difference of the  $N_c$  distribution of the three structures also showed the advantage of the  $\text{TiO}_x\text{C}_y@\text{CN}$  framework (**Fig. S28D–F**).

## Supplementary Section X

**Detailed methodology for ECSA calculation.** The ECSA was derived from the electrochemical double-layer capacitance of the electrode(57), which was obtained by performing cyclic voltammetry (CV) sweeps in a standard three-electrode electrochemical workstation at different scanning rates (i.e., 10, 20, 40, 60, 80, and 100  $\text{mV s}^{-1}$ ). An inert titanium mesh served as the counter electrode, an Ag/AgCl electrode was employed as the reference electrode, and the prepared electrode sample acted as the working electrode. Both the working electrode and the counter electrode had an apparent geometric area of  $1 \text{ cm}^2$ . The electrolyte solutions comprised 10 mM  $\text{Na}_2\text{SO}_4$  and  $20 \text{ mg L}^{-1}$  PRO, identical to the solutions used for electrocatalytic degradation of pollutants by  $\text{TiO}_x\text{C}_y$  membrane. Prior to conducting the CV scans, the assembled three-electrode system was stabilized for at least 30 minutes to ensure a stable open-circuit potential (OCP).

The bilayer capacitance  $C_{\text{DL}}$  was calculated from the current density ( $i_c$ ,  $\text{mA cm}^{-2}$ ) – scan rate ( $v$ ,  $\text{mV s}^{-1}$ ) curve of CV scans at different scan rates (Plotting  $i_c$  as a function of  $v$  as a line with a fitted slope equal to  $C_{\text{DL}}$ )(79):

$$i_c = C_{\text{DL}} v \quad (\text{S2})$$

The linear regression analysis was performed using the OriginPro software (OriginLab, USA). The ECSA can be subsequently calculated by dividing the  $C_{\text{DL}}$  by the specific capacitance ( $C_s$ ):

$$\text{ECSA} = C_{\text{DL}} / C_s \quad (\text{S3})$$

The adopted specific capacitance ( $C_s$ ) is  $40 \mu\text{F cm}^{-2}$  (most commonly used value in the literature(79)). Although minor deviations may exist depending on the specific materials and experimental conditions, this value serves as a common baseline(79), enabling standardized and meaningful comparisons across different studies.

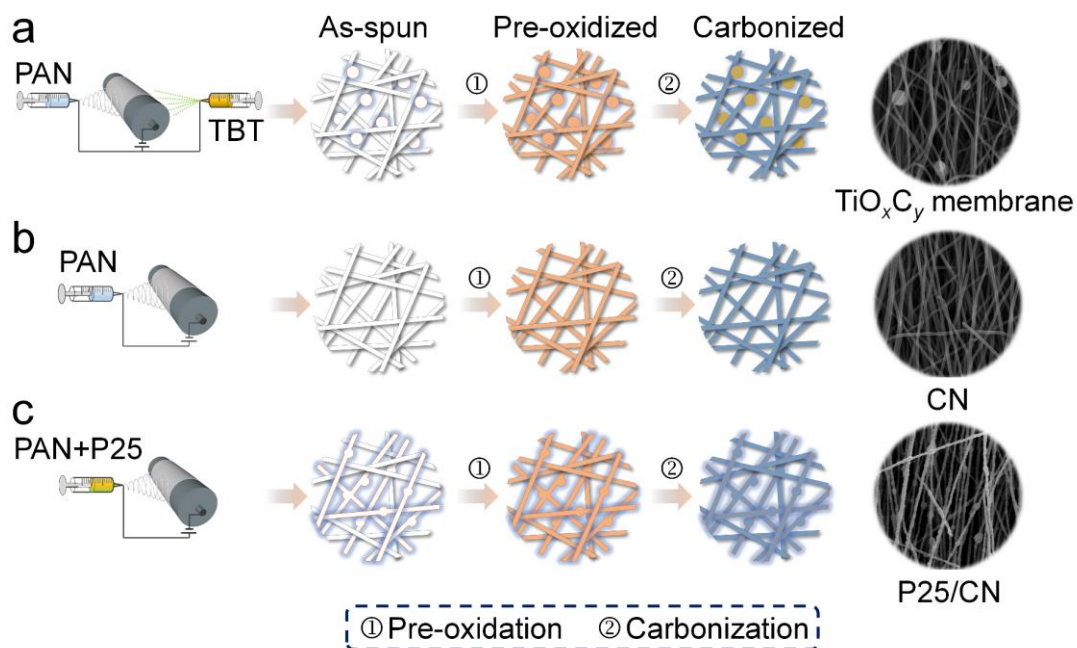


**Fig. S1. Schematic of different membrane preparation processes.** Fabrication protocols of the (a) TiO<sub>x</sub>C<sub>y</sub> membrane, (b) CN (served as a control), and (c) P25/CN (served as a control) membranes with their SEM images included aside.

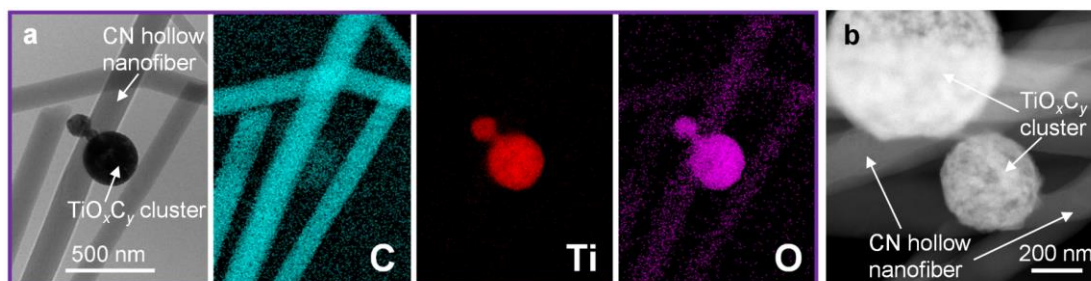


**Fig. S2. Microscopic characterization of the TiO<sub>x</sub>C<sub>y</sub> membrane.** (a and b) TEM and (a) EDS mapping of the TiO<sub>x</sub>C<sub>y</sub> membrane.

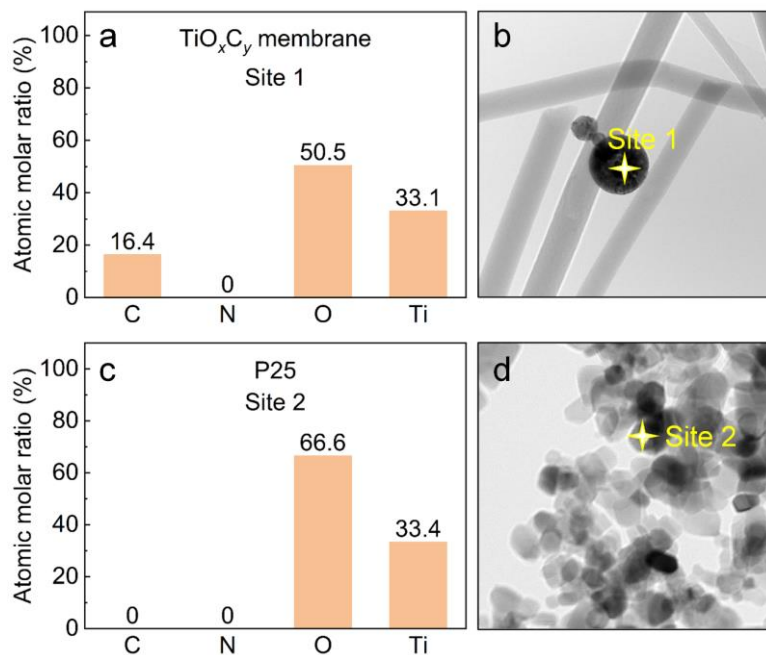


**Fig. S3. High-resolution EDS characterization of the TiO<sub>x</sub>C<sub>y</sub> membrane.** (a) Local elemental composition of (b) a nanoparticle in the TiO<sub>x</sub>C<sub>y</sub> membrane determined by EDS in a point scan mode. (c) Elemental composition of the (d) commercial P25 nanoparticle. The corresponding sites for the measurements are separately labeled on their TEM images.

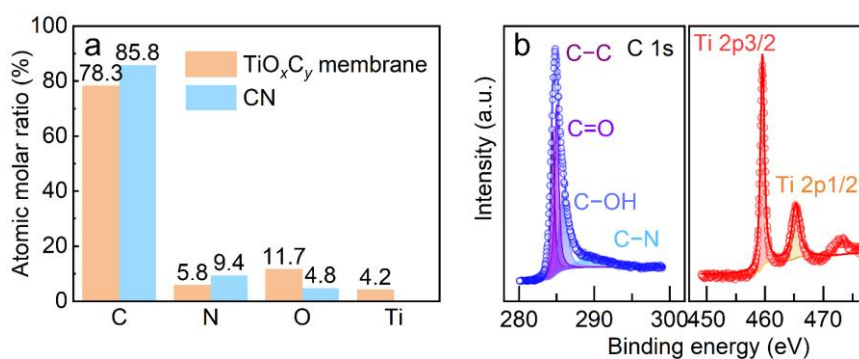


**Fig. S4. XPS characterization of the TiO<sub>x</sub>C<sub>y</sub> membrane.** (a) Comparison of the overall elemental compositions measured by XPS between the TiO<sub>x</sub>C<sub>y</sub> membrane and CN membrane. (b) XPS spectra displaying the C 1s and Ti 2p regions of the TiO<sub>x</sub>C<sub>y</sub> membrane.

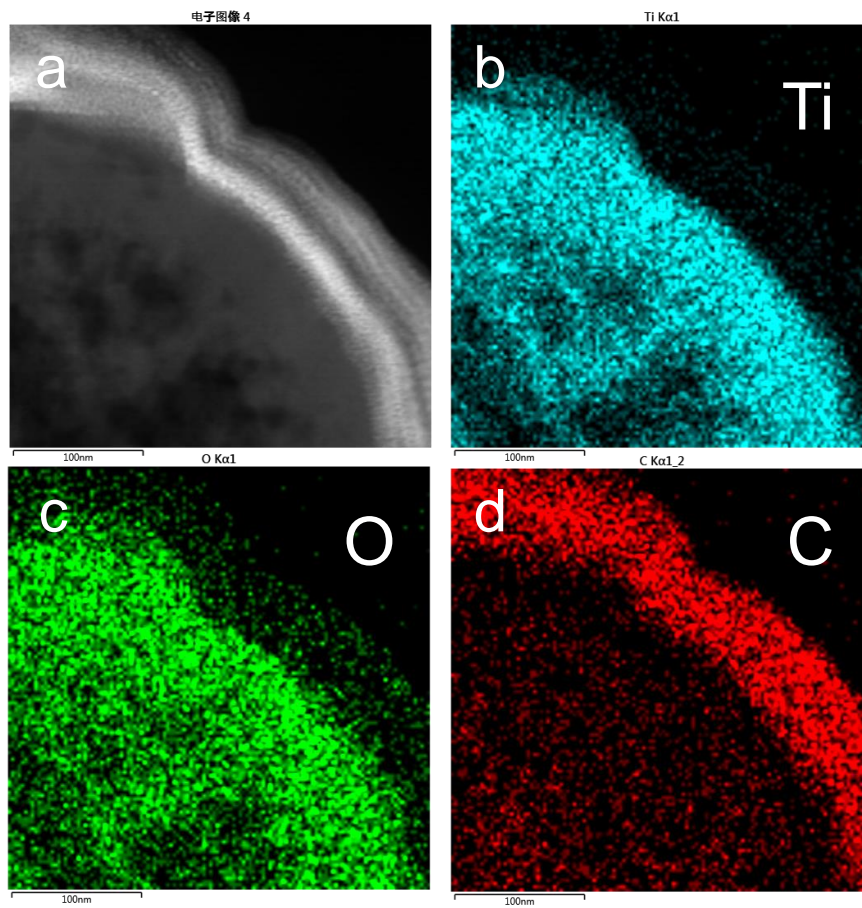


**Fig. S5. EDS mapping results show that the cluster has a well-defined carbon shell.**  
(a) TEM, (b) Ti elemental mapping, (c) O elemental mapping, and (d) C elemental mapping images of the  $\text{TiO}_x\text{C}_y$  membrane.

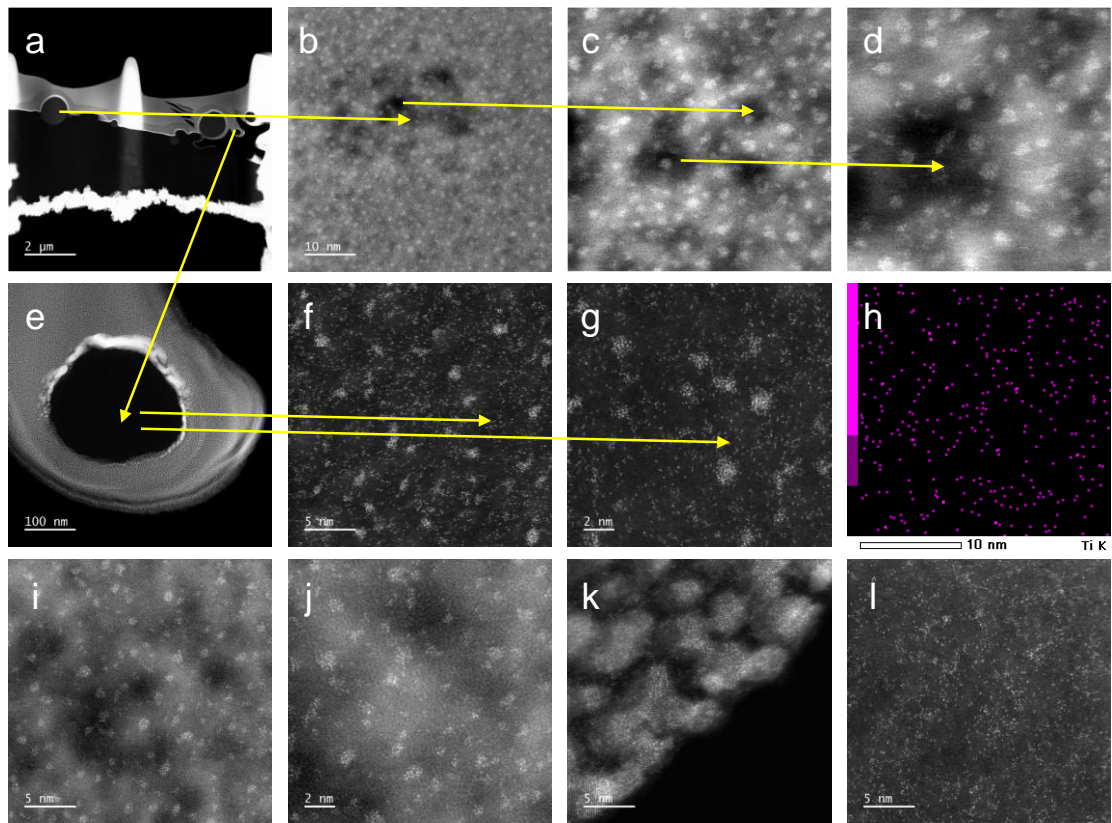


**Fig. S6. Further aberration-corrected HAADF-STEM characterization of the cross sections of as-spun and pre-oxidized  $\text{TiO}_x\text{C}_y$  membrane.** (a–h) Aberration-corrected HAADF-STEM characterization of the cross sections of as-spun: (b–d) inside the cluster and (f–h) inside the CN. (i–l) Aberration-corrected HAADF-STEM characterization of the cross sections of pre-oxidized samples: (i–j) inside the cluster, (k) wall of CN, and (l) inside the CN.

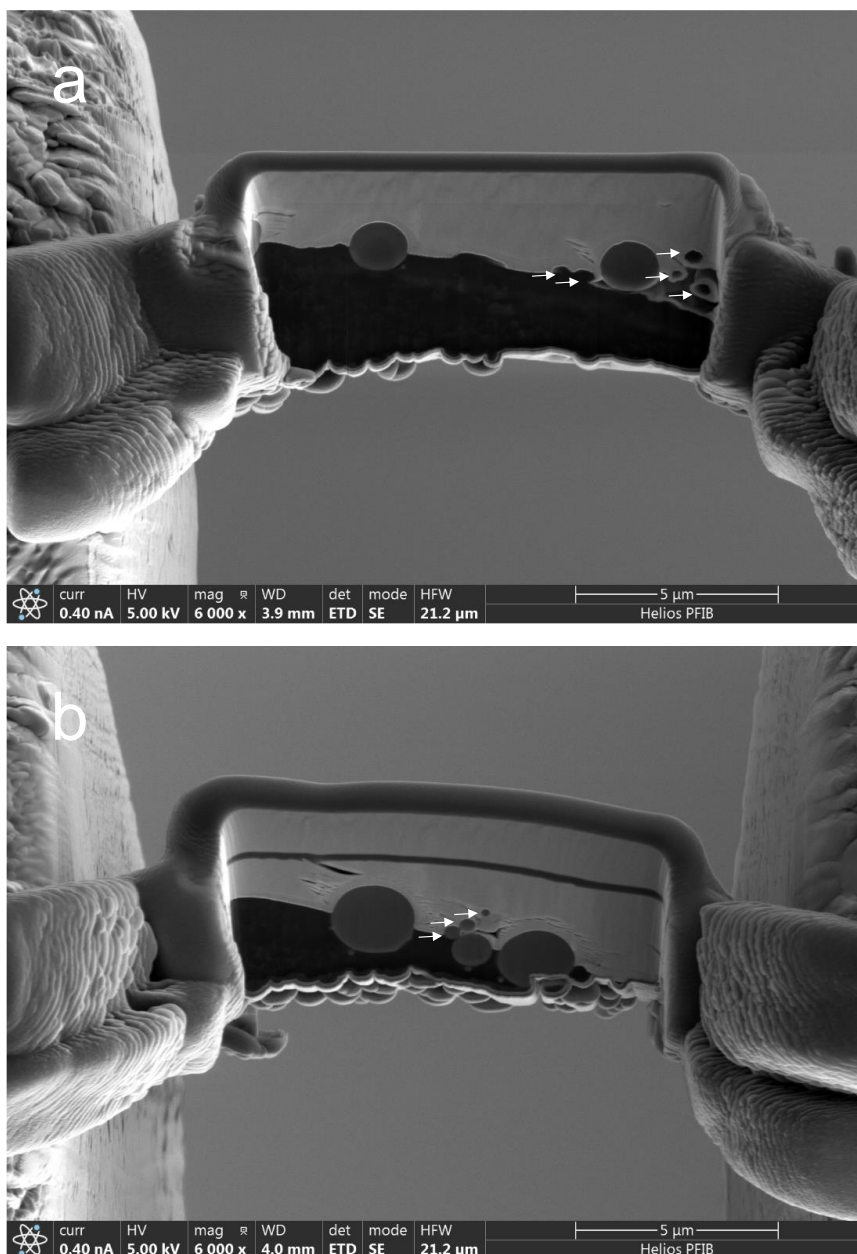


**Fig. S7. FIB-SEM view of as-spun and pre-oxidized samples.** An FIB-SEM view of the cross section of the (a) as-spun and (b) pre-oxidized  $\text{TiO}_x\text{C}_y$  membrane. The small black holes correspond to the hollow area of the CNs, indicating that the hollow structure was formed right after the DESP process.

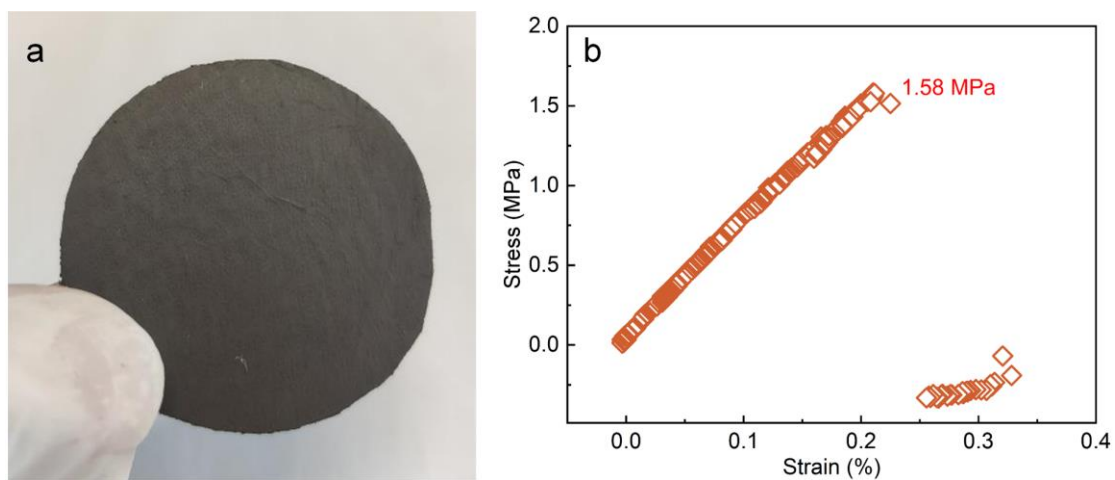


**Fig. S8. A photograph and the tensile stress–strain curve of the self-supported  $\text{TiO}_x\text{C}_y$  membrane.** (a) A representative photograph of the prepared self-supported  $\text{TiO}_x\text{C}_y$  membrane (diameter: 20 mm; and thickness: 0.35 mm). (b) Measured tensile stress–strain curve of the  $\text{TiO}_x\text{C}_y$  membrane.

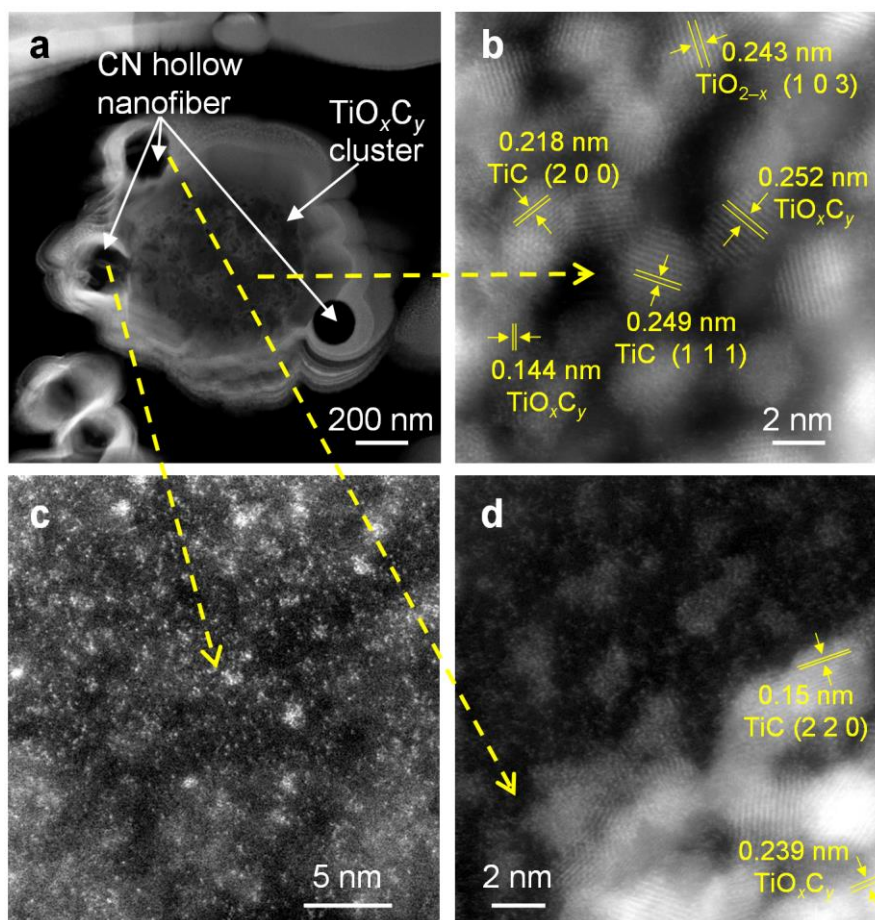


**Fig. S9. Further microscopic imaging by aberration-corrected HAADF-STEM of the  $\text{TiO}_x\text{C}_y$  membrane.** The (a) FIB-SEM view shows the 3D structure of the  $\text{TiO}_x\text{C}_y$  membrane: 3D highly dispersed  $\text{TiO}_x\text{C}_y$  clusters in a 3D CN network. (b)  $\text{TiO}_x\text{C}_y$  were observed inside the clusters by aberration-corrected HAADF-STEM. Further microscopic imaging by aberration-corrected HAADF-STEM of the CNs in (a), showing the presence of (c) single atomic Ti in the hollow CN and (d) TiC and  $\text{TiO}_x\text{C}_y$  at the junctions of the CNs and  $\text{TiO}_x\text{C}_y$  clusters.

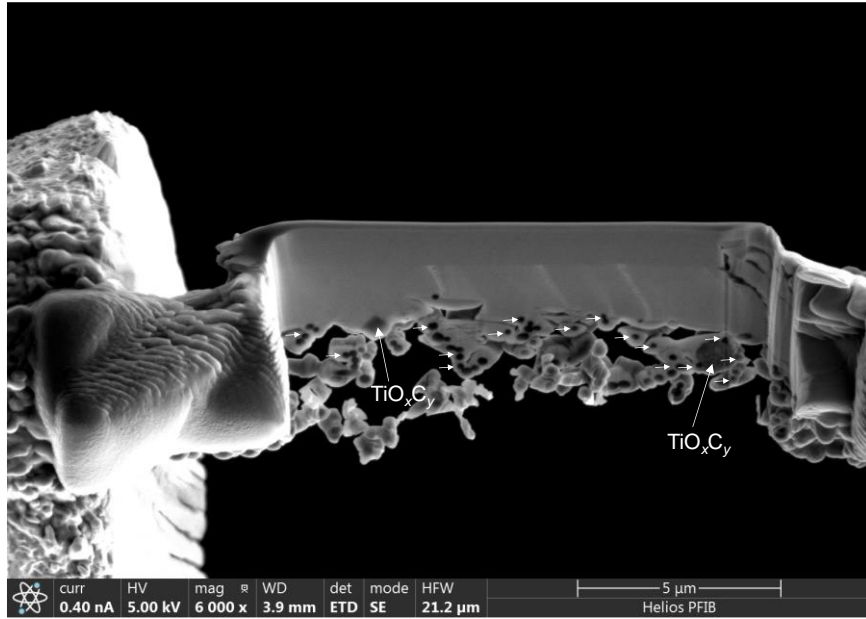


**Fig. S10.** An FIB-SEM view of the cross section of the  $\text{TiO}_x\text{C}_y$  membrane. The small black holes correspond to the hollow area of the CNs, while the large spheres correspond to the  $\text{TiO}_x\text{C}_y$  sub-3nm clusters.

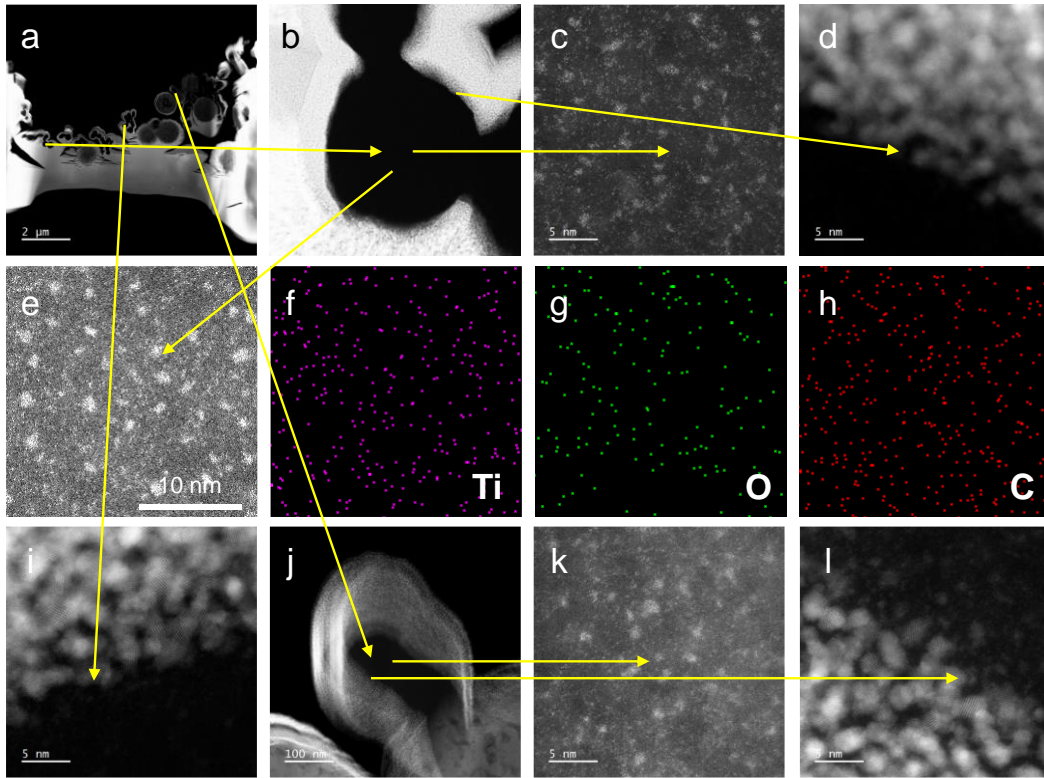


**Fig. S11.** Even inside the CNs away from the  $\text{TiO}_x\text{C}_y$  clusters are spread with single atomic Ti of the  $\text{TiO}_x\text{C}_y$  membrane. (a–e, i–l) Aberration-corrected HAADF-STEM view of single atomic Ti inside CN far away from  $\text{TiO}_x\text{C}_y$  clusters and  $\text{TiO}_x\text{C}_y$  lattice on the wall; (f–h) EDS-mapping of the location of (e).

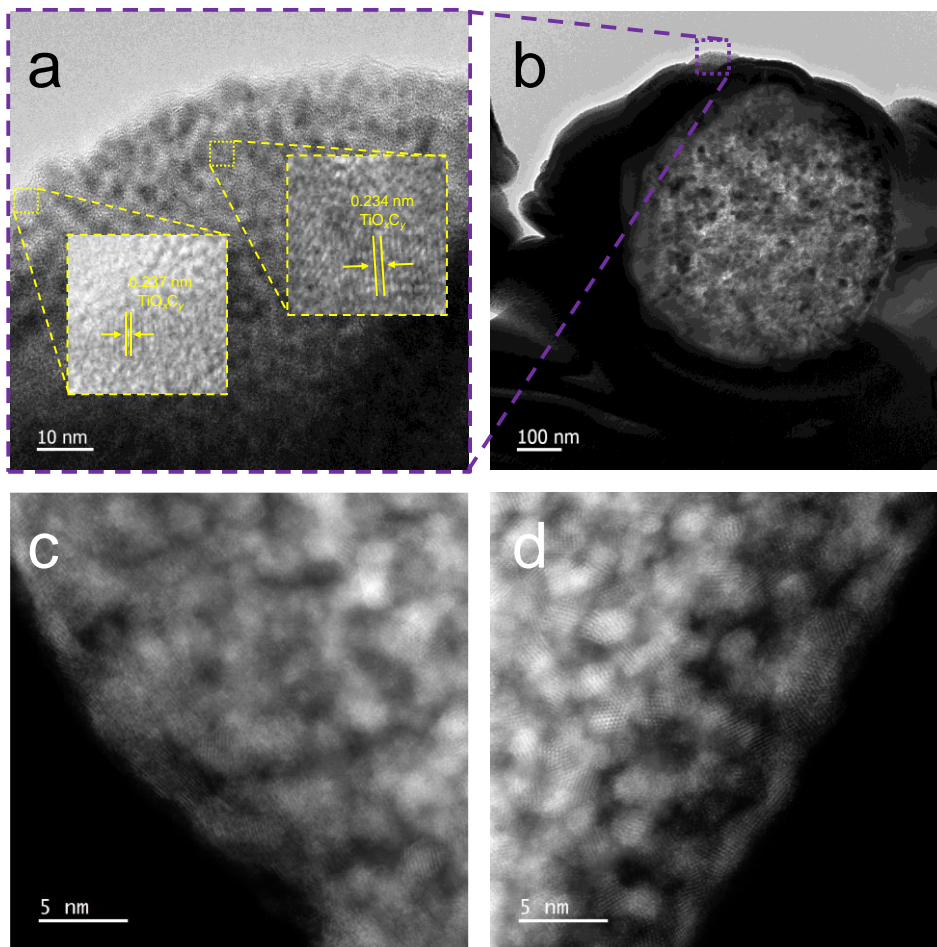


**Fig. S12. TEM view of the carbon shell of the  $\text{TiO}_x\text{C}_y$  cluster. (a–d)  $\text{TiO}_2$  lattice can be observed in the carbon shell of the cluster.**

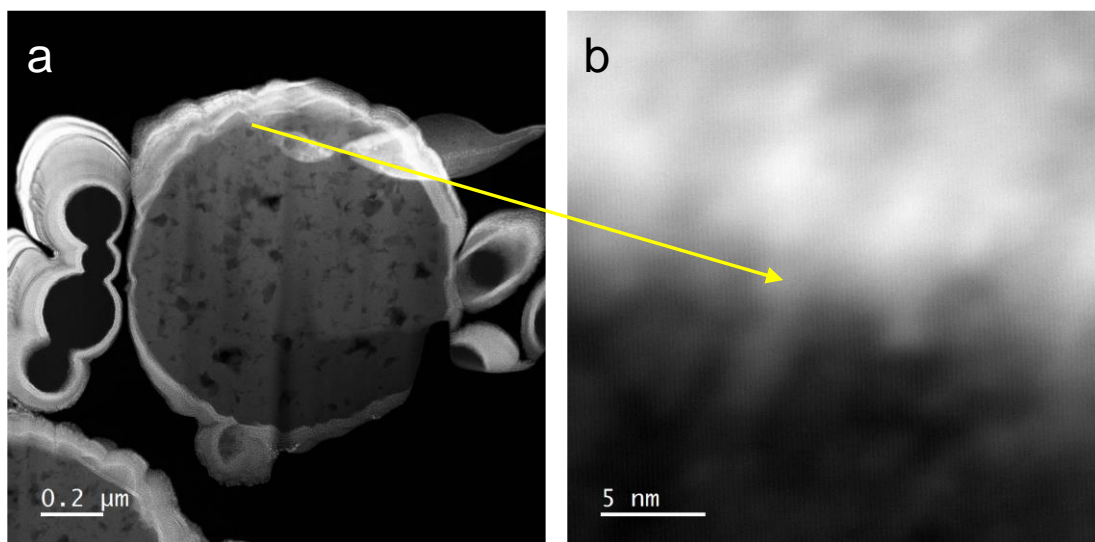


**Fig. S13.** The hollow CN has been completely fused with the carbon shell of the  $\text{TiO}_x\text{C}_y$  cluster. Aberration-corrected HAADF-TEM views of the (a)  $\text{TiO}_x\text{C}_y$  cluster particle and (b) the magnified interface between the  $\text{TiO}_x\text{C}_y$  main core and the carbon shell.

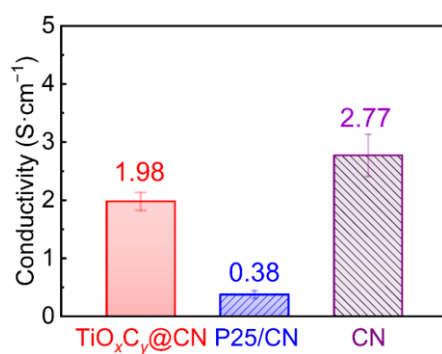


**Fig. S14. Conductivity of the different membranes.** High conductivity due to the oxygen defects of  $\text{TiO}_x\text{C}_y$  and hierarchical structure, the integration of  $\text{TiO}_x\text{C}_y$  did not substantially reduce the electrical conductivity (12.4  $\text{S/gC}$  for  $\text{TiO}_x\text{C}_y$  membrane compared to 13.2  $\text{S/gC}$  for CN).

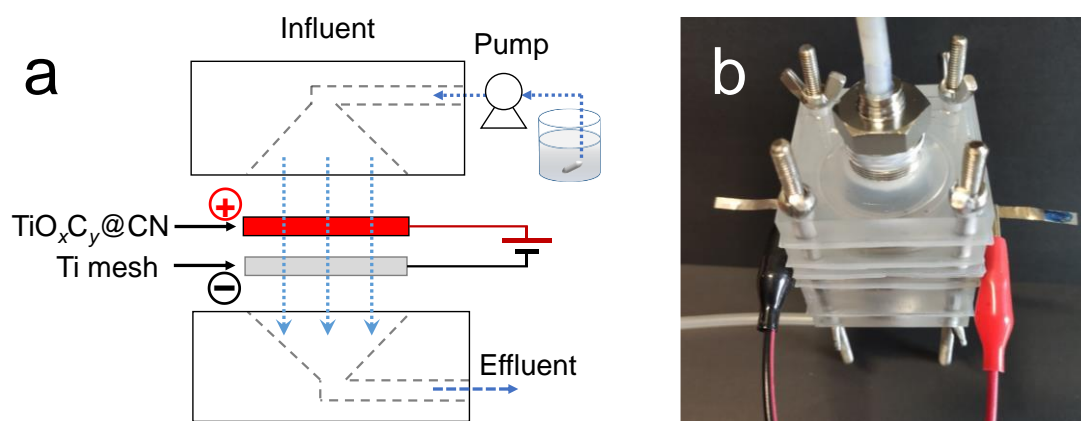


**Fig. S15. Detailed system configuration of the EMF set up. (a)** Schematic configuration and **(b)** a photo of the EMF system, where the electrocatalytic membrane is incorporated as the anode with an inert titanium mesh (nominal pore size  $\sim 0.7$  mm) as the cathode.

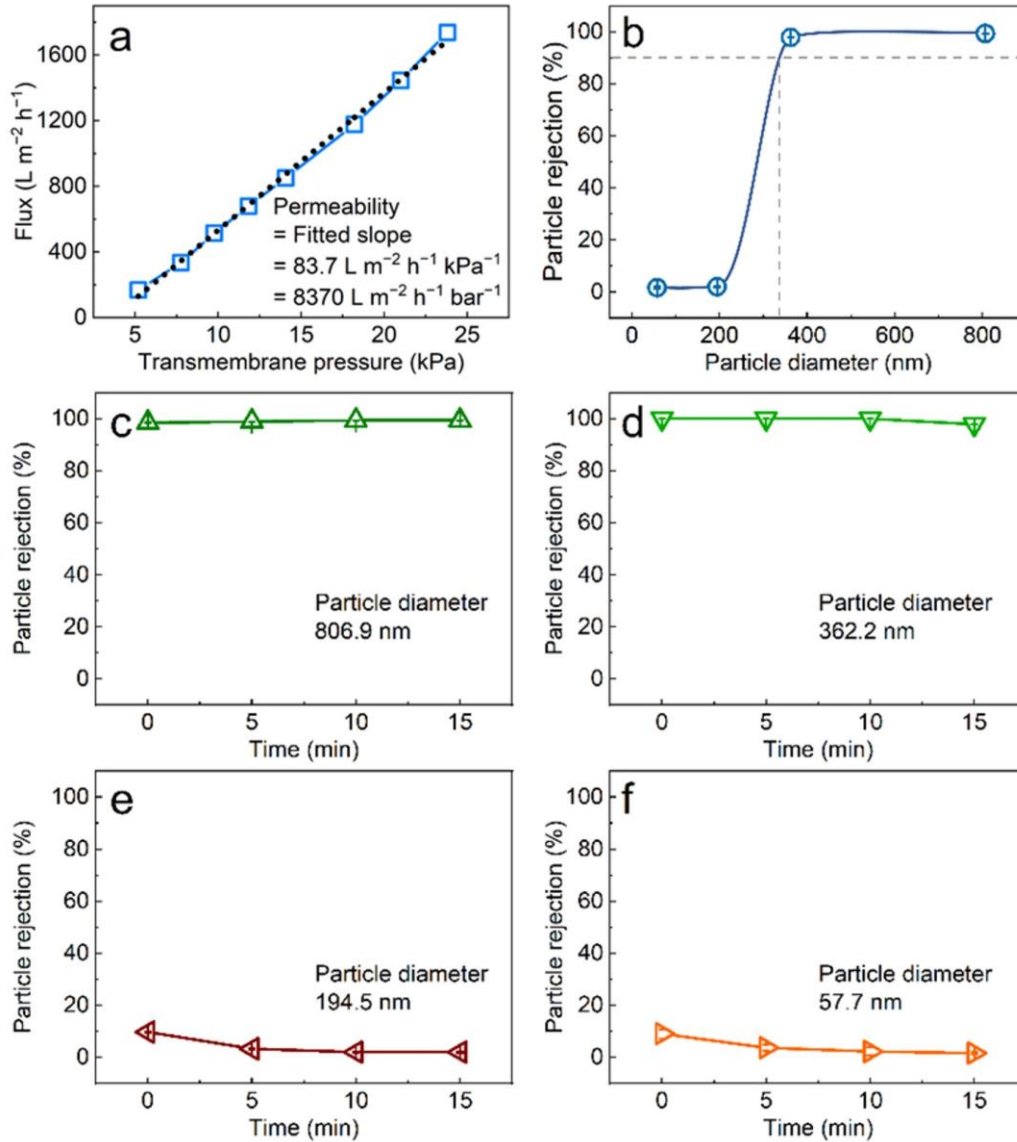


**Fig. S16. Filtration performance of the  $\text{TiO}_x\text{C}_y$  membrane.** (a) Measured pure water flux at different transmembrane pressures. The permeability of  $8370 \text{ L m}^{-2} \text{h}^{-1} \text{bar}^{-1}$  was calculated by fitting the flux-pressure data linearly and then based on the slope of the fit. (b) Measured micro-particle rejection rates at different particle diameters. Detailed rejection performance for the different micro-particles of (c) 806.9, (d) 362.2, (e) 194.5, and (f) 57.7 nm.

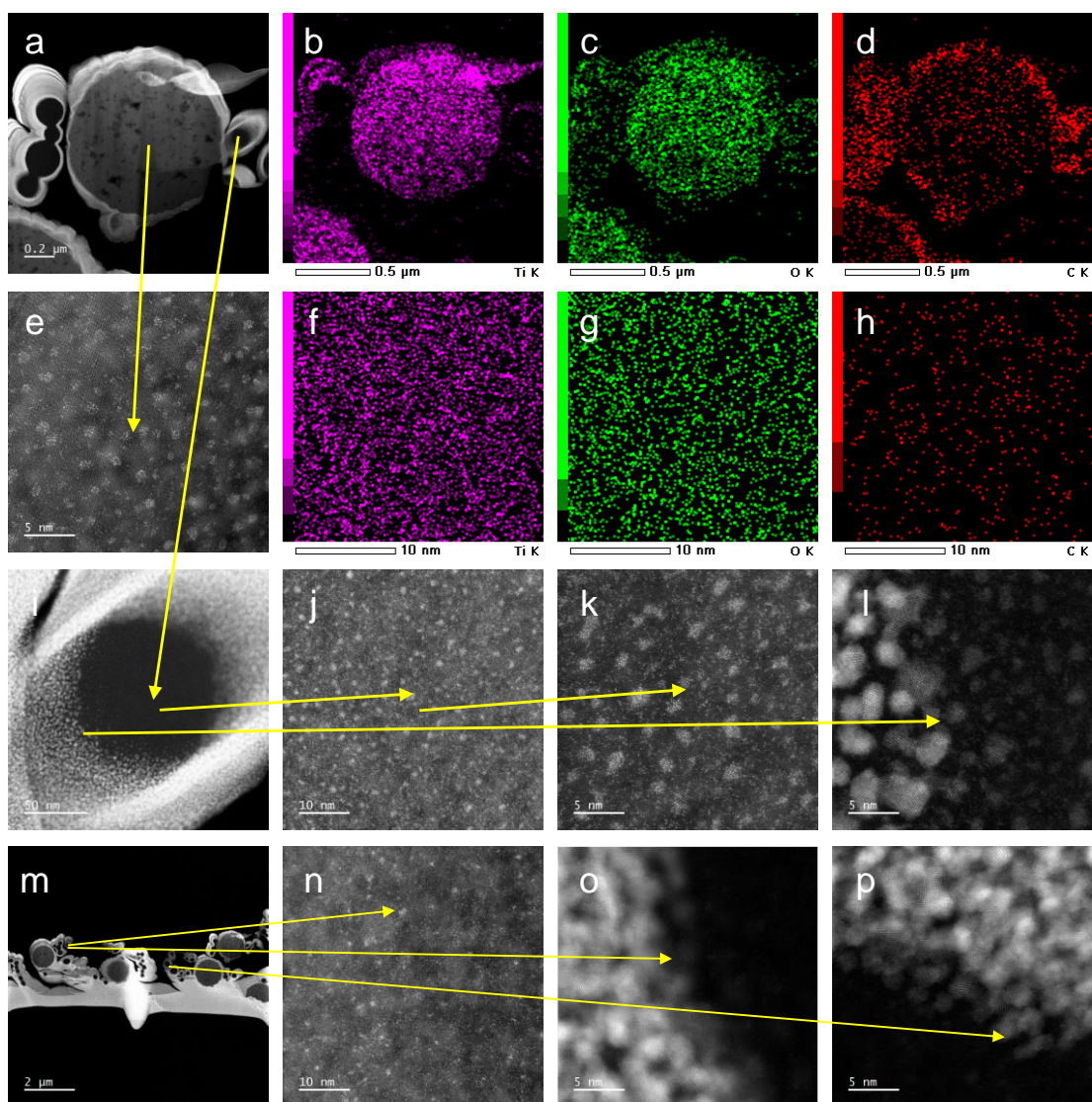


**Fig. S17. Characterizations of  $\text{TiO}_x\text{C}_y$  membrane after electrochemical use. (a–d)** Aberration-corrected HAADF-STEM view and EDS-mapping of  $\text{TiO}_x\text{C}_y$  cluster. **(e–h)** Aberration-corrected HAADF-STEM view and EDS-mapping of single atomic Ti inside the  $\text{TiO}_x\text{C}_y$  cluster. **(i–l)** Aberration-corrected HAADF-STEM view of single atomic Ti inside CN and  $\text{TiO}_x\text{C}_y$  lattice on the wall of CN. **(m–p)** Aberration-corrected HAADF-STEM view of single atomic Ti inside CN far away from  $\text{TiO}_x\text{C}_y$  clusters and  $\text{TiO}_x\text{C}_y$  lattice on the wall.

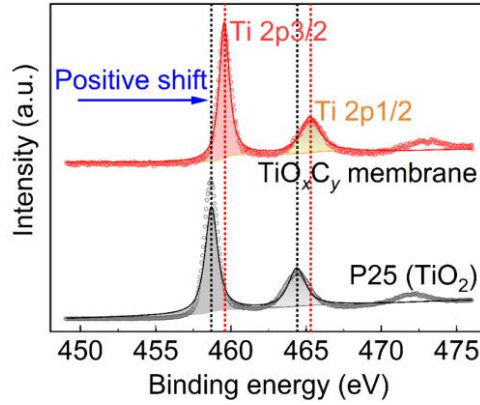


**Fig. S18. Comparison of the XPS spectra of the  $\text{TiO}_x\text{C}_y$  membrane and commercial P25 ( $\text{TiO}_2$ ) particles.**

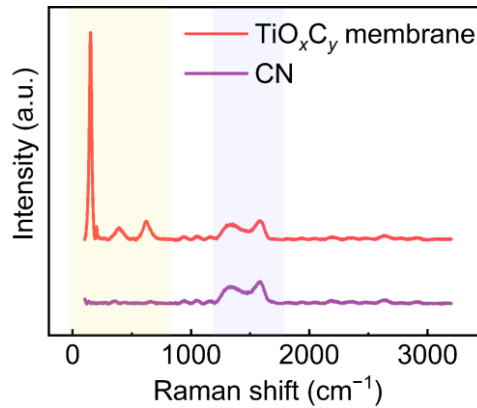


**Fig. S19. Raman spectra of the  $\text{TiO}_x\text{C}_y$  and CN membranes.**

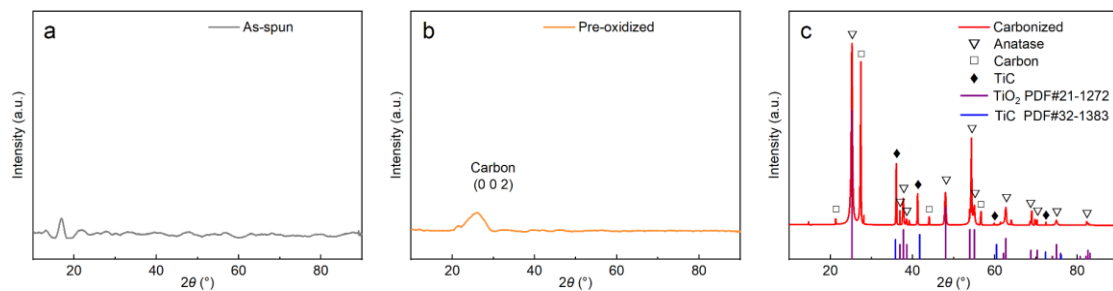


**Fig. S20. XRD patterns of the membrane samples at different fabrication stages: (a) as-spun, (b) pre-oxidized, (c) and carbonized. These results indicated that the anatase crystal and TiC structure was formed at the carbonization stage.**

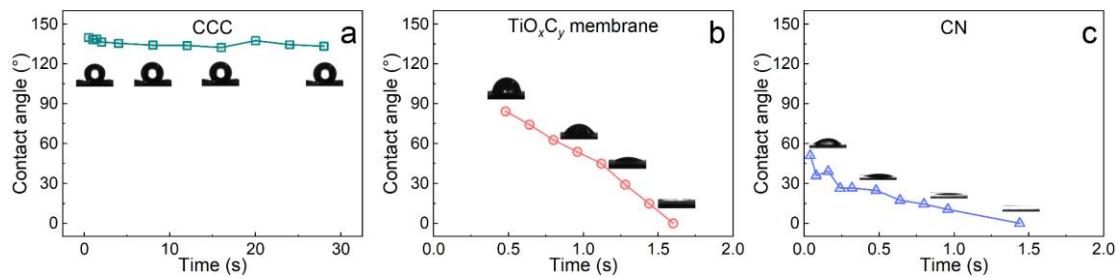


**Fig. S21.** Detailed contact angle variations along with time on the (a) commercial carbon cloth (CCC), (b) TiO<sub>x</sub>C<sub>y</sub> membrane, and (c) CN membrane.

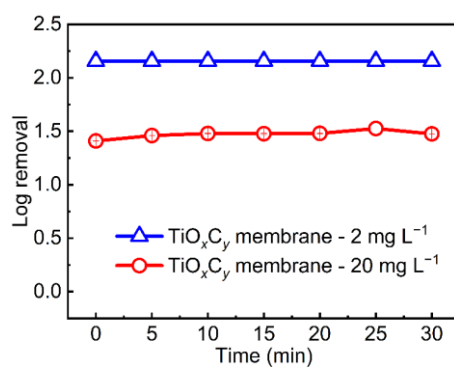


**Fig. S22.** Comparison of the electrocatalytic performance in terms of the propranolol (PRO) removal rate at different influent concentrations (i.e., 2 and 20 mg L<sup>-1</sup>) by the TiO<sub>x</sub>C<sub>y</sub> membrane.

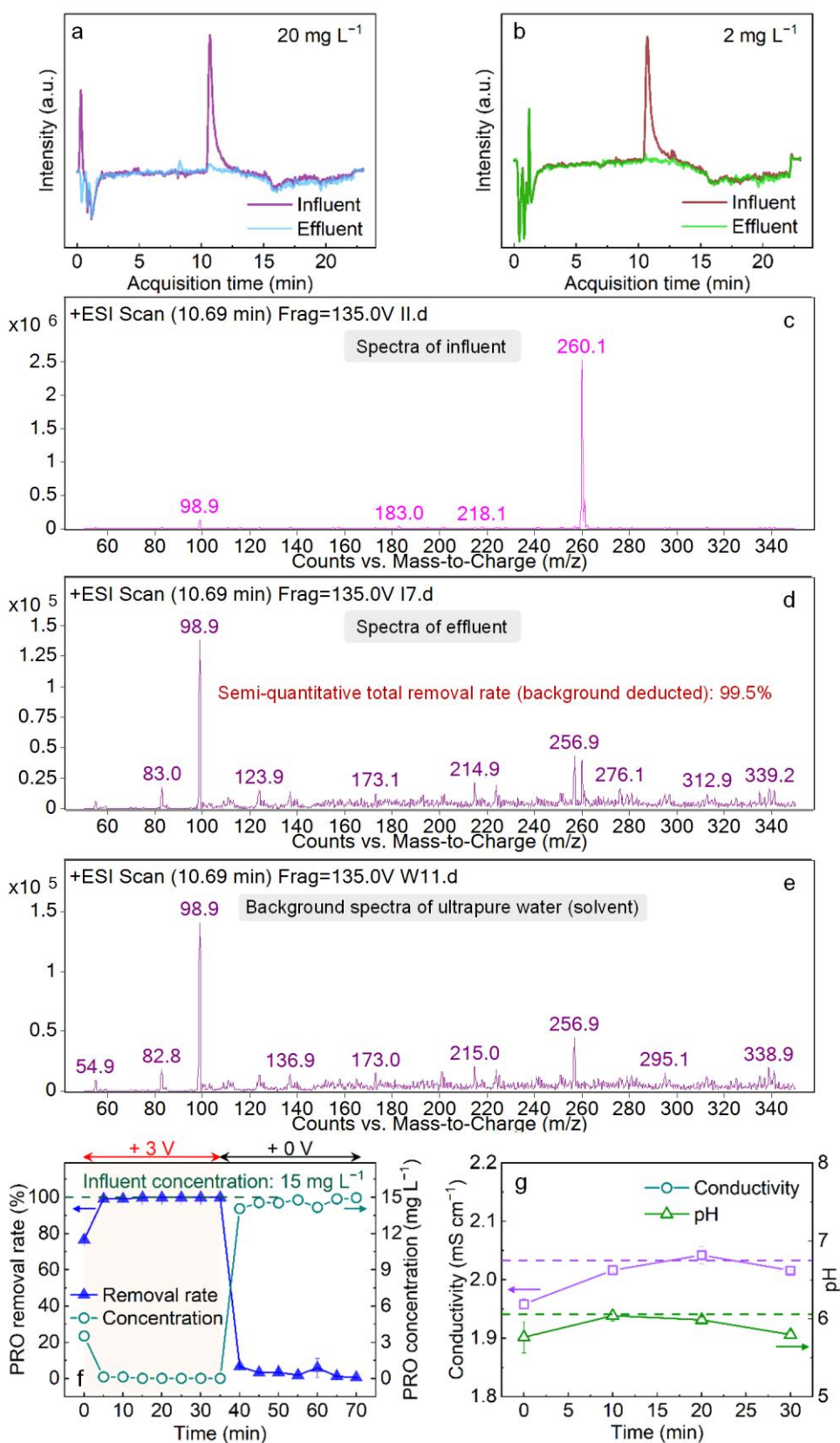


**Fig. S23. Further analysis for PRO degradation by the TiO<sub>x</sub>C<sub>y</sub> membrane. (a and b) Comparison of the total ion current spectra measured by HPLC-MS/MS between the**

influent and effluent at different PRO concentrations: (a) 20 mg L<sup>-1</sup> and (b) 2 mg L<sup>-1</sup>. Corresponding mass spectra of (c) influent at 2 mg L<sup>-1</sup> PRO, (d) effluent, and (e) ultrapure water background. (f) An EMF test based on the TiO<sub>x</sub>C<sub>y</sub> membrane and 15 mg L<sup>-1</sup> PRO influent to evaluate the contribution of electrosorption to the removal of pollutants. Note: if electrosorption apparently contributed to the removal, the effluent PRO concentration would rise beyond its influent value with a corresponding negative removal rate when the applied voltage was cut off at 35 min. (g) Variations of the effluent pH and conductivity during the EMF test based on the TiO<sub>x</sub>C<sub>y</sub> membrane and 20 mg L<sup>-1</sup> PRO influent. The green and purple dotted lines indicate the influent pH and conductivity, respectively.

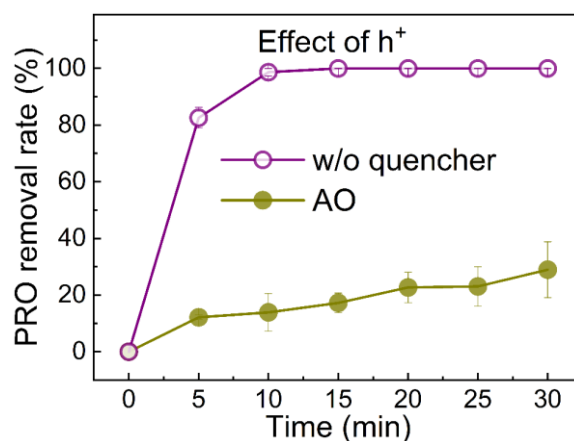


**Fig. S24. Quenching tests demonstrating the effect of  $h^+$  (quenched by 100 mM ammonium oxalate (AO)) on the degradation of PRO ( $20 \text{ mg L}^{-1}$ ) during the cyclic EMF process (3 V).**

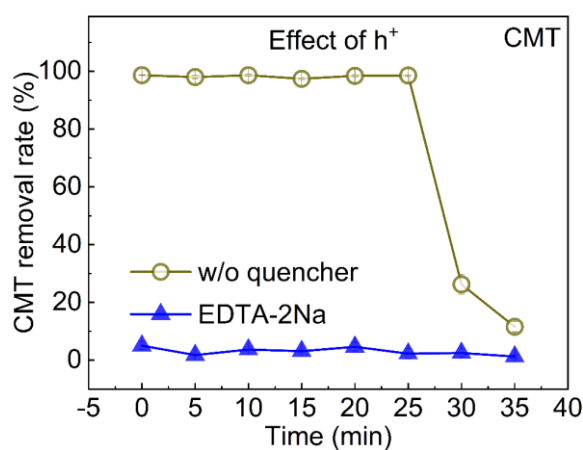


**Fig. S25. Quenching tests further verifying the effect of  $h^+$  oxidation (quenched with 100 mM EDTA-2Na) using CMT ( $2 \text{ mg L}^{-1}$ ) as the model pollutant under a continuous flow mode.**

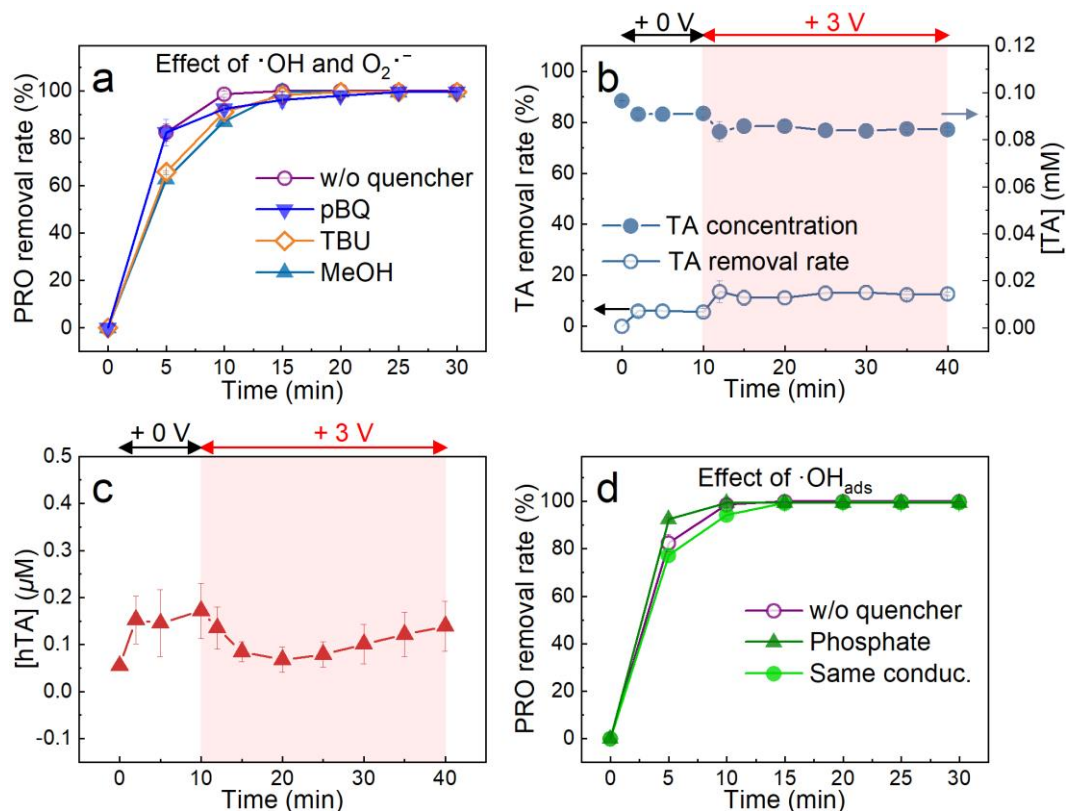


**Fig. S26. Further revealing the mechanism of electrocatalytic degradation performance of the  $\text{TiO}_x\text{C}_y$  membrane.** (a) Quenching tests investigating the effect of  $\text{O}_2^{\cdot-}$  (quenched with 2 mM pBQ),  $\cdot\text{OH}$  (quenched with 100 mM TBU), and  $\text{SO}_4^{2\cdot-}$  (assessed by the difference between the results of the 100 mM MeOH quenching and the 100 mM TBU quenching, as MeOH quenches both  $\cdot\text{OH}$  and  $\text{SO}_4^{2\cdot-}$ ). (b) Probe test exploring the presence of  $\cdot\text{OH}$  through the degradation of 100  $\mu\text{M}$  TA by the  $\text{TiO}_x\text{C}_y$  membrane. (c) Variation of the measured concentrations of hTA (produced from the reaction between TA and  $\cdot\text{OH}$ ) during the probe-test with TA for the  $\text{TiO}_x\text{C}_y$  membrane. (d) Quenching tests investigating the effect of adsorbed  $\cdot\text{OH}_{\text{ads}}$  (quenched with 100 mM phosphate).

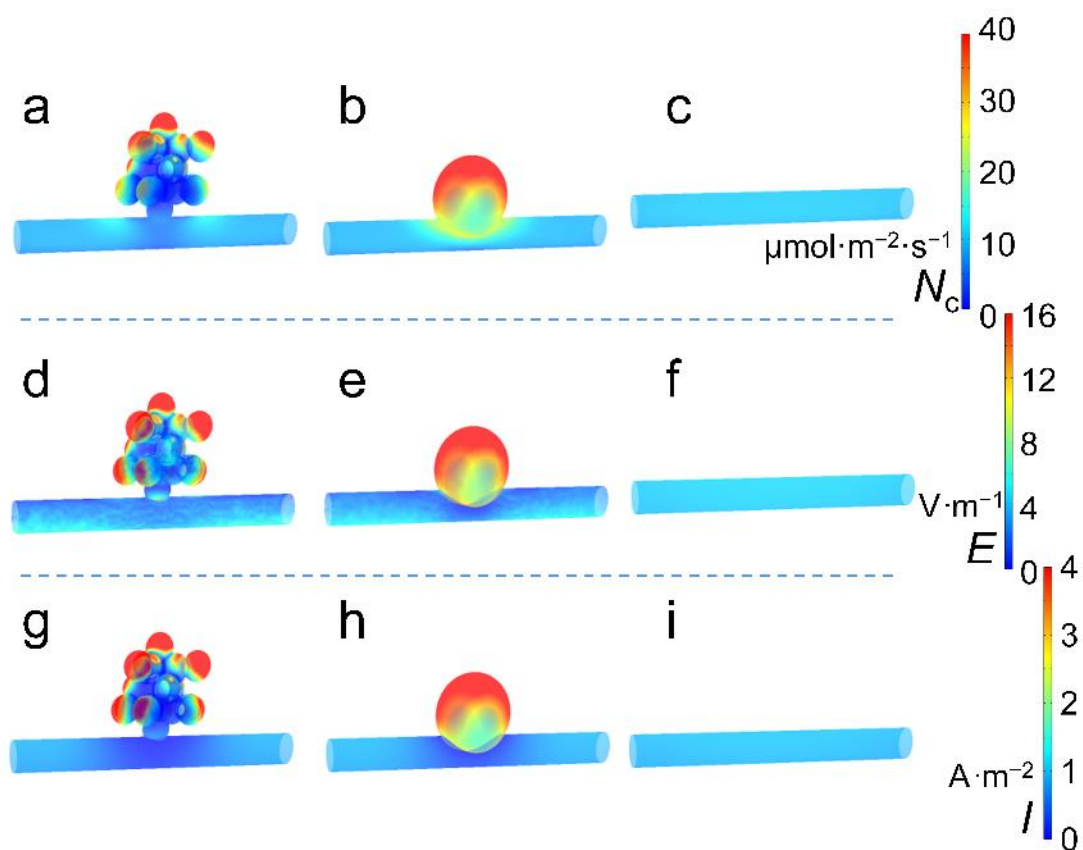


**Fig. S27. Simulation analyses revealing the influence of  $\text{TiO}_x\text{C}_y$  nanoreactor microscopic structure on key electrocatalytic parameters.** (a–c) Comparison of the computed distribution of pollutant mass flux ( $N_c$ ,  $\mu\text{mol m}^{-2} \text{s}^{-1}$ ) adjacent to membrane surface among the (a) simulated  $\text{TiO}_x\text{C}_y$  sub-nanocluster@CN membrane segment, (b) simulated  $\text{TiO}_x\text{C}_y$ @CN segment, and (c) simulated CN segment. (d–f) Comparison of the computed distribution of normal electric field intensity ( $E$ ,  $\text{V m}^{-1}$ ) among the (d)  $\text{TiO}_x\text{C}_y$  sub-nanocluster@CN, (e)  $\text{TiO}_x\text{C}_y$ @CN, and (f) CN segments. (g–i) Comparison of the computed distribution of normal current density ( $I$ ,  $\text{A m}^{-2}$ ) among the (g)  $\text{TiO}_x\text{C}_y$  sub-nanocluster@CN, (h)  $\text{TiO}_x\text{C}_y$ @CN, and (i) CN segments.

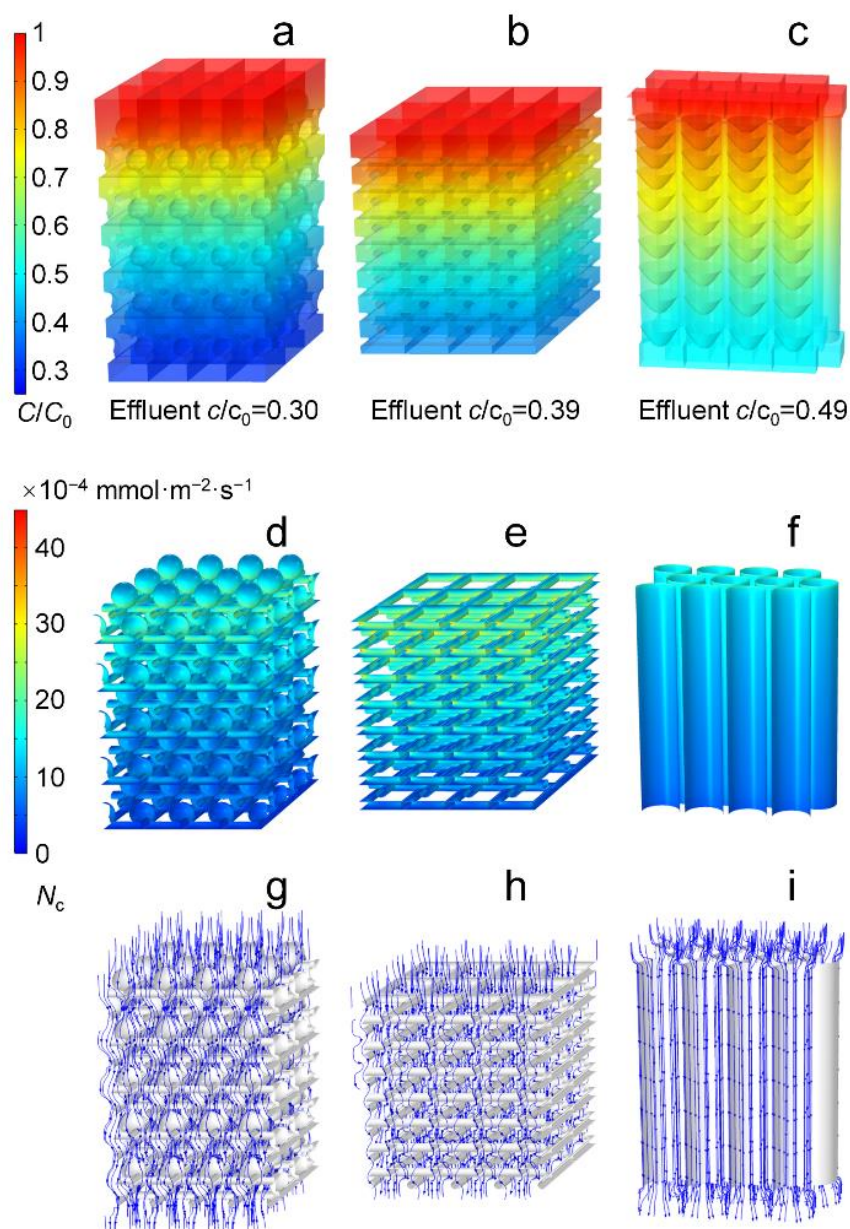


**Fig. S28. Simulation analyses revealing the unique hierarchical structure of the “nanofiber-nanocluster” of the  $\text{TiO}_x\text{C}_y$  membrane enhanced the hydraulic mass transfer. (a–c) Comparison of the computed distribution of pollutant concentration ( $c/c_0$ ) across the membrane among three multi-layer-stacked models: (a)  $\text{TiO}_x\text{C}_y$  membrane, (b) CN, and (c) classic microfiltration membrane with finger-like pore structures. (d–f) Comparison of the computed distribution of pollutant mass flux ( $N_c$ ) across the membrane among the (d)  $\text{TiO}_x\text{C}_y$  membrane, (e) CN, and (f) classic membrane models. (g–i) Comparison of the hydraulic flow regime across the membrane among the (g)  $\text{TiO}_x\text{C}_y$  membrane, (h) CN, and (i) classic membrane models.**

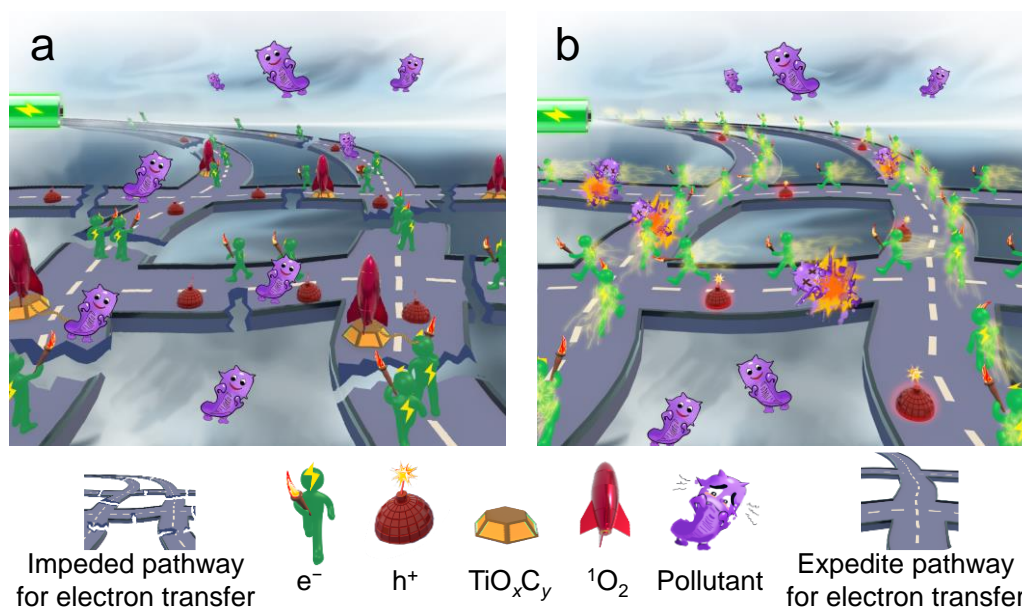


**Fig. S29. The conventional strategies for the P25/CN and CN membranes suffer from impeded electron transfer and unidimensional degradation capability.** Schematic illustrating two disadvantageous scenarios which could result in seriously reduced efficiency of electrocatalytic degradation: **(a)** impeded pathway for electron transfer (e.g., membrane prepared through the mixed matrix strategy where the deeply embedded catalysts severely narrow the pathway for electron transfer) and **(b)** limited capability of  $^1O_2$  production (e.g., the CN membrane).

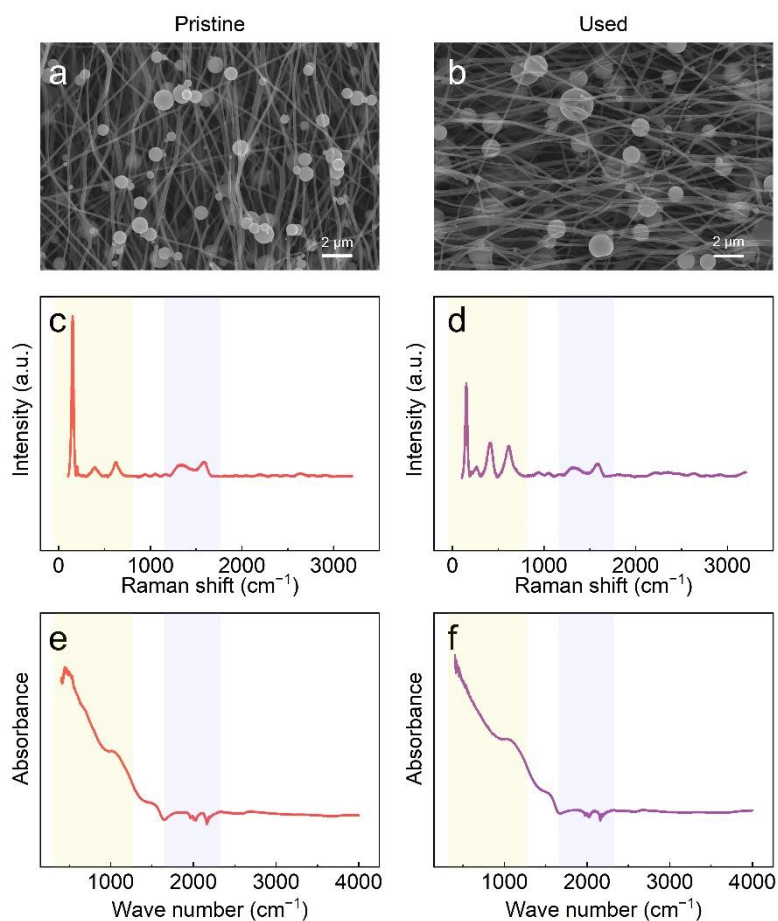


**Fig. S30. Comparisons in terms of morphology and chemical compositions of the  $\text{TiO}_x\text{C}_y$  membrane between its pristine and long-term-used states.** SEM images of the (a) pristine and (b) used  $\text{TiO}_x\text{C}_y$  membranes. Raman spectra of the  $\text{TiO}_x\text{C}_y$  membrane between its (c) pristine and (d) long-term-used states. FTIR spectra of the  $\text{TiO}_x\text{C}_y$  membrane between its (e) pristine and (f) long-term-used states.

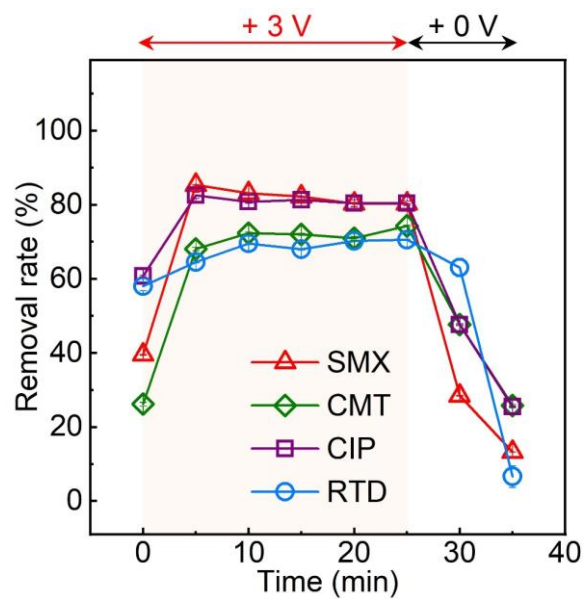


**Fig. S31.** Compared electrocatalytic degradation performance by P25/CN membrane for different pollutants: SMX, CMT, CIP and RTD; all at  $2 \text{ mg L}^{-1}$ .

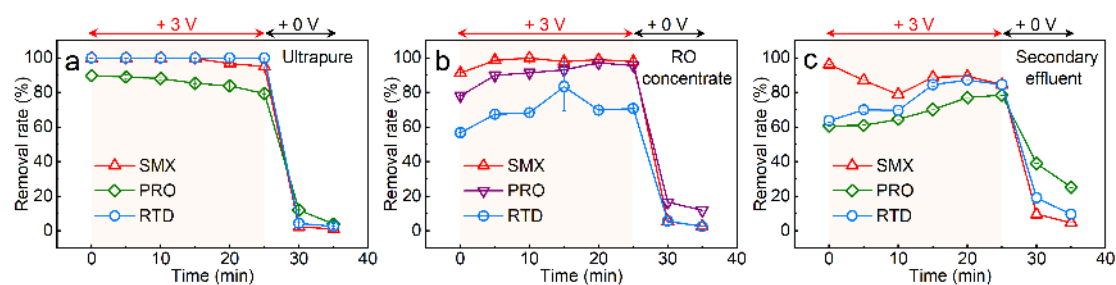


**Fig. S32. Electrocatalytic degradation performance of mixed contaminants in complex practical wastewaters.** Electrocatalytic degradation performance of the  $\text{TiO}_x\text{C}_y$  membrane with mixed contaminants (i.e.,  $7 \text{ mg L}^{-1}$  each of sulfamethoxazole (SMX), propranolol (PRO), and ranitidine (RTD)) in complex solutions: (a) ultrapure water, (b) practical reverse osmosis (RO) concentrate, and (c) practical secondary effluent. All the tests were conducted at the continuous flow mode with a flux of  $849 \text{ L m}^{-2} \text{ h}^{-1}$  under 14 kPa at 3V. The removal ratio dropped when treating the mixed micropollutants in the practical water, especially in the RO concentrate and secondary effluent. The real water also contains a lot of other organic pollutants that can consume part of the oxidative active sites or ROS. These consumptions resulted in a decrease in PRO or RTD removal, but did not necessarily represent a decrease in overall pollutant removal performance. Future research is needed to fully analyze the changes of water matrix before and after treatment as well as to further optimize the conditions for the practical water treatment.

**Table S1. EXAFS fitting parameters at the Ti K-edge for various samples ( $S_0^2=0.7$  from Ti-foil)**

	Shell	CN <sup>a</sup>	R <sup>b</sup> (Å)	$\sigma^{2c}$ (Å <sup>2</sup> )	$\Delta E_0^d$ (eV)	R factor
Ti-foil	Ti-Ti	12	2.92±0.01	0.089	5.1±0.6	0.0079
Ti-TiO <sub>x</sub> C <sub>y</sub>	Ti-O/C/N	3.5±0.3	1.93±0.02	0.0035	-5.2±2.1	0.0165
	Ti-Ti	2.0±0.3	2.98±0.02	0.0041		

<sup>a</sup>CN: coordinatin numbers; <sup>b</sup>R: bond distance; <sup>c</sup> $\sigma^2$ : Debye-Waller factors; <sup>d</sup>  $\Delta E_0$ : the inner potential correction. R factor: goodness of fit. Error bounds that characterize the structural parameters obtained by EXAFS spectroscopy were estimated as CN±20%; R ± 1%;  $\sigma^2 \pm 20\%$ .

**Table S2. The referenced studies in the comparison of ECSA and cost.**

	ECSA cm <sup>2</sup> cm <sup>-2</sup>	Cost USD kg <sup>-1</sup>	Reference
This study	1840	1.63	This study
S1	107	6.90	(32)
S2	296.3	18.87	(80)
S3	7.5	6.58	(81)
S4	185	6.90	(15)
S5	90	6.90	(19)
S6	3.18	6.83	(17)
S7	63.5	3.95	(82)
S8	0.52	556.01	(33)
S9	54.5	35.13	(83)
S10	96.75	3.72	(84)
S11	430.5	10.66	(85)
S12	83.3	45.15	(86)
S13	221	4.78	(87)
S14	75	7.33	(88)
S15	2.2	2803.86	(13)
S16	1033.3	14.19	(22)

**Table S3. The referenced studies in the comparison of electrocatalysis efficiency.**

	Fabrication strategy	Membrane materials	Target pollutant	Initial target concentration, mg L <sup>-1</sup>	Removal amount, g m <sup>-2</sup> h <sup>-1</sup>	<i>k</i> , min <sup>-1</sup>	1/EEO, m <sup>3</sup> order kWh <sup>-1</sup>	1/SEC, g-pollutant kWh <sup>-1</sup>	Water flux, L m <sup>-2</sup> h <sup>-1</sup>	Mechanism	Reference
†	Bioinspired	TiO <sub>x</sub> C <sub>y</sub> membrane	Propranolol	0.5	0.41	166.6	35.83	11.52	849	The Bioinspired topological framework actuates an expeditious “transfer–reaction” mechanism via direct hole oxidation and indirect reactive oxygen species (ROS) oxidation.	This study
†	Bioinspired	TiO <sub>x</sub> C <sub>y</sub> membrane	Propranolol	2	1.69	238.2	44.50	41.01	849		This study
	Bioinspired	TiO <sub>x</sub> C <sub>y</sub> membrane	Propranolol	20	16.46	168.2	40.22	512.84	849		This study
†	Bioinspired	TiO <sub>x</sub> C <sub>y</sub> membrane	Sulfamethoxazole	2	1.68	219.9	35.01	34.65	849		This study
†	Bioinspired	TiO <sub>x</sub> C <sub>y</sub> membrane	Cimetidine	2	1.67	203.9	43.74	46.68	849		This study
†	Bioinspired	TiO <sub>x</sub> C <sub>y</sub> membrane	Ciprofloxacin	2	1.69	255.3	74.68	64.35	849		This study
†	Bioinspired	TiO <sub>x</sub> C <sub>y</sub> membrane	Ranitidine	2	1.69	253.9	66.00	57.21	849		This study
S1	(ii)	Nb/BDD	Propranolol	10	3.80	0.0101	0.024	0.413	843.5	Indirect oxidation by active chlorine	(89)
S2	(ii)	Ti/Pt	Propranolol	1.3	0.0637	0.0326	0.227	0.170	50	Direct oxidation (peroxydisulfate oxidation alone and electrolysis) and nonradical oxidation	(90)
S3	(ii)	Mixed-metal oxide anodes	Propranolol	0.26	0.0135	0.0217	0.208	0.024	53.03	Surface-bound reactive chlorine species (i.e., •Cl) oxidation	(91)
S4	(iii)	BDD/ADE–Pt/CF	Propranolol	135	7.3125	0.0029	0.005	2.825	83.33	n.r.	(92)
S5	(ii)	TiO <sub>2</sub> @SnO <sub>2</sub> –Sb	p-chloroaniline	1.276	0.0231	0.0019	0.805	1.581	31.25	•OH oxidation	(93)
S6	(ii)	Blue-colored TiO <sub>2</sub> nanotube arrays	Carbamazepine	10	9.36	0.403	11.63	101.69	954.65	•OH oxidation	(94)
S7*	(ii)	Ti/TiO <sub>2</sub> -NTs/PbO <sub>2</sub>	Reverse osmosis concentrate COD	310	12.74	0.009	0.006	2.439	55.56	•OH oxidation	(95)

S8	(ii)	TiO <sub>2</sub> nanotubes arrays electrode	Lipopolysaccharide	20	0.2844	0.0253	0.122	2.703	18	Direct electron transfer and •OH oxidation	(96)
S9	(ii)	Sb-doped SnO <sub>2</sub> with TiO <sub>2</sub> nanotube clusters on Ti mesh	Phenol	100	3.54	0.0676	0.312	8.852	35.42	•OH oxidation	(97)
S10*	(ii)	TiO <sub>2</sub> -NTA/SnO <sub>2</sub> -Sb anodes with/without PbO <sub>2</sub> layer	Reverse osmosis concentrates COD	169	14.90	0.0237	0.070	11.288	100	Reactive chlorine species and •OH oxidation	(98)
S11	(ii)	Macroporous-Ti-enhanced TiO <sub>2</sub> nanotube array/SnO <sub>2</sub> -Sb <sub>2</sub> O <sub>3</sub>	2-Methyl-4-isothiazolin-3-one	50	15.31	0.124	1.724	36	382.65	Nonradical and radical oxidation	(99)
S12	(ii)	Blue TiO <sub>2</sub> nanotubes covered with SnO <sub>2</sub> -Sb <sub>2</sub> O <sub>3</sub>	Benzoic acid	24.4	7.32	0.0076	0.121	2.610	500	n.r.	(100)
S13	(ii)	Blue-TiO <sub>2</sub> nanotubes	Phenol	100	6.47	0.0071	1.587	101.01	66.67	•OH and SO <sub>4</sub> <sup>•-</sup> oxidation	(101)
S14*	(ii)	Cobalt-doped Black-TiO <sub>2</sub> nanotube array	Latrine wastewater	500	2.34	0.0048	0.011	5.095	5.21	n.r.	(102)
S15*	(ii)	Blue-Black TiO <sub>2</sub> nanotube arrays	Human wastewater	330	1.44	0.0023	0.062	16.129	10.42	•OH oxidation	(103)
S16	(ii)	Ti/Ru <sub>0.3</sub> Ti <sub>0.7</sub> O	Formaldehyde	400	9.70	0.0161	0.016	2.939	24.44	n.r.	(104)
S17	(iii)	Ti <sub>4</sub> O <sub>7</sub>	Sulfamethoxazole	25.4	7.29	20.977	3.074	88.885	300	n.r.	(105)

S18	(ii)	Carbon nanotube electrochemical filter	Tetracycline	88.89	11.11	98.9	6.933	414.52	127.48	n.r.	(106)
S19	(ii)	Multi-walled carbon nanotube	Ciprofloxacin	5	0.48	1.38	0.310	1.900	127.48		(107)
S20	(ii)	Multi-walled carbon nanotube	Amoxicillin	5	0.62	3.66	0.849	2.450	127.48	Direct electron transfer and radical oxidation (e.g., •OH, Cl•)	(107)
S21	(ii)	Multi-walled carbon nanotube	Sulfamethoxazole	5	0.57	2.1	0.500	2.250	127.48		(107)
S22	(ii)	BDD	Ciprofloxacin	100	5.26	0.0715	1.429	35.71	52.62	n.r.	(108)
S23	(ii)	BDD	Norfloxacin	100	8.95	0.0158	0.040	4.167	105.25	•OH oxidation	(109)
S24	(i)	PANI/PI	Congo red	20	4.4	0.0707	0.307	5.867	250	•OH and OCl <sup>-</sup> oxidation	(110)
S25	(iii)	Bi-doped SnO <sub>2</sub> -Ti <sub>n</sub> O <sub>2n-1</sub>	Atrazine	2.157	0.65	115.1	2.381	1.712	300		(111)
S26	(iii)	Bi-doped SnO <sub>2</sub> -Ti <sub>n</sub> O <sub>2n-1</sub>	Clothianidin	2.497	0.74	67.9	1.205	1.701	300	Direct electron transfer and •OH oxidation	(111)
S27	(ii)	Ti/SnO <sub>2</sub> -Sb/Ce-PbO <sub>2</sub>	Naproxen	0.05	0.02	0.649	1.344	0.024	4	•OH oxidation	(112)
S28	(ii)	Ti/SnO <sub>2</sub> -Sb	Stavudine	0.02	0.01	0.24	0.690	0.007	8	•OH oxidation	(113)
S29	(i)	G/SnO <sub>2</sub> /CFs	Sulfamethoxazole	10	0.076	0.238	0.024	0.240	8.84	n.r.	(114)
S30	(iii)	SnO <sub>2</sub> -Sb reactive anodic filter	Ciprofloxacin	3.31	0.145	1.486	3.030	8.410	54	Direct electron transfer and •OH, SO <sub>4</sub> • <sup>-</sup> oxidation	(115)
S31	(i)	electrodeposited polytetrafluoroethylene (PTFE)-doped β-PbO <sub>2</sub>	Norfloxacin	100	8.418	0.0154	0.0202	1	85.03	n.r.	(116)

S32‡	(i)	CNT	Microcystin-LR	0.5	n.r.	0.3838	n.r.	n.r.	n.r.	n.r.	(117)
S33‡	(i)	CNT	Phenol	10	n.r.	0.0164	n.r.	n.r.	n.r.	n.r.	(118)
S34‡	(i)	GO@Polypyrrole	Ofloxacin	n.r.	n.r.	0.026	n.r.	n.r.	n.r.	H <sub>2</sub> O <sub>2</sub> and •OH oxidation	(119)
S35‡	(i)	MnO <sub>2</sub> @stainless steel	Phenol	500	n.r.	1.519	n.r.	n.r.	13.5	•OH oxidation	(120)
S36‡	(i)	Conductive poly(aminoanthraquinone)/reduced graphene oxide nanohybrid blended PVDF	Bovine serum albumin	500	n.r.	Antifouling	n.r.	n.r.	n.r.	Electrostatic repulsion force and electro-generated H <sub>2</sub> O <sub>2</sub>	(121)
S37‡	(i)	Carbon nanotube–polyvinyl alcohol composite	Alginic acid	3000-5000	n.r.	Antifouling	n.r.	n.r.	n.r.	Electrostatic forces	(122)
S38‡	(i)	MWCNT/graphene/PES nanocomposite	Bovine serum albumin	200	n.r.	Anti-fouling	n.r.	n.r.	n.r.	Electrostatic repulsion and generated gas bubbles	(123)

Note: (i) mixed matrix strategy; (ii) catalyst coating strategy; (iii) inorganic membrane strategy.

n.r. = not reported.

\*These data were based on treatments with mixed contaminants in complex solutions, thus potentially lower than those based on treatments with single contaminants in purer solutions.

†These data were not plotted in **Fig. 2c** to avoid overlap-induced ambiguity, since they are not fundamentally different from each other.

‡These studies were not included in **Fig. 2c** either because some data were not reported or they aimed at antifouling rather than degradation.

The references are classified and sorted according to the following basis: studies on the PRO degradation, studies using TiO<sub>2</sub>-based materials, studies using carbon-based materials, studies using SnO<sub>2</sub>-based materials, studies using PbO<sub>2</sub>-based materials, studies with some data not reported, studies aimed at antifouling based on the (i) mixed matrix strategy.

## REFERENCE AND NOTES

1. R. Zeng, Y. Yang, X. Feng, H. Li, L. M. Gibbs, F. J. DiSalvo, H. D. Abruña, Nonprecious transition metal nitrides as efficient oxygen reduction electrocatalysts for alkaline fuel cells. *Sci. Adv.* **8**, eabj1584 (2022).
2. A. Abdelhafiz, A. N. M. Tanvir, M. Zeng, B. Wang, Z. Ren, A. R. Harutyunyan, Y. Zhang, J. Li, Pulsed light synthesis of high entropy nanocatalysts with enhanced catalytic activity and prolonged stability for oxygen evolution reaction. *Adv. Sci.* **10**, 2300426 (2023).
3. Z. Liang, L. Song, M. Sun, B. Huang, Y. Du, Tunable CO/H<sub>2</sub> ratios of electrochemical reduction of CO<sub>2</sub> through the Zn-Ln dual atomic catalysts. *Sci. Adv.* **7**, eabl4915 (2021).
4. Y. Gao, S. Liang, B. Liu, C. Jiang, C. Xu, X. Zhang, P. Liang, M. Elimelech, X. Huang, Subtle tuning of nanodefects actuates highly efficient electrocatalytic oxidation. *Nat. Commun.* **14**, 2059 (2023).
5. L. Chen, A. N. Alshwabkeh, S. Hojabri, M. Sun, G. Xu, J. Li, A robust flow-through platform for organic contaminant removal. *Cell Rep. Phys. Sci.* **2**, 100296 (2021).
6. L. Liu, H. Lan, Y. Cui, Q. Tang, J. Bai, X. An, M. Sun, H. Liu, J. Qu, A Janus membrane with electro-induced multi-affinity interfaces for high-efficiency water purification. *Sci. Adv.* **10**, eadn8696 (2024).
7. L. Ren, J. Ma, M. Chen, Y. Qiao, R. Dai, X. Li, Z. Wang, Recent advances in electrocatalytic membrane for the removal of micropollutants from water and wastewater. *iScience* **25**, 104342 (2022).
8. W. Bian, W. Wu, B. Wang, W. Tang, M. Zhou, C. Jin, H. Ding, W. Fan, Y. Dong, J. Li, D. Ding, Revitalizing interface in protonic ceramic cells by acid etch. *Nature* **604**, 479–485 (2022).
9. S. Li, Q. Li, R. W. Carpick, P. Gumbsch, X. Z. Liu, X. Ding, J. Sun, J. Li, The evolving quality of frictional contact with graphene. *Nature* **539**, 541–545 (2016).

10. L. Jin, X. Duan, M. Sun, C. D. Vecitis, H. Yu, Y. Liu, A General strategy to synthesize fluidic single atom electrodes for selective reactive oxygen species production. *ACS Nano* **17**, 12875–12883 (2023).
11. Y. Yao, L. Zhao, J. Dai, J. Wang, C. Fang, G. Zhan, Q. Zheng, W. Hou, L. Zhang, Single atom Ru monolithic electrode for efficient chlorine evolution and nitrate reduction. *Angew. Chem. Int. Ed. Engl.* **61**, e202208215 (2022).
12. J. Ding, J. Huang, Q. Zhang, Z. Wei, Q. He, Z. Chen, Y. Liu, X. Su, Y. Zhai, A hierarchical monolithic cobalt-single-atom electrode for efficient hydrogen peroxide production in acid. *Cat. Sci. Technol.* **12**, 2416–2419 (2022).
13. E. Plaza-Mayoral, I. J. Pereira, K. Nicole Dalby, K. D. Jensen, I. Chorkendorff, H. Falsig, P. Sebastián-Pascual, M. Escudero-Escribano, Pd–Au nanostructured electrocatalysts with tunable compositions for formic acid oxidation. *ACS Appl. Energy Mater.* **5**, 10632–10644 (2022).
14. H. Xie, H. Zhang, X. Wang, G. Wei, S. Chen, X. Quan, Conductive and stable polyphenylene/CNT composite membrane for electrically enhanced membrane fouling mitigation. *Front. Environ. Sci. Eng.* **18**, 3 (2023).
15. C. C. Raj, R. Sundheep, R. Prasanth, Enhancement of electrochemical capacitance by tailoring the geometry of TiO<sub>2</sub> nanotube electrodes. *Electrochim. Acta* **176**, 1214–1220 (2015).
16. H. L. Hellstern, M. Bremholm, A. Mamakhel, J. Becker, B. B. Iversen, Hydrothermal synthesis of TiO<sub>2</sub>@SnO<sub>2</sub> hybrid nanoparticles in a continuous-flow dual-stage reactor. *ChemSusChem* **9**, 532–539 (2016).
17. Y. Lu, H. Cao, S. Xu, C. Jia, G. Zheng, A comparative study of the effects of different TiO<sub>2</sub> supports toward CO<sub>2</sub> electrochemical reduction on CuO/TiO<sub>2</sub> electrode. *RSC Adv.* **11**, 21805–21812 (2021).

18. P. Li, X. Qi, L. Zhao, J. Wang, M. Wang, M. Shao, J. S. Chen, R. Wu, Z. Wei, Hierarchical 3D porous carbon with facily accessible Fe–N<sub>4</sub> single-atom sites for Zn–air batteries. *J. Mater. Chem. A* **10**, 5925–5929 (2022).
19. M. Wang, B.-j. Kim, D. Suk Han, H. Park, Electrocatalytic activity of nanoparticulate TiO<sub>2</sub> coated onto Ta-doped IrO<sub>2</sub>/Ti substrates: Effects of the TiO<sub>2</sub> overlayer thickness. *Chem. Eng. J.* **425**, 131435 (2021).
20. W. Fan, B. Wang, R. Gao, G. Dimitrakopoulos, J. Wang, X. Xiao, L. Ma, K. Wu, B. Yildiz, J. Li, Anodic shock-triggered exsolution of metal nanoparticles from perovskite oxide. *J. Am. Chem. Soc.* **144**, 7657–7666 (2022).
21. J. Li, M. Li, N. An, S. Zhang, Q. Song, Y. Yang, J. Li, X. Liu, Boosted ammonium production by single cobalt atom catalysts with high Faradic efficiencies. *Proc. Natl. Acad. Sci. U.S.A.* **119**, e2123450119 (2022).
22. Y.-C. Zhang, C. Han, J. Gao, J. Wu, X.-D. Zhu, J.-J. Zou, Co<sub>3-x</sub>O<sub>4</sub>/NiO with abundant Ni<sup>3+</sup> active sites for boosting oxygen evolution reaction. *Chem. Eng. J.* **446**, 137036 (2022).
23. N. Shakibi Nia, C. Griesser, T. Mairegger, E.-M. Wernig, J. Bernardi, E. Portenkirchner, S. Penner, J. Kunze-Liebhäuser, Titanium oxycarbide as platinum-free electrocatalyst for ethanol oxidation. *ACS Catal.* **14**, 324–329 (2024).
24. Y. Gao, N. Yan, C. Jiang, C. Xu, S. Yu, P. Liang, X. Zhang, S. Liang, X. Huang, Filtration-enhanced highly efficient photocatalytic degradation with a novel electrospun rGO@TiO<sub>2</sub> nanofibrous membrane: Implication for improving photocatalytic efficiency. *Appl Catal B* **268**, 118737 (2020).
25. X. Li, W. Chen, Q. Qian, H. Huang, Y. Chen, Z. Wang, Q. Chen, J. Yang, J. Li, Y.-W. Mai, Electrospinning-based strategies for battery materials. *Adv. Energy Mater.* **11**, 2000845 (2021).
26. J. Wen, G. L. Wilkes, Organic/inorganic hybrid network materials by the Sol–Gel approach. *Chem. Mater.* **8**, 1667–1681 (1996).

27. J. Cheng, H. Ma, Y. Shi, L. Liu, W. Shang, W. Liu, S. Li, W. Li, Y. Wang, Y. Shi, Single-atom Ti decorated carbon black and carbon nanotubes: Modular dual-carbon electrode for optimizing the charge transport kinetics of perovskite solar cells. *Adv. Funct. Mater.* **34**, 2409533 (2024).
28. L. Kuai, Z. Chen, S. Liu, E. Kan, N. Yu, Y. Ren, C. Fang, X. Li, Y. Li, B. Geng, Titania supported synergistic palladium single atoms and nanoparticles for room temperature ketone and aldehydes hydrogenation. *Nat. Commun.* **11**, 48 (2020).
29. D. N. Miller, A. K. Azad, H. Delpouve, L. Quazuguel, J. Zhou, A. Sinha, P. Wormald, J. T. S. Irvine, Studies on the crystal structure, magnetic and conductivity properties of titanium oxycarbide solid solution ( $\text{TiO}_{1-x}\text{Cx}$ ). *J. Mater. Chem. A* **4**, 5730–5736 (2016).
30. R. Tröger, H. Ren, D. Yin, C. Postigo, P. D. Nguyen, C. Baduel, O. Golovko, F. Been, H. Joerss, M. R. Boleda, S. Polesello, M. Roncoroni, S. Taniyasu, F. Menger, L. Ahrens, F. Yin Lai, K. Wiberg, What's in the water?—Target and suspect screening of contaminants of emerging concern in raw water and drinking water from Europe and Asia. *Water Res.* **198**, 117099 (2021).
31. S. S. Jeon, P. W. Kang, M. Klingenhof, H. Lee, F. Dionigi, P. Strasser, Active surface area and intrinsic catalytic oxygen evolution reactivity of NiFe LDH at reactive electrode potentials using capacitances. *ACS Catal.* **13**, 1186–1196 (2023).
32. S. Franz, H. Arab, G. L. Chiarello, M. Bestetti, E. Selli, Single-step preparation of large area  $\text{TiO}_2$  photoelectrodes for water splitting. *Adv. Energy Mater.* **10**, 2000652 (2020).
33. K. Shi, Z. S. Parsons, X. Feng, Sensitivity of gas-evolving electrocatalysis to the catalyst microenvironment. *ACS Energy Lett.* **8**, 2919–2926 (2023).
34. J. Shen, G. Liu, Y. Han, W. Jin, Artificial channels for confined mass transport at the sub-nanometre scale. *Nat. Rev. Mater.* **6**, 294–312 (2021).
35. C. Liu, A.-Y. Zhang, Y. Si, D.-N. Pei, H.-Q. Yu, Photochemical protection of reactive sites on defective  $\text{TiO}_{2-x}$  surface for electrochemical water treatment. *Environ. Sci. Technol.* **53**, 7641–7652 (2019).

36. A.-Y. Zhang, T. Lin, Y.-Y. He, Y.-X. Mou, Heterogeneous activation of H<sub>2</sub>O<sub>2</sub> by defect-engineered TiO<sub>2-x</sub> single crystals for refractory pollutants degradation: A Fenton-like mechanism. *J. Hazard. Mater.* **311**, 81–90 (2016).
37. M. Bai, B. Hong, K. Zhang, K. Yuan, K. Xie, W. Wei, Y. Lai, Defect-rich carbon nitride as electrolyte additive for in-situ electrode interface modification in lithium metal battery. *Chem. Eng. J.* **407**, 127123 (2021).
38. J. P. Flach, P. H. Figueiredo de Lima, J. C. Sparks, M. Islam, R. Martinez-Duarte, Synthesis of titanium oxycarbide through carbothermal reduction of titanium dioxide nanoparticles and renewable biopolymers. *ECS Trans.* **72**, 17–23 (2016).
39. Ministry of Ecology and Environment of the People's Republic of China. *Discharge standard of pollutants for urban wastewater treatment plant* (Ministry of Ecology and Environment of the People's Republic of China, 2022).
40. U. S. E. P. Agency, in *National Primary Drinking Water Regulations* (2024).
41. G. Chen, Z. Ma, K. Xiao, X. Wang, S. Liang, X. Huang, Hierarchically textured superhydrophilic polyvinylidene fluoride membrane via nanocasting and post-fabrication grafting of surface-tailored silica nanoparticles. *Environ. Sci. Nano* **6**, 3579–3589 (2019).
42. H. Shi, Y. Wang, C. Li, R. Pierce, S. Gao, Q. Huang, Degradation of perfluorooctanesulfonate by reactive electrochemical membrane composed of magnéli phase titanium suboxide. *Environ. Sci. Technol.* **53**, 14528–14537 (2019).
43. M. Li, K. Zuo, S. Liang, K. Xiao, P. Liang, X. Wang, X. Huang, Electrically tuning ultrafiltration behavior for efficient water purification. *Environ. Sci. Technol.* **54**, 11536–11545 (2020).
44. Y. Wang, X. Liu, X. Han, R. Godin, J. Chen, W. Zhou, C. Jiang, J. F. Thompson, K. B. Mustafa, S. A. Shevlin, J. R. Durrant, Z. Guo, J. Tang, Unique hole-accepting carbon-dots promoting selective carbon dioxide reduction nearly 100% to methanol by pure water. *Nat. Commun.* **11**, 2531 (2020).

45. C. Liu, Y. Min, A.-Y. Zhang, Y. Si, J.-J. Chen, H.-Q. Yu, Electrochemical treatment of phenol-containing wastewater by facet-tailored TiO<sub>2</sub>: Efficiency, characteristics and mechanisms. *Water Res.* **165**, 114980 (2019).
46. X. Wang, D. Guo, J. Zhang, Y. Yao, Y. Liu, Insights into the electron transfer mechanisms of permanganate activation by carbon nanotube membrane for enhanced micropollutants degradation. *Front. Environ. Sci. Eng.* **17**, 106 (2023).
47. Z. Pan, C. Song, L. Li, H. Wang, Y. Pan, C. Wang, J. Li, T. Wang, X. Feng, Membrane technology coupled with electrochemical advanced oxidation processes for organic wastewater treatment: Recent advances and future prospects. *Chem. Eng. J.* **376**, 120909 (2019).
48. S. Lan, J. Feng, Y. Xiong, S. Tian, S. Liu, L. Kong, Performance and mechanism of piezo-catalytic degradation of 4-chlorophenol: Finding of effective piezo-dechlorination. *Environ. Sci. Technol.* **51**, 6560–6569 (2017).
49. L. Peng, H. Liu, W.-L. Wang, Z.-B. Xu, X.-Y. Ni, Y.-H. Wu, Q.-Y. Wu, H.-Y. Hu, Degradation of methylisothiazolinone biocide using a carbon fiber felt-based flow-through electrode system (FES) via anodic oxidation. *Chem. Eng. J.* **384**, 123239 (2020).
50. Y. Zhao, M. Sun, X. Wang, C. Wang, D. Lu, W. Ma, S. A. Kube, J. Ma, M. Elimelech, Janus electrocatalytic flow-through membrane enables highly selective singlet oxygen production. *Nat. Commun.* **11**, 6228 (2020).
51. J. Wandt, P. Jakes, J. Granwehr, H. A. Gasteiger, R.-A. Eichel, Singlet oxygen formation during the charging process of an aprotic lithium–oxygen battery. *Angew. Chem. Int. Ed. Engl.* **55**, 6892–6895 (2016).
52. W. Huang, X. Wang, W. Zhang, S. Zhang, Y. Tian, Z. Chen, W. Fang, J. Ma, Intraligand charge transfer boosts visible-light-driven generation of singlet oxygen by metal-organic frameworks. *Appl Catal B* **273**, 119087 (2020).
53. Y. Qian, D. Li, Y. Han, H.-L. Jiang, Photocatalytic molecular oxygen activation by regulating excitonic effects in covalent organic frameworks. *J. Am. Chem. Soc.* **142**, 20763–20771 (2020).

54. C. Dong, Y. Bao, T. Sheng, Q. Yi, Q. Zhu, B. Shen, M. Xing, I. M. C. Lo, J. Zhang, Singlet oxygen triggered by robust bimetallic MoFe/TiO<sub>2</sub> nanospheres of highly efficacy in solar-light-driven peroxymonosulfate activation for organic pollutants removal. *Appl Catal B* **286**, 119930 (2021).
55. C. Trelu, M. Rivallin, S. Cerneaux, C. Coetsier, C. Causserand, M. A. Oturan, M. Cretin, Integration of sub-stoichiometric titanium oxide reactive electrochemical membrane as anode in the electro-Fenton process. *Chem. Eng. J.* **400**, 125936 (2020).
56. H. Tu, M. Huang, Y. Yi, Z. Li, Y. Zhan, J. Chen, Y. Wu, X. Shi, H. Deng, Y. Du, Chitosan-rectorite nanospheres immobilized on polystyrene fibrous mats via alternate electrospinning/electrospraying techniques for copper ions adsorption. *Appl. Surf. Sci.* **426**, 545–553 (2017).
57. A. Abdelhafiz, B. Wang, A. R. Harutyunyan, J. Li, Carbothermal shock synthesis of high entropy oxide catalysts: Dynamic structural and chemical reconstruction boosting the catalytic activity and stability toward oxygen evolution reaction. *Adv. Energy Mater.* **12**, 2200742 (2022).
58. X. Li, S. Shao, Y. Yang, Y. Mei, W. Qing, H. Guo, L. E. Peng, P. Wang, C. Y. Tang, Engineering interface with a one-dimensional RuO<sub>2</sub>/TiO<sub>2</sub> heteronanostructure in an electrocatalytic membrane electrode: Toward highly efficient micropollutant decomposition. *ACS Appl. Mater. Interfaces* **12**, 21596–21604 (2020).
59. S. Liang, W. Zheng, L. Zhu, W. Duan, C. Wei, C. Feng, One-step treatment of phosphite-laden wastewater: A single electrochemical reactor integrating superoxide radical-induced oxidation and electrocoagulation. *Environ. Sci. Technol.* **53**, 5328–5336 (2019).
60. B. Ravel, M. Newville, ATHENA, ARTEMIS, HEPHAESTUS: Data analysis for x-ray absorption spectroscopy using IFEFFIT. *J. Synchrotron Radiat.* **12**, 537–541 (2005).
61. C. Trelu, C. Coetsier, J.-C. Rouch, R. Esmilaire, M. Rivallin, M. Cretin, C. Causserand, Mineralization of organic pollutants by anodic oxidation using reactive electrochemical membrane synthesized from carbothermal reduction of TiO<sub>2</sub>. *Water Res.* **131**, 310–319 (2018).

62. V. Maneeratana, D. Portehault, J. Chaste, D. Mailly, M. Antonietti, C. Sanchez, Original electrospun core-shell nanostructured magnéli titanium oxide fibers and their electrical properties. *Adv. Mater.* **26**, 2654–2658 (2014).
63. A. Wang, X. Liu, Y. Wen, Y. Qiu, S. Lv, M. Xu, C. Meng, K. Wang, F. Lin, S. Xie, Q. Zhuo, Single-atom Zr embedded  $\text{Ti}_4\text{O}_7$  anode coupling with hierarchical  $\text{CuFe}_2\text{O}_4$  particle electrodes toward efficient electrooxidation of actual pharmaceutical wastewater. *Water Res.* **245**, 120596 (2023).
64. D. Huang, D. J. Kim, K. Rigby, X. Zhou, X. Wu, A. Meese, J. Niu, E. Stavitski, J.-H. Kim, Elucidating the Role of single-atom Pd for electrocatalytic hydrodechlorination. *Environ. Sci. Technol.* **55**, 13306–13316 (2021).
65. T. Li, S. Ren, C. Zhang, L. Qiao, J. Wu, P. He, J. Lin, Y. Liu, Z. Fu, Q. Zhu, W. Pan, B. Wang, Z. Chen, Cobalt single atom anchored on N-doped carbon nanoboxes as typical single-atom catalysts (SACs) for boosting the overall water splitting. *Chem. Eng. J.* **458**, 141435 (2023).
66. Y. Liao, C.-H. Loh, M. Tian, R. Wang, A. G. Fane, Progress in electrospun polymeric nanofibrous membranes for water treatment: Fabrication, modification and applications. *Prog. Polym. Sci.* **77**, 69–94 (2018).
67. C. J. Luo, S. D. Stoyanov, E. Stride, E. Pelan, M. Edirisinghe, Electrospinning versus fibre production methods: From specifics to technological convergence. *Chem. Soc. Rev.* **41**, 4708–4735 (2012).
68. L. Persano, A. Camposeo, C. Tekmen, D. Pisignano, Industrial upscaling of electrospinning and applications of polymer nanofibers: A review. *Macromol. Mater. Eng.* **298**, 504–520 (2013).
69. M. Yu, R.-H. Dong, X. Yan, G.-F. Yu, M.-H. You, X. Ning, Y.-Z. Long, Recent advances in needleless electrospinning of ultrathin fibers: From academia to industrial production. *Macromol. Mater. Eng.* **302**, 1700002 (2017).

70. H. B. Madalosso, R. Machado, D. Hotza, C. Marangoni, Membrane surface modification by electrospinning, coating, and plasma for membrane distillation applications: A state-of-the-art review. *Adv. Eng. Mater.* **23**, 2001456 (2021).
71. J. Xue, T. Wu, Y. Dai, Y. Xia, Electrospinning and electrospun nanofibers: Methods, materials, and applications. *Chem. Rev.* **119**, 5298–5415 (2019).
72. H. Lin, H. Peng, X. Feng, X. Li, J. Zhao, K. Yang, J. Liao, D. Cheng, X. Liu, S. Lv, J. Xu, Q. Huang, Energy-efficient for advanced oxidation of bio-treated landfill leachate effluent by reactive electrochemical membranes (REMs): Laboratory and pilot scale studies. *Water Res.* **190**, 116790 (2021).
73. T. X. Huong Le, L. F. Dumée, S. Lacour, M. Rivallin, Z. Yi, L. Kong, M. Bechelany, M. Cretin, Hybrid graphene-decorated metal hollow fibre membrane reactors for efficient electro-Fenton - Filtration co-processes. *J. Membr. Sci.* **587**, 117182 (2019).
74. N. Mameda, H. J. Park, K. H. Choo, Membrane electro-oxidizer: A new hybrid membrane system with electrochemical oxidation for enhanced organics and fouling control. *Water Res.* **126**, 40–49 (2017).
75. H. Hui, H. Wang, Y. Mo, Z. Yin, J. Li, Optimal design and evaluation of electrocatalytic reactors with nano-MnOx/Ti membrane electrode for wastewater treatment. *Chem. Eng. J.* **376**, 120190 (2019).
76. K. V. Plakas, S. D. Sklari, D. A. Yiankakis, G. T. Sideropoulos, V. T. Zaspalis, A. J. Karabelas, Removal of organic micropollutants from drinking water by a novel electro-Fenton filter: Pilot-scale studies. *Water Res.* **91**, 183–194 (2016).
77. D. Yu, M. Wu, Q. Hu, L. Wang, C. Lv, L. Zhang, Iron-based metal-organic frameworks as novel platforms for catalytic ozonation of organic pollutant: Efficiency and mechanism. *J. Hazard. Mater.* **367**, 456–464 (2019).

78. J. Lim, Y. Yang, M. R. Hoffmann, Activation of peroxymonosulfate by oxygen vacancies-enriched cobalt-doped black TiO<sub>2</sub> nanotubes for the removal of organic pollutants. *Environ. Sci. Technol.* **53**, 6972–6980 (2019).
79. C. C. L. McCrory, S. Jung, I. M. Ferrer, S. M. Chatman, J. C. Peters, T. F. Jaramillo, Benchmarking hydrogen evolving reaction and oxygen evolving reaction electrocatalysts for solar water splitting devices. *J. Am. Chem. Soc.* **137**, 4347–4357 (2015).
80. M. Szkoda, A. Ilnicka, M. Skorupska, M. Wysokowski, J. P. Lukaszewicz, Modification of TiO<sub>2</sub> nanotubes by graphene–strontium and cobalt molybdate perovskite for efficient hydrogen evolution reaction in acidic medium. *Sci. Rep.* **12**, 22577 (2022).
81. A. M. Díez, I. Núñez, M. Pazos, M. Á. Sanromán, Y. V. Kolen'ko, Fluoride-doped TiO<sub>2</sub> photocatalyst with enhanced activity for stable pollutant degradation. *Catalysts* **12**, 1190 (2022).
82. J. Li, Y. Kuang, X. Zhang, W.-H. Hung, C.-Y. Chiang, G. Zhu, G. Chen, F. Wang, P. Liang, H. Dai, Electrochemical acetate production from high-pressure gaseous and liquid CO<sub>2</sub>. *Nat. Catal.* **6**, 1151–1163 (2023).
83. Y. Zhao, Y. Wang, Y. Dong, C. Carlos, J. Li, Z. Zhang, T. Li, Y. Shao, S. Yan, L. Gu, J. Wang, X. Wang, Quasi-two-dimensional earth-abundant bimetallic electrocatalysts for oxygen evolution reactions. *ACS Energy Lett.* **6**, 3367–3375 (2021).
84. Y. Yan, J. Lin, K. Huang, X. Zheng, L. Qiao, S. Liu, J. Cao, S. C. Jun, Y. Yamauchi, J. Qi, Tensile strain-mediated spinel ferrites enable superior oxygen evolution activity. *J. Am. Chem. Soc.* **145**, 24218–24229 (2023).
85. Y. Wei, Y. Hu, P. Da, Z. Weng, P. Xi, C.-H. Yan, Triggered lattice-oxygen oxidation with active-site generation and self-termination of surface reconstruction during water oxidation. *Proc. Natl. Acad. Sci. U.S.A.* **120**, e2312224120 (2023).
86. F. Ye, S. Zhang, Q. Cheng, Y. Long, D. Liu, R. Paul, Y. Fang, Y. Su, L. Qu, L. Dai, C. Hu, The role of oxygen-vacancy in bifunctional indium oxyhydroxide catalysts for

- electrochemical coupling of biomass valorization with CO<sub>2</sub> conversion. *Nat. Commun.* **14**, 2040 (2023).
87. F. Yao, M. Jia, Q. Yang, F. Chen, Y. Zhong, S. Chen, L. He, Z. Pi, K. Hou, D. Wang, X. Li, Highly selective electrochemical nitrate reduction using copper phosphide self-supported copper foam electrode: Performance, mechanism, and application. *Water Res.* **193**, 116881 (2021).
88. S. I. Perez Bakovic, P. Acharya, M. Watkins, H. Thornton, S. Hou, L. F. Greenlee, Electrochemically active surface area controls HER activity for Fe<sub>x</sub>Ni<sub>100-x</sub> films in alkaline electrolyte. *J. Catal.* **394**, 104–112 (2021).
89. J. D. García-Espinoza, M. Zolfaghari, P. Mijaylova Nacheva, Synergistic effect between ultraviolet irradiation and electrochemical oxidation for removal of humic acids and pharmaceuticals. *Water Environ. J.* **34**, 232–246 (2020).
90. H. Song, L. Yan, J. Ma, J. Jiang, G. Cai, W. Zhang, Z. Zhang, J. Zhang, T. Yang, Nonradical oxidation from electrochemical activation of peroxydisulfate at Ti/Pt anode: Efficiency, mechanism and influencing factors. *Water Res.* **116**, 182–193 (2017).
91. J. T. Jasper, O. S. Shafaat, M. R. Hoffmann, Electrochemical transformation of trace organic contaminants in latrine wastewater. *Environ. Sci. Technol.* **50**, 10198–10208 (2016).
92. E. Isarain-Chávez, R. M. Rodríguez, P. L. Cabot, F. Centellas, C. Arias, J. A. Garrido, E. Brillas, Degradation of pharmaceutical beta-blockers by electrochemical advanced oxidation processes using a flow plant with a solar compound parabolic collector. *Water Res.* **45**, 4119–4130 (2011).
93. J. Zheng, Z. Wang, J. Ma, S. Xu, Z. Wu, Development of an electrochemical ceramic membrane filtration system for efficient contaminant removal from waters. *Environ. Sci. Technol.* **52**, 4117–4126 (2018).

94. L. Xu, J. Niu, H. Xie, X. Ma, Y. Zhu, J. Crittenden, Effective degradation of aqueous carbamazepine on a novel blue-colored TiO<sub>2</sub> nanotube arrays membrane filter anode. *J. Hazard. Mater.* **402**, 123530 (2021).
95. F. Wei, D. Liao, Y. Lin, C. Hu, J. Ju, Y. Chen, D. Feng, Electrochemical degradation of reverse osmosis concentrate (ROC) using the electrodeposited Ti/TiO<sub>2</sub>-NTs/PbO<sub>2</sub> electrode. *Sep. Purif. Technol.* **258**, 118056 (2021).
96. K. Wang, Y. Li, J. Huang, L. Xu, L. Yin, Y. Ji, C. Wang, Z. Xu, J. Niu, Insights into electrochemical decomposition mechanism of lipopolysaccharide using TiO<sub>2</sub> nanotubes arrays electrode. *J. Hazard. Mater.* **391**, 122259 (2020).
97. L. Huang, D. Li, J. Liu, L. Yang, C. Dai, N. Ren, Y. Feng, Construction of TiO<sub>2</sub> nanotube clusters on Ti mesh for immobilizing Sb-SnO<sub>2</sub> to boost electrocatalytic phenol degradation. *J. Hazard. Mater.* **393**, 122329 (2020).
98. M. Chen, S. Pan, C. Zhang, C. Wang, W. Zhang, Z. Chen, X. Zhao, Y. Zhao, Electrochemical oxidation of reverse osmosis concentrates using enhanced TiO<sub>2</sub>-NTA/SnO<sub>2</sub>-Sb anodes with/without PbO<sub>2</sub> layer. *Chem. Eng. J.* **399**, 125756 (2020).
99. M. Chen, C. Wang, X. Zhao, Y. Wang, W. Zhang, Z. Chen, X. Meng, J. Luo, J. Crittenden, Development of a highly efficient electrochemical flow-through anode based on inner in-site enhanced TiO<sub>2</sub>-nanotubes array. *Environ. Int.* **140**, 105813 (2020).
100. X. Meng, Z. Chen, C. Wang, W. Zhang, K. Zhang, S. Zhou, J. Luo, N. Liu, D. Zhou, D. Li, J. Crittenden, Development of a three-dimensional electrochemical system using a blue TiO<sub>2</sub>/SnO<sub>2</sub>-Sb<sub>2</sub>O<sub>3</sub> anode for treating low-ionic-strength wastewater. *Environ. Sci. Technol.* **53**, 13784–13793 (2019).
101. J. Cai, M. Zhou, Y. Pan, X. Du, X. Lu, Extremely efficient electrochemical degradation of organic pollutants with co-generation of hydroxyl and sulfate radicals on Blue-TiO<sub>2</sub> nanotubes anode. *Appl Catal B* **257**, 117902 (2019).

102. Y. Yang, L. C. Kao, Y. Liu, K. Sun, H. Yu, J. Guo, S. Y. H. Liou, M. R. Hoffmann, Cobalt-doped black TiO<sub>2</sub> nanotube array as a stable anode for oxygen evolution and electrochemical wastewater treatment. *ACS Catal.* **8**, 4278–4287 (2018).
103. Y. Yang, M. R. Hoffmann, Synthesis and stabilization of blue-black TiO<sub>2</sub> nanotube arrays for electrochemical oxidant generation and wastewater treatment. *Environ. Sci. Technol.* **50**, 11888–11894 (2016).
104. M. T. Fukunaga, J. R. Guimarães, R. Bertazzoli, Kinetics of the oxidation of formaldehyde in a flow electrochemical reactor with TiO<sub>2</sub>/RuO<sub>2</sub> anode. *Chem. Eng. J.* **136**, 236–241 (2008).
105. S. N. Misal, M.-H. Lin, S. Mehraeen, B. P. Chaplin, Modeling electrochemical oxidation and reduction of sulfamethoxazole using electrocatalytic reactive electrochemical membranes. *J. Hazard. Mater.* **384**, 121420 (2020).
106. Y. Liu, H. Liu, Z. Zhou, T. Wang, C. N. Ong, C. D. Vecitis, Degradation of the common aqueous antibiotic tetracycline using a carbon nanotube electrochemical filter. *Environ. Sci. Technol.* **49**, 7974–7980 (2015).
107. T.-Y. Tan, Z.-T. Zeng, G.-M. Zeng, J.-L. Gong, R. Xiao, P. Zhang, B. Song, W.-W. Tang, X.-Y. Ren, Electrochemically enhanced simultaneous degradation of sulfamethoxazole, ciprofloxacin and amoxicillin from aqueous solution by multi-walled carbon nanotube filter. *Sep. Purif. Technol.* **235**, 116167 (2020).
108. J. F. Carneiro, J. M. Aquino, B. F. Silva, A. J. Silva, R. C. Rocha-Filho, Comparing the electrochemical degradation of the fluoroquinolone antibiotics norfloxacin and ciprofloxacin using distinct electrolytes and a BDD anode: Evolution of main oxidation byproducts and toxicity. *J. Environ. Chem. Eng.* **8**, 104433 (2020).
109. D. A. C. Coledam, J. M. Aquino, B. F. Silva, A. J. Silva, R. C. Rocha-Filho, Electrochemical mineralization of norfloxacin using distinct boron-doped diamond anodes in a filter-press reactor, with investigations of toxicity and oxidation by-products. *Electrochim. Acta* **213**, 856–864 (2016).

110. M.-L. Liu, L. Li, Y.-X. Sun, Z.-J. Fu, X.-L. Cao, S.-P. Sun, Scalable conductive polymer membranes for ultrafast organic pollutants removal. *J. Membr. Sci.* **617**, 118644 (2021).
111. P. Gayen, C. Chen, J. T. Abiade, B. P. Chaplin, Electrochemical oxidation of atrazine and clothianidin on Bi-doped  $\text{SnO}_2$ - $\text{TiO}_{2n-1}$  electrocatalytic reactive electrochemical membranes. *Environ. Sci. Technol.* **52**, 12675–12684 (2018).
112. L. Xu, X. Ma, J. Niu, J. Chen, C. Zhou, Removal of trace naproxen from aqueous solution using a laboratory-scale reactive flow-through membrane electrode. *J. Hazard. Mater.* **379**, 120692 (2019).
113. C. Zhou, Y. Wang, J. Chen, J. Niu, Porous  $\text{Ti/SnO}_2$ -Sb anode as reactive electrochemical membrane for removing trace antiretroviral drug stavudine from wastewater. *Environ. Int.* **133**, 105157 (2019).
114. S. Yu, Y. Gao, R. Khan, P. Liang, X. Zhang, X. Huang, Electrospun PAN-based graphene/ $\text{SnO}_2$  carbon nanofibers as anodic electrocatalysis microfiltration membrane for sulfamethoxazole degradation. *J. Membr. Sci.* **614**, 118368 (2020).
115. C. Yang, Y. Fan, S. Shang, P. Li, X. Y. Li, Fabrication of a permeable  $\text{SnO}_2$ -Sb reactive anodic filter for high-efficiency electrochemical oxidation of antibiotics in wastewater. *Environ. Int.* **157**, 106827 (2021).
116. I. Sánchez-Montes, J. R. Fuzer Neto, B. F. Silva, A. J. Silva, J. M. Aquino, R. C. Rocha-Filho, Evolution of the antibacterial activity and oxidation intermediates during the electrochemical degradation of norfloxacin in a flow cell with a PTFE-doped  $\beta$ - $\text{PbO}_2$  anode: Critical comparison to a BDD anode. *Electrochim. Acta* **284**, 260–270 (2018).
117. G. Wei, X. Quan, X. Fan, S. Chen, Y. Zhang, Carbon-nanotube-based sandwich-like hollow fiber membranes for expanded microcystin-LR removal applications. *Chem. Eng. J.* **319**, 212–218 (2017).

118. Y. Yang, S. Qiao, M. Zheng, J. Zhou, X. Quan, Enhanced permeability, contaminants removal and antifouling ability of CNTs-based hollow fiber membranes under electrochemical assistance. *J. Membr. Sci.* **582**, 335–341 (2019).
119. D. Huang, G. Wang, X. Zhao, W. Pang, M. Wang, D. Wang, Electrogeneration of hydrogen peroxide in neutral medium using PVDF-based air cathode for removing ofloxacin in wastewater. *J. Solid State Electrochem.* **23**, 1455–1462 (2019).
120. J. Chen, S. Fan, Y. Chen, Y. Wang, K. Bai, Z. Mai, Z. Xiao, Electrocatalytic composite membrane with deep-permeation nano structure fabricated by flowing synthesis for enhanced catalysis. *J. Membr. Sci.* **636**, 119616 (2021).
121. H. Liu, G. Zhang, C. Zhao, J. Liu, F. Yang, Hydraulic power and electric field combined antifouling effect of a novel conductive poly(aminoanthraquinone)/reduced graphene oxide nanohybrid blended PVDF ultrafiltration membrane. *J. Mater. Chem. A* **3**, 20277–20287 (2015).
122. A. V. Dudchenko, J. Rolf, K. Russell, W. Duan, D. Jassby, Organic fouling inhibition on electrically conducting carbon nanotube–polyvinyl alcohol composite ultrafiltration membranes. *J. Membr. Sci.* **468**, 1–10 (2014).
123. F. Sun, J. Yang, Q. Shen, M. Li, H. Du, D. Y. Xing, Conductive polyethersulfone membrane facilely prepared by simultaneous phase inversion method for enhanced anti-fouling and separation under low driven-pressure. *J. Environ. Manage.* **297**, 113363 (2021).